Simulation of a Cavity-Type Receiver for Concentrated Solar Power Towers

by

Ivan James Fuller

A thesis in partial fulfillment of

the requirements for the degree of

Master of Science

(Mechanical Engineering)

At the

UNIVERSITY OF WISCONSIN – MADISON

2020

Approved by

_____

Professor Gregory F. Nellis

_____

Professor Douglas T. Reindl

_____

Date

ABSTRACT

The object of this research was to develop a thermal model for a cavity-type receiver that could be integrated into the National Renewable Energy Laboratory's Solar Advisor Model (SAM) software. External receivers are currently the most common type of receivers currently being used for concentrated solar power towers. The receiver is constructed by a set of panels, comprised of a network of tightly bundled tubing, assembled in an approximate cylindrical shape with a heat transfer fluid being routed through the tubing. This allows for a 360° heliostat field surrounding the tower as well as a large active surface area which is directly irritated by the heliostat field. Since the external receiver is directly exposed to the ambient environment, it will be subjected to convective and radiative losses. The convection losses occur because of buoyancy induced flow from the large temperature gradient between the panels and the ambient air as well as from force convection caused by wind. The radiation losses of the system occur to the environment by reflected short wavelength radiation and emitted long wavelength radiation.

To mitigate a portion of the radiative and convective losses of the external receiver, cavity receivers were proposed. By enclosing the surface area that is directly irradiated from the heliostat field, it is hypothesized that this will prevent a percentage of the thermal losses due to convection and radiation which will lead to a higher efficiency of the power tower system. However, current modeling software such as SolarPILOT and SAM, which are developed by the Nation Renewable Energy Laboratory (NREL), are not capable of simulating these types of receivers.

New code has been developed for the integration with SolarPILOT and SAM to allow for the heat transfer modeling of a half-octagonal cavity type receiver. The incident solar flux on the cavity receiver is determined by NREL's SolTrace software. SolTrace uses a Monte Carlo ray tracing method to determine the incident solar flux on the cavity surfaces. The radiation heat transfer is determined using view factors calculated by numerical and Monte Carlo methods. The view factors are modified to incorporate indirect radiation transfer by the F-hat method for both a short-wavelength and long-wavelength radiation band. The convective heat transfer is determined using correlations from literature for cavity type receivers.

The code developed offers another avenue for parametric studies and comparison between the two types of receivers without the use of CFD software. It was shown that the cavity receiver has a better overall thermal performance compared to an external cylindrical receiver system with the same active area and incident power. The receiver surface coating was shown to play a major role on each system's efficiencies. The selective coatings such as the Ti-Si multi-layer material developed by Sandia results in smaller differences in efficiency between the two designs, however the cavity was still maintained a higher efficiency.

Table of Contents

List of Figures

Nomenclature

A	m^2	Surface area
β	$\frac{1}{K}$	Expansion Factor
c	$\frac{J}{kg-K}$	Specific Heat
D	m	Diameter
E_b	$\frac{W}{m^2}$	Blackbody emissive power
F	-	View Factor
$\hat{F}$	-	F-hat parameter
Flux	$\frac{W}{m^2}$	Solar Flux
G	$\frac{W}{m^2}$	Irradiation
Gr	-	Grashof number
H	m	Height
h	$\frac{W}{m^2K}$	Heat transfer coefficient
J	$\frac{W}{m^2}$	Radiosity
k	$\frac{W}{m-K}$	Thermal conductivity
L	m	Length
$\dot{m}$	$\frac{kg}{s}$	Mass flowrate
N	-	Number of surfaces; Number of nodes
Nu	-	Nusselt number
Pr	-	Prantl number
$\dot{Q}$	W	Heat transfer rate
R	$\frac{W}{K}$	Heat transfer resistance
Ra	-	Rayleigh number
Re	-	Reynolds number
T	K	Temperature

UA	$\frac{W}{K}$	Conductance

Greek Letters

α	-	Absorptivity
β	$\frac{1}{K}$	Expansion Factor
ε	-	Emissivity
η	-	Efficiency
θ	-	Angle; Cavity tilt angle
μ	$\frac{kg}{m-s}$	Dynamic Viscosity
ν	$\frac{m^2}{s}$	Kinematic Viscosity
ρ	-	Reflectivity

Subscripts

a	Aperature
b	Bulk
c	Characteristic
cz	Convective zone
i, j, k	Surfaces
n	Horizontal nodes
m	Vertical nodes
solar	Solar Radiation (Short-wave)
thermal	Thermal Radiation (Long-wave)
∞	Infinity; Ambient

Acronyms

CFD	Computational Fluid Dynamics
CSP	Concentrated Solar Power

DNI	Direct Normal Irradiance; Direct Normal Insolation
HTF	Heat Transfer Fluid
NREL	National Renewable Energy Laboratory
MATLAB	Matrix Laboratory
SAM	Solar Advisor Model
SP	SolarPILOT
ST	SolTrace

1. Introduction

With the increasing demand for renewable sources of energy in the United States, solar power has experienced a resurgence in research and technology development. Solar technology uses the abundant solar radiation that is incident on Earth as the source for electric energy production. Within the field of solar energy, Concentrated Solar Power (CSP) has become one of the leading methods of large-scale energy generation that is competing with fossil fuels and natural gas. As of 2018, the levelized cost of electricity for these systems has dropped to $0.185/kwh and is projected to be competitive with fossil fuel-based generation within the next decade (IRENA, 2019).

1.1 Concentrated Solar Power Tower

Concentrating solar power (CSP) systems utilize mirrors to focus incident solar beam radiation onto a target receiver. The thermal energy absorbed by the receiver is then used to heat a working fluid and produce electricity through a power cycle. Currently, there are four main types of CSP technologies: parabolic trough, Fresnel, power tower, and dish Stirling. Both parabolic trough and Fresnel systems reflect and focus incident beam solar radiation onto a linear receiver. Both power towers and dish Stirling systems utilize parabolic mirrors to reflect and focus beam solar radiation onto a single “point source” receiver.

The focus of the present research is on solar power towers, which use several thousand reflective mirrors, known as heliostats, to redirect incident solar radiation to a receiver at the top of a tower as seen in Figure 1.1. The main benefit of this type of CSP technology is the high power conversion efficiency that can be achieved due to higher operating temperatures from the large number of heliostats used. The two factors that limit solar towers are the materials of construction for the receiver surface and the thermal properties of the heat transfer fluid (HTF). Inherent in all CSP technologies is the need for high levels of beam solar radiation. Within the U.S., locations with the highest beam radiation are found in the deserts of the southwest as shown in Figure 1.2.

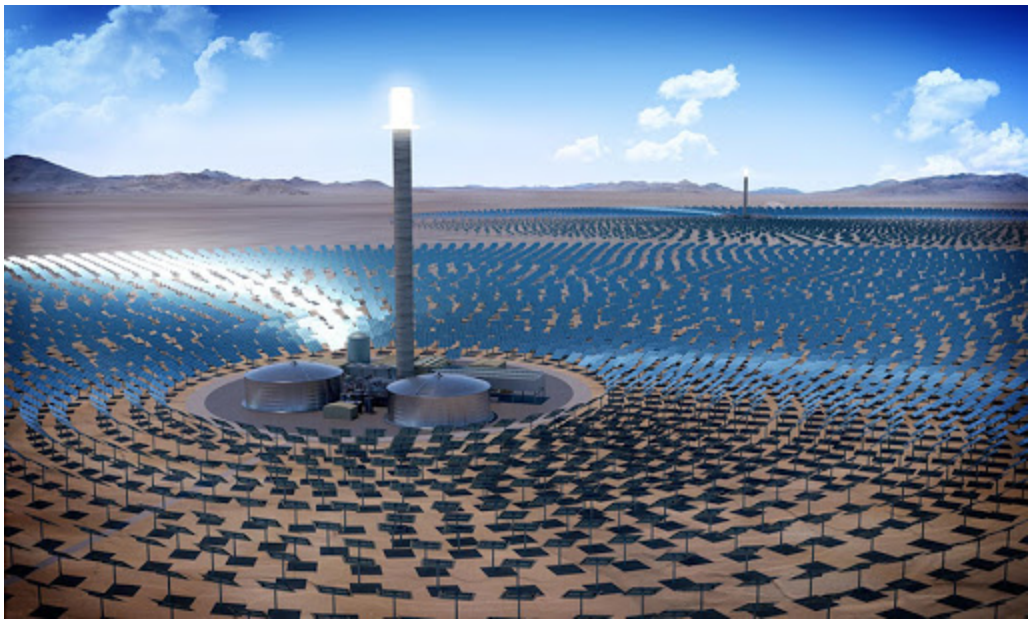

Figure 5.1 - Copiapó Solar Project Rendering. Reprinted from (Gallego, B., 2016).

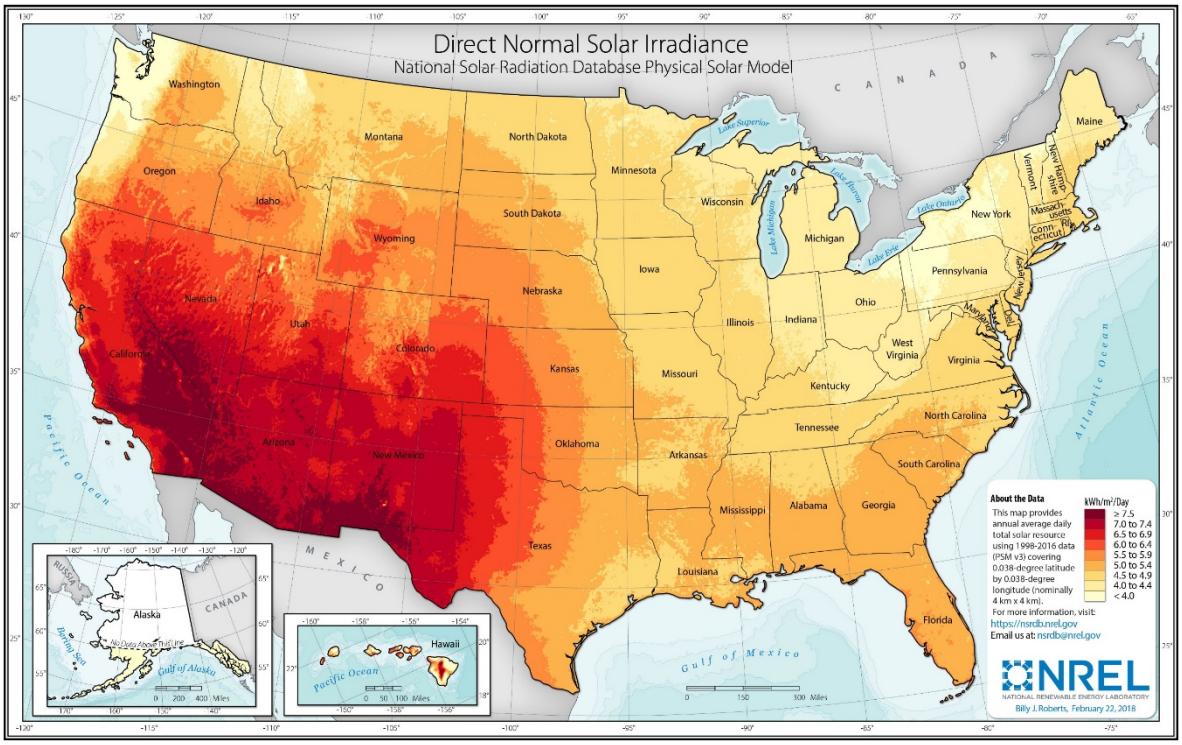

Figure 6.2 – U.S. Annual Solar DNI. Reprinted from (Sengupta et al., 2016).

1.1.1 Technology Overview

The main components of a Solar Tower are the heliostat field, the receiver, and the heat transfer fluid (HTF). The system is completed by incorporating a "power block" that converts the thermal energy to electrical power utilizing an appropriate cycle configuration such as a Rankine or closed Brayton cycle. The heliostat field is comprised of highly reflective surfaces (Figure 1.3) that move throughout the day to track the sun and concentrate the reflected solar radiation onto the tower's receiver. Due to the large number of heliostats, the aggregate of the reflected radiation from each heliostat within the field can produce a high density of solar flux onto the receiver's surface(s). The distribution of energy on the receiver generally depends on the quantity and type of heliostats, the direct normal irradiance (DNI) value, and the aiming strategy. DNI is a quantity that is dependent on the location of the plant and how much energy from the sun will directly be received on an area basis, which is dependent on weather and the location of the sun relative to the earth.

The "aiming strategies" determine where each heliostat in the field will be pointed to achieve a desired distribution of reflected radiation onto the receiver surface(s) commonly referred to as the "flux distribution." The flux distribution can be uniform which means the receiver receives the same amount of energy across its entire surface. The flux can also be localized on defined portions of the receiver to preheat a HTF or for various other reasons. The maximum flux value is limited by the receiver surface material, as temperatures exceeding the operating temperature limits of the receiver material can possibly damage or degrade the material or even cause fires if the mirrors are misaligned, as was the case of the Ivanpah plant in 2016 (Lillian, B. 2016).

Figure 1.3 - Front view of a Sanlúcar 120 heliostat. Reprinted from (Osuna et al., 2006).

The tower's receiver design and construction material is heavily influenced by the type of HTF that the tower will use to convert the incident solar radiation to usable thermal energy (Ho & Iverson, 2014). One common type of fluid used in solar power tower applications is $60NaNO_3$ $40KNO_3$. Nitrate salts have low melting point (~220°C), are stable up to 530-565°C, can be used as a media for thermal storage, and are cheaper than other molten salts (Ding et al, 2019). These properties make molten salts a suitable choice for current solar power towers. Research is currently being conducted to find a replacement salt mixture that can achieve higher operational temperatures, while still maintaining favorable properties such as a low melting point. Carbonate salts such as LiNaK have an operating range from approximately 390°C to over 650°C which would make them a good candidate. However, the use of lithium for batteries has driven the price of LiNaK up substantially. Currently the cost of LiNaK is $1.3-2.5 per kilogram, which is 2 to 3 times more expensive than nitrate salts. Another alternative is fluoride salts which are similar to carbonate salts but have a higher melting point and better thermal stability. Fluoride-based salts do have some drawbacks including being hazardous material and still relatively expensive. The Department of Energy is currently supporting the development of chloride salts which have a moderate melting point (400°C) while being stable at temperatures over 800°C, with prices of $0.35 to $1, depending on the purity. Chloride salts still have significant issues that need to be addressed. Low purity levels in these types of salts results in high corrosion rates to the receiver pipes and the high corrosion rates will lead to premature failures of the receiver's fluid piping.

External receivers are the most common type of receivers currently being used for solar power towers. The receiver panels are commonly constructed from a network of tightly bundled tubing (i.e. no separate surface) as seen in Figure 1.4, arranged in an approximate cylindrical shape (Figure 1.5a), with the HTF routed through a network of piping that is thermally coupled to the panel. This allows for a 360° heliostat field surrounding the tower as well as a large active surface area (i.e., the area transferring heat directly to HTF). Since the external receiver is exposed to the environment, it will be subjected to convective and radiative losses. The convection loss is caused by both buoyancy-induced flow from the large temperature gradient between the panels and the ambient air as well as from the ambient wind local to and flowing past the receiver surfaces. Radiation loss occur to the environment by a combination of reflected short-wavelength radiation and emitted long-wavelength radiation from the high surface temperature of the receiver to the lower temperature surroundings. These two loss mechanisms can account for large energy losses depending on the receiver design and plant location.

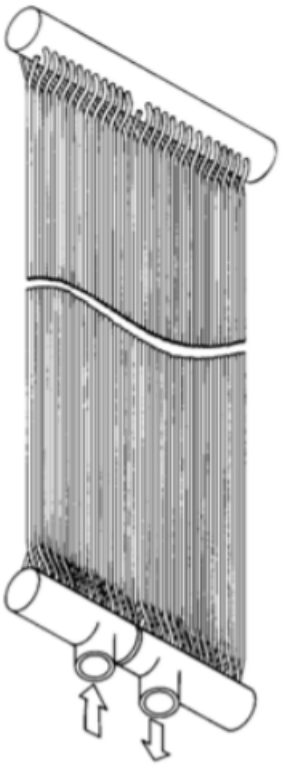

Figure 1.4 - Schematic of a tubular panel. Adapted from (Ho, C. K., & Iverson, B., 2012).

Cavity receivers were designed with the concept of limiting convective losses by having the active panels sheltered by passive surfaces (Figure 1.5b) which do not participate in the transfer of energy to the HTF. Enclosing the active panels is hypothesized to prevent a percentage of the thermal losses due to convection and long-wave thermal radiation as the active surfaces are not directly exposed to the environment. This is thought to improve the efficiency of the receiver system.

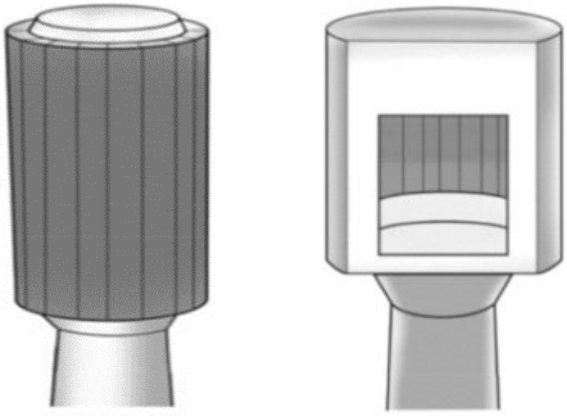

Figure 1.5 - a) Left: External receiver b.) Right: Cavity receiver. Reprinted from (Ho & Iverson, 2014).

1.2 Literature Review

A literature review was conducted to determine the current information and research regarding cavity-type receiver systems for solar power towers. The largest gap in information for receivers is that of the convective losses. This literature review will focus on the available material relating to this aspect. Research for convective losses can be separated into two categories: correlations and computational fluid dynamics (CFD) simulations. The initial part of the literature review will be dedicated to correlations and the remaining will be involving CFD. It should be noted that the majority of the CFD simulations are based on smaller cavity receivers for another type of CSP technology, dish-Stirling. However, the trends seen in the smaller scale cavity may be similar to those of solar tower cavities.

1.2.1 Samanes & Garcia-Barberena (2014)

(Samanes & Garcia-Barberena, 2014) conducted a comparison between five different natural convection correlations: (Clausing, 1983), (Leibfried & Ortjohann, 1995), (Clausing et al., 1987), (Siebers & Kraabel, 1984), and (Paitoonsurikan & Lovegrove, 2006). The five correlations are compared using Modelica to simulate a PS10 cavity-type receiver (Figure 1.6) with solar salt as the working fluid. The results show that the estimated convection losses with four of the correlations are in reasonable agreement while the Paitoonsurikan & Lovegrove model estimated about double the amount of energy loss as the others, as seen in Table 1. Clausing's 1983 model shows the lowest convection loss estimation at 27.39% of the total thermal losses while the average convection loss of the four (excluding Paitoonsurikan & Lovegrove) are 31.82%. It should be noted that out of the five correlations, only the correlations by Paitoonsurikan & Lovegrove and Leibfried & Ortjohan provide no validity range for their respective correlations.

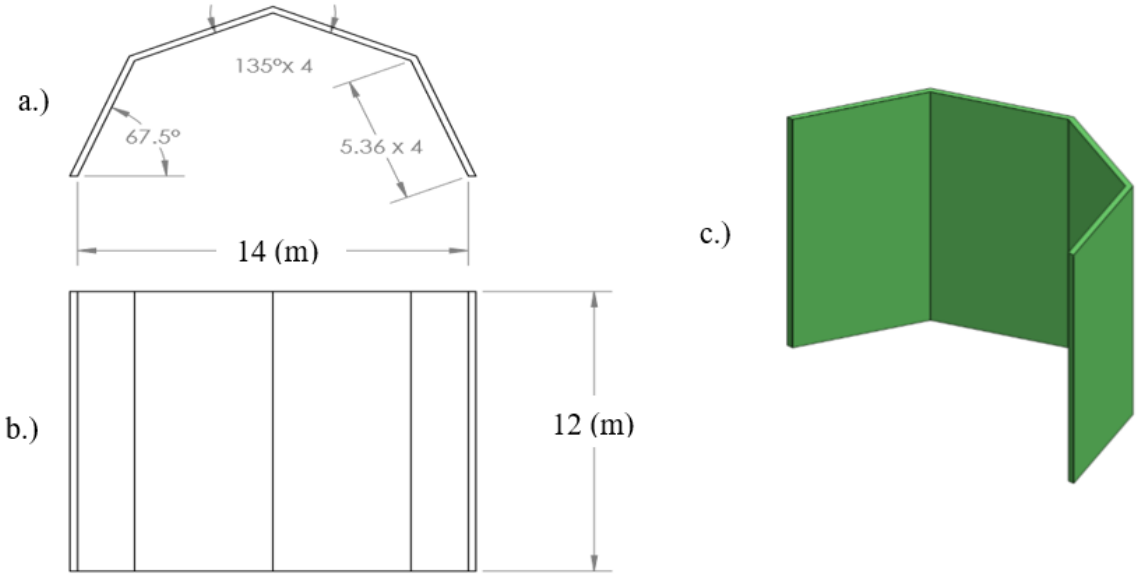

Figure 1.6 – Solidworks CAD model of approximation of PS10 panel geometry. a.) Top view. b.) Front view. c.) Isometric view.

MODEL	GENERAL PERFORMANCE			%Heat Loss
Clausing 1983	Power absorbed	5,177E+07		
	Efficiency	91,34%		
	Heat Losses	5,338E+06	Convection	27,39%
			Conduction	10,24%
			Radiation	62,37%
Clausing 1987	Power absorbed	5,118E+07		
	Efficiency	90,31%		
	Heat Losses	5,591E+06	Convection	35,57%
			Conduction	12,41%
			Radiation	52,02%
Siebers and Kraabel	Power absorbed	5,111E+07		
	Efficiency	90,17%		
	Heat Losses	5,705E+06	Convection	34,08%
			Conduction	12,62%
			Radiation	53,30%
Paitoonsurikarn and Lovegrove	Power absorbed	4,833E+07		
	Efficiency	85,28%		
	Heat Losses	7,848E+06	Convection	63,42%
			Conduction	3,50%
			Radiation	33,08%
Leibfried and Ortjohann	Power absorbed	5,140E+07		
	Efficiency	90,69%		
	Heat Losses	5,496E+06	Convection	30,23%
			Conduction	13,38%
			Radiation	56,40%

Table 1 - Comparison of convection correlations. Reprinted from (Samanes et al., 2014).

There are large uncertainties with each of these correlations. Clausing claims that the errors for the 1983 and 1987 are ±1% and ±20% respectively. Paitoonsurikan & Lovegrove state that 40% of the data have an error of ±20%, and 80% of the data with an error of ±50%

1.2.2 Clausing 1987

The convection correlations developed by (Clausing et al., 1987) are based on experimental data obtained from 0.4 meter side-facing isothermal cubical cavities with varying apertures. The data was collected from a cryogenic wind tunnel with air at a temperature ranging between 80K and 310K, so that large Rayleigh numbers and temperature ratios between the wall and ambient air could be achieved. The goal was to match the large Rayleigh numbers and temperature ratios that are characteristic of larger-scale solar receivers. The correlations developed relied on previous work from (Clausing, 1983) which is a resistance based analytical model with the introduction of assumed stagnant and convective zones within the cavity as illustrated in Figure 1.7. The stagnant zone within the cavity is created by an upper aperture “lip” and this zone is assumed to not result in any convective losses to the ambient environment.

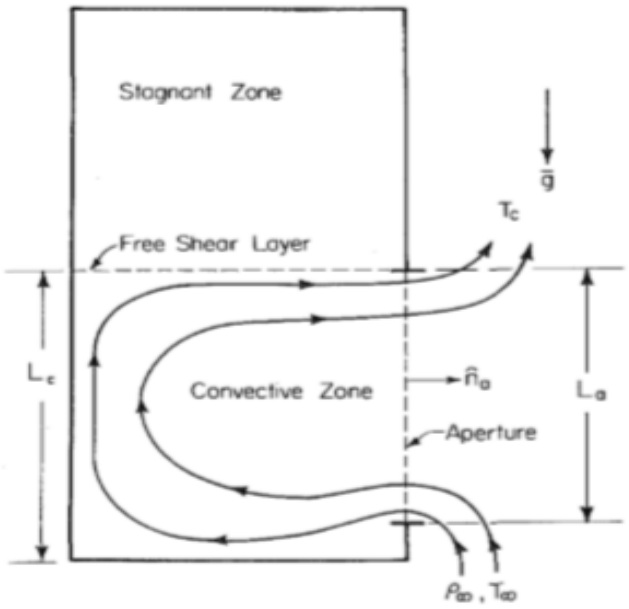

Figure 1.7 - Stagnant and Convective zone of cavity receiver (Clausing 1983).

The correlation developed allows for the Nusselt number to be calculated in accordance with Eq (1.1). The variable g is related to the Rayleigh number, f attempts to accounts for the variable properties of air between the wall and ambient temperature, and b accounts for the effect of the property variations that occur when the bulk air temperature (T_b) and the ambient temperature differ significantly.

$$Nu = \frac{hL_c}{k} = \frac{\dot{Q}L_c}{A_{cz}(T_w - T_\infty)k} = g \cdot f \cdot b \tag{1.1}$$

The b variable is found by the implicit function given in Eq (1.2). The formula requires fluid properties at both the ambient and film temperature, characteristic length (L_c), aperture height (L_a), aperture area (A_a), convective zone area (A_{cz}), as well as the g and f variables. The characteristic length is defined as the aperture height plus half the receiver height. The parameter A_{cz}, is the area that is below the stagnant zone, including all the sides and the aperture area. The g and f variables can be found using Eqs (1.3-1.5) depending on the flow regime.

$$b = 1 - 1.57\left[\frac{g \cdot f \cdot b\left(\frac{k_w}{k_\infty}\right)}{\left(Ra_\infty \cdot Pr_\infty \cdot \frac{L_a}{L_c}\right)^{\frac{1}{2}} \cdot \left(\frac{A_a}{A_{cz}}\right)}\right]^{\frac{2}{3}} \tag{1.2}$$

Laminar – regime I for:

$$Ra < 3.8 \times 10^8 \equiv Ra_{laminar}$$

$$g = 0.63Ra^{\frac{1}{4}} \tag{1.3}$$

$$f_{laminar} = 1$$

Transitional – regime II for:

$$Ra_{laminar} < Ra < 1.6 \times 10^9 \equiv Ra_{transition}$$

$$g = 0.63Ra^{\frac{1}{4}} \tag{1.4}$$

$$f_{transition} = (f_{turbulent} - 1) \cdot \left(\frac{Ra^{1/3} - Ra_{laminar}^{1/3}}{Ra_{turbulent}^{1/3} - Ra_{laminar}^{1/3}}\right) + 1$$

Turbulent – regime III for:

$$Ra > 1.6 \times 10^9 \equiv Ra_{turbulent}$$

$$g = 0.108Ra^{\frac{1}{3}} \tag{1.5}$$

$$f_{turbulent} = 0.2524 + 0.9163 \cdot \left(\frac{T_w}{T_\infty}\right) - 0.1663 \cdot \left(\frac{T_w}{T_\infty}\right)^2$$

The valid range for the correlation depends on the Rayleigh number, the wall and ambient temperature ratio, and the aperture area as given in Eqs (1.6-1.8).

$$3x10^7 < Ra < 3x10^{10} \tag{1.6}$$

$$1 < \frac{T_w}{T_\infty} < 3 \tag{1.7}$$

$$\frac{L^2}{18} \leq A_a \leq L^2 \tag{1.8}$$

1.2.3 Siebers and Kraabel (1984)

(Siebers & Kraabel, 1984) developed a correlation for both cylindrical and cavity type receivers through experimental data derived from scaled receivers. The cavities tested were a 2.2m high receiver and two cubical cavities of size 0.2m and 0.6m. With this correlation, the Nusselt number can be found with Eqs. (1.9) and (1.10), with the fluid properties being determined at ambient temperature. The correlation is valid in the range of $10^5 < Gr < 10^{12}$. The authors claim that the correlation is independent of length scale due to the 1/3 exponent in Eq (1.10).

$$Gr_l = \frac{g\beta(T_{wall} - T_\infty)L_c^3}{\upsilon^2} \tag{1.9}$$

$$Nu_l = 0.088 Gr_l^{\frac{1}{3}} \left(\frac{T_w}{T_\infty}\right)^{0.18} \tag{1.10}$$

The authors also provide a correction factor that can be used to find a modified heat transfer coefficient (1.11) for cavities with a tilt and/or added upper and bottom lips. This correction factor is based on ratios of areas, with A_1 being the entire area of the cavity, A_2 is the total cavity area minus the bottom lip, and A_3 is the area below a horizontal plane that intersects the lowest point of the top of the receiver as seen in Figure 1.8. The value of the exponent, *n*, is 0.63 for inclinations less than or equal to 30°, and 0.8 for angles greater than 30°.

$$h_{nc} = h_{nc,0} \cdot \left(\frac{A_1}{A_2}\right)\left(\frac{A_3}{A_1}\right)^n \tag{1.11}$$

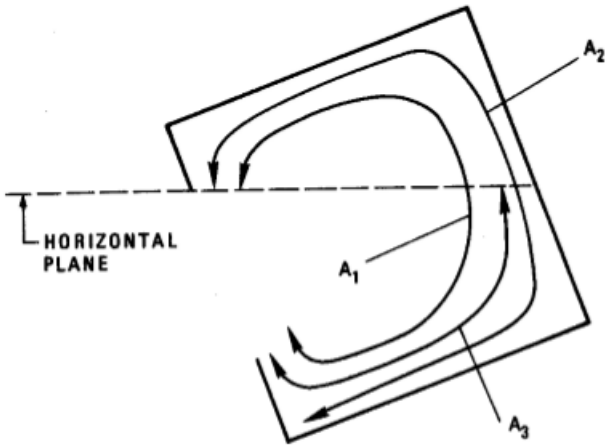

Figure 1.8 - Cavity areas for correction factor. Reprinted from (Siebers, D. and Kraabel J., 1984).

1.2.4 Jilte (2013)

This study by (Jilte et al., 2013) involves the comparison of various small-scale cavity receivers of different shapes for dish-Stirling systems. Fluent was used for the CFD modeling of seven different types of receivers as seen in Figure 1.9. For the study, the receivers have the same inner active heat transfer area as well as the same aperture area (0.5 m). The simulations were performed at isothermal wall temperature of 523-923K with increments of 100K as well as inclination angles from 0°- 90° in increments of 15°. The ambient temperature for each simulation was held constant at 300K.

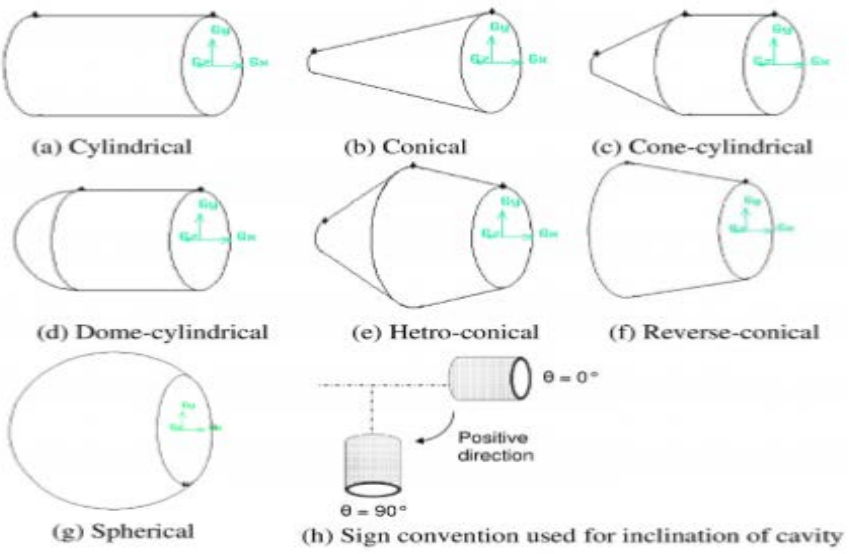

Figure 1.9 - Geometries for CFD study, reprinted from (Jilte et al., 2013).

The results from the simulations show that the conical cavity, (b), has the lowest convective losses, and the spherical cavity, (g), has the highest loss. Figure 1.10 shows the losses for each geometry at a wall temperature of 723 K. It can also be seen that the inclination angle can have a large impact on the convective loss with an angle of 45° reducing convective losses by a factor of approximately 2. Additionally, the data collected from the CFD simulations were compared against values obtained from using the Clausing (1987) correlation and showed good agreement.

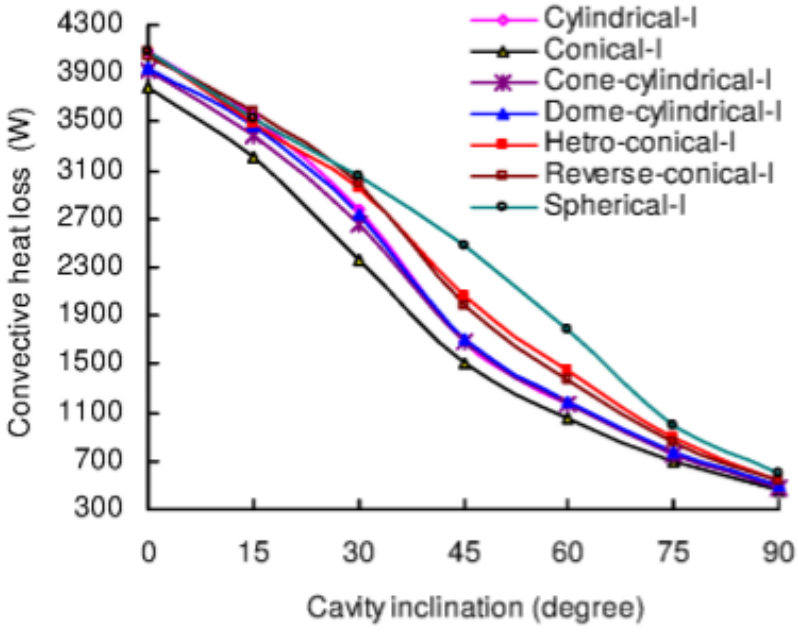

Figure 1.10 - Convective loss at T_{wall} = 723K. Adapted from (Jilte et al., 2013).

1.2.5 Ngo (2014)

This numerical study by (Ngo et al., 2014) investigates the effects of added fins to the interior lips of a cavity receiver and their effects on the heat loss due to convection for a spherical cavity for a dish-Stirling system. The study investigates the effects of the fins at three inclination angles, 0°, 30°, and 60°, with the "no-fin" case serving as the baseline for comparison. Figure 1.11 shows the baseline receiver as well as the added fins to the modified receiver.

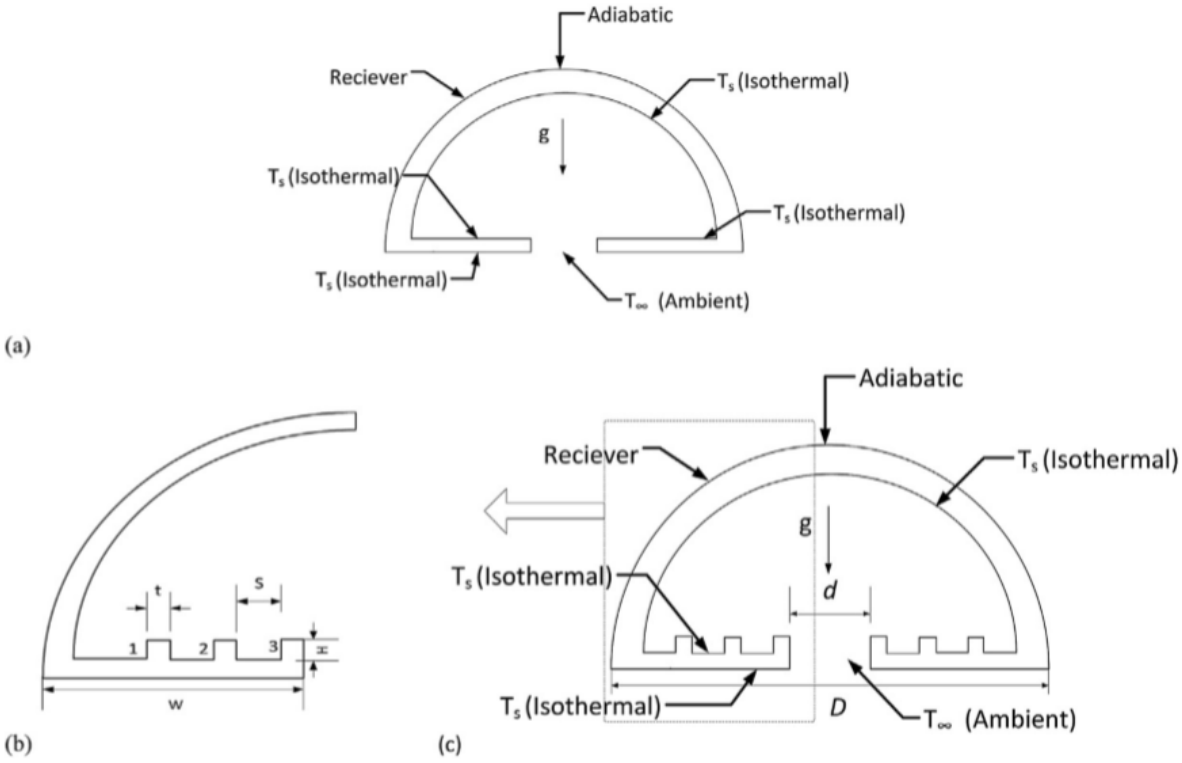

Figure 1.11 - Cavity receiver baseline, and modified receiver with fins. Reprinted from (Ngo et al., 2014).

The results from this study show that the fins are more effective at preventing energy loss from convection with an increasing Rayleigh number as seen in Figure 1.12. It is also apparent that inclination of the receiver has a greater effect on limiting convection losses by a significant margin when compared to the fins. The fins are generally more effective when the convection losses are larger and seem to approach the baseline receiver as the losses decrease.

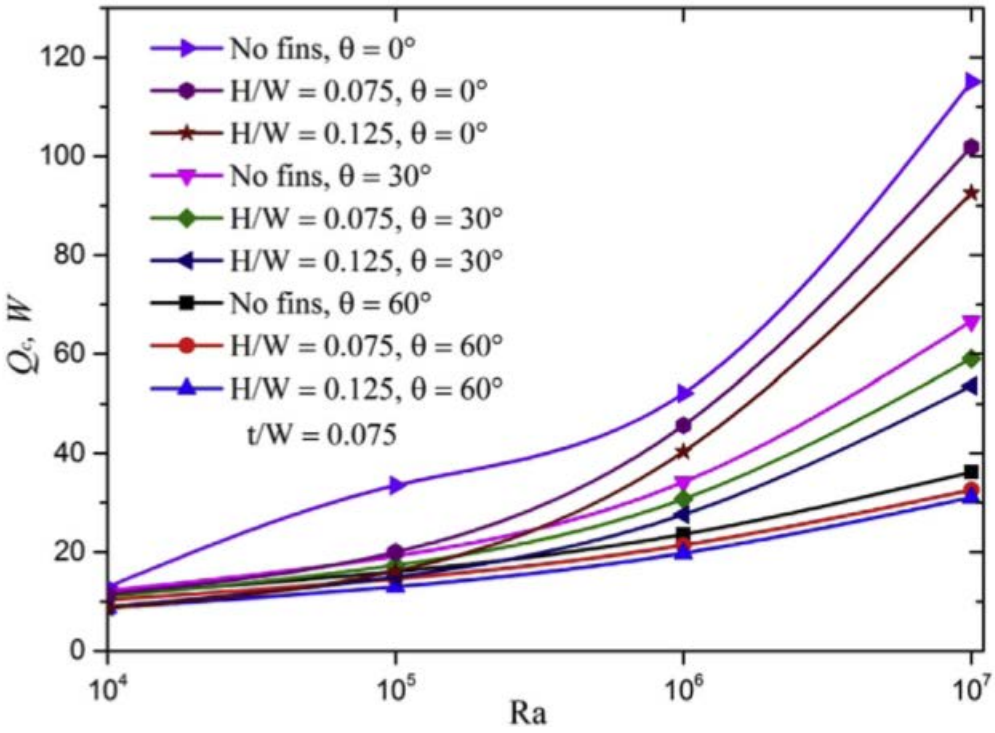

Figure 1.12. Rayleigh number vs convection loss. Reprinted from (Ngo et al., 2014).

1.3 Objective of this work

The main objective of this work is to (1) develop and integrate a heat transfer model that is capable of determining the incident solar flux from the heliostat field, (2) calculate the losses for radiation and convection, (3) calculate the energy gain to the HTF, and (4) incorporate the combined model into existing software from the National Renewable Energy Laboratory (NREL). The first software package to be used is *SolTrace*, which is a Monte Carlo ray tracing program used to simulate optical systems. This software will be used to create and model a heliostat field as well as the cavity receiver so the solar flux incident on the active surfaces of the receiver panels can be determined. The second program is SolarPILOT, which is a program developed to model and optimize external cylindrical receivers for power tower systems. The program will be modified to both accommodate a cavity receiver design and to run parametric models. The final program is the Solar Advisor Model (SAM) which is a thermal/financial model of the renewable energy systems, which will use the new thermal model to predict annual performance forecasts for future plants that use the cavity receiver design. The modifications to this program should have flexibility in the code to accommodate future modifications and allow for new features to be easily implemented.

2. Software for Simulating Heat Flux

Determining the distribution of reflected radiant or solar flux on the cavity receiver's panels is the first major step in modeling the cavity receiver system. To determine the solar flux distribution for a specified heliostat field and receiver, the software package *SolTrace* is used as it has the capability to simulate complex optical systems. Two other software codes, *DELSOL3* and

Tonatiuh were also investigated and compared to determine the accuracy and agreement with *SolTrace*.

2.1 SOLTRACE

SolTrace is a Monte-Carlo based ray-tracing software created by NREL to model complex optical systems for solar applications. The software requires three main data sets for the simulation: insolation data, definition of stages/geometric elements, and the optical properties of each element. The position of the sun is specified using either global coordinates or with a latitude, day, and hour. The sun's "disk shape" can be either set to a pillbox, Gaussian, or a user-defined distribution. A set of optical properties are then defined for all the elements that will be modeled as part of the system, these properties include the reflectivity, transmissivity, and optical errors that are associated with an element's surface. For example, optical properties for every heliostat can be defined once and named "Heliostat Optics". Later when creating each heliostat element, the optic type will be set to "Heliostat Optics". This is done so that optical properties of duplicate elements such as heliostats do not have to be repeatedly defined during element creation. Stages are set to define the progression of the optical analysis (Figure 2.1), i.e. for modeling a solar power tower, the heliostat field is set as stage 1 and the receiver is set as stage 2 as the sun's rays will be reflected off the heliostat field first and then intersect the receiver surface(s). Within a stage, elements need to be created for every geometric entity that will be involved in the optical model (heliostat, receiver, etc.). For each element, up to 29 values may need to be set, these values include the global coordinates of the element, its orientation in space, the geometric shape of the element, the surface of the geometric shape (flat, parabolic, etc.), the interaction that rays will have on the surface (reflection/refraction), and the set of optical properties of the element (these were the set of optical properties that were defined earlier). A user-specified number of ray interactions is set for the simulation, and the analysis is performed resulting in solar flux maps for each element. For a solar power tower, flux maps would be generated for the receiver elements.

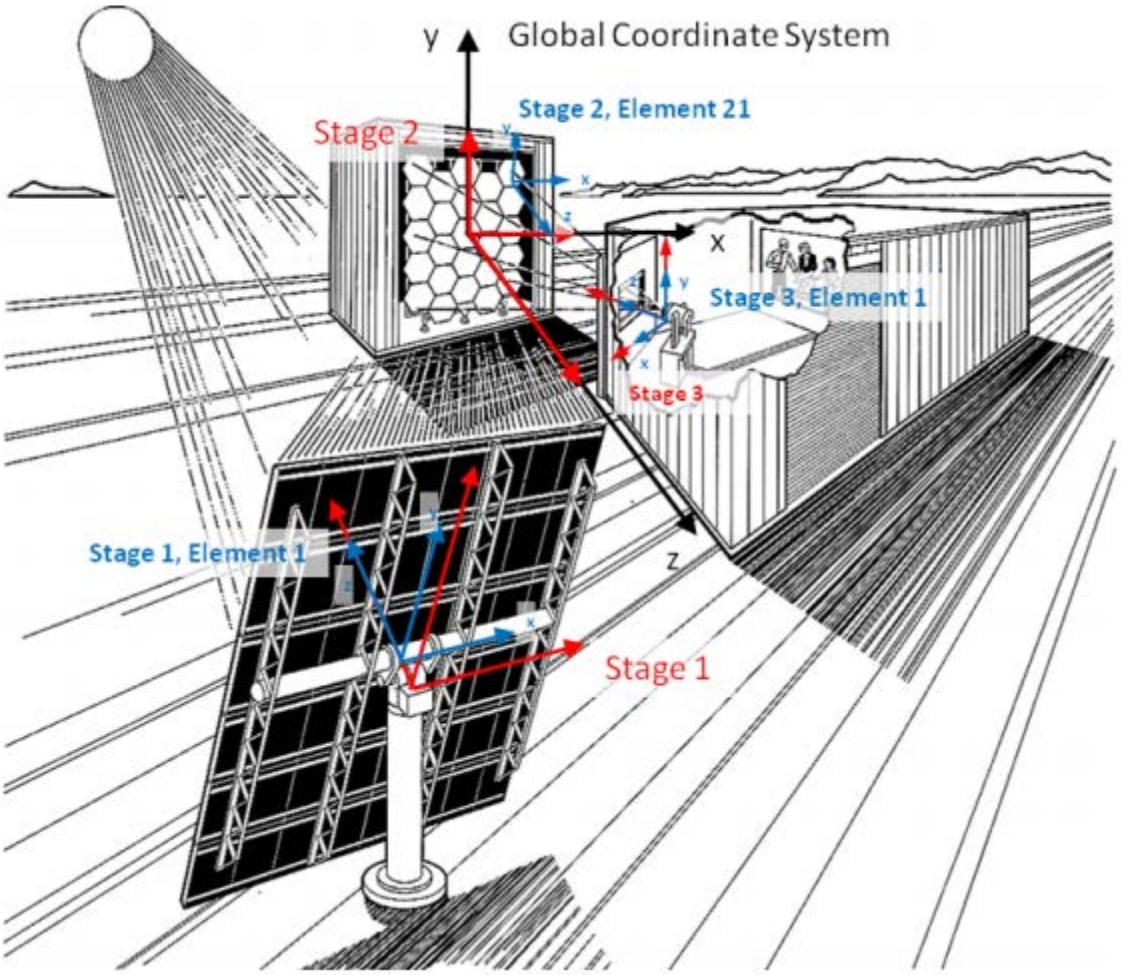

Figure 2.1 -NREL High Flux Solar Furnace SolTrace Diagram. Reprinted from (Wendelin et al., 2013).

2.1.1 Cavity Generation

A function called *SolTrace Cavity Generation* was written for automating the creation of the half octagonal-type cavity receiver stage in *SolTrac*e, based on the PS10 solar power plant's receiver in Seville, Spain. To model this type of cavity receiver in *SolTrace* requires that up to 10 elements must be created; these include 4 for the active panels of the receiver, 4 for the passive paneling of the receiver, including the roof and floor, and 2 for the optional upper and lower "lip" (Figure 2.2). The function is currently limited to a half-octagon geometry, with a symmetric panel size. The function will define the 290 values that are required for modeling the cavity in *SolTrace*. The function requires 8 inputs:

- receiver height
- receiver width
- tower height (which is the distance from the ground to the mid-height of the cavity)
- cavity receiver angle

- coordinate system
- enable/disable receiver lip(s)
- height of each receiver lip (when enabled)

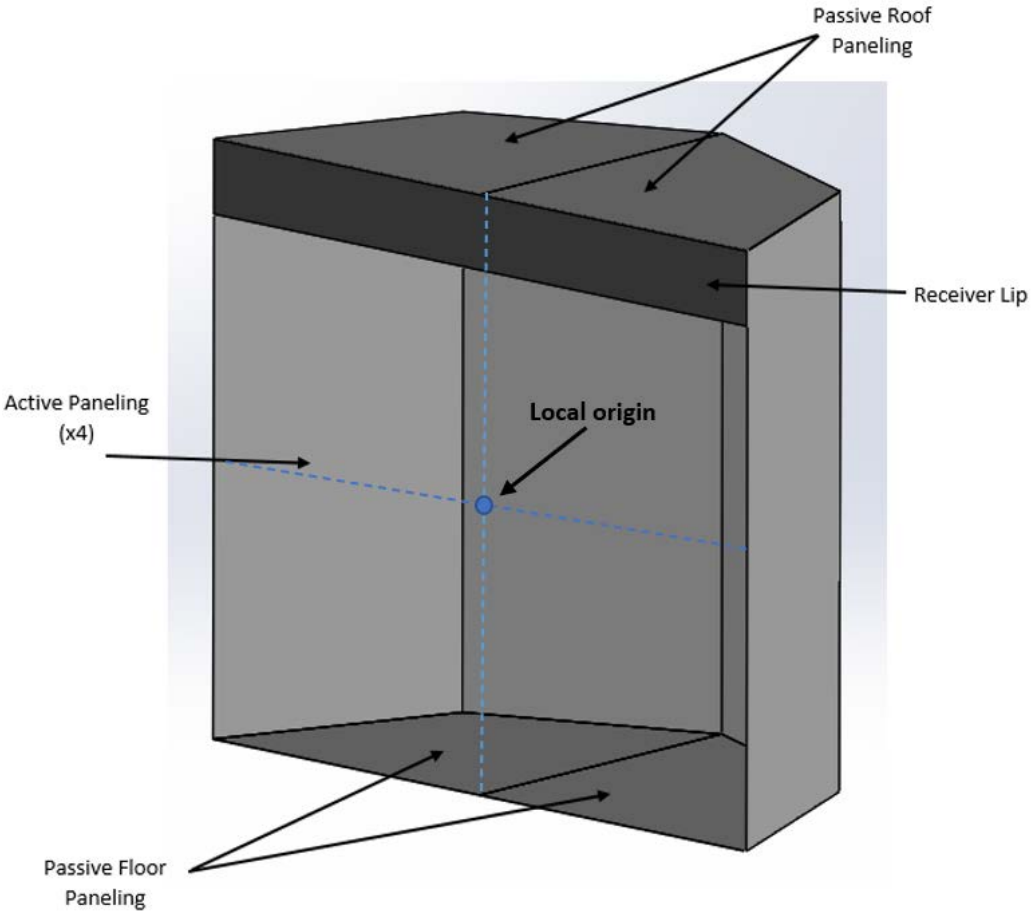

Figure 2.2- Geometric elements of the octagonal cavity. Optional top lip shown.

The first portion of the *SolTrace Cavity Generation* determines the width of each active panel and the distance between the mid-point of the panels and the local origin of the cavity, which are denoted as X and D, respectively, in Figure 2.3. This is, implicitly, set by the definition of the receiver width and found using trigonometric functions for a right-triangle and the 135° interior angle of an octagon. Once these values are found, four panels are created and transformed by a rotation matrix with the rotation angles set as -67.5°, -22.5°, 22.5°, -67.5° to determine their respective coordinates and their aim points as shown in Figure 2.4. The code will then set the panel dimensions, shape, surface, optical, and interaction values.

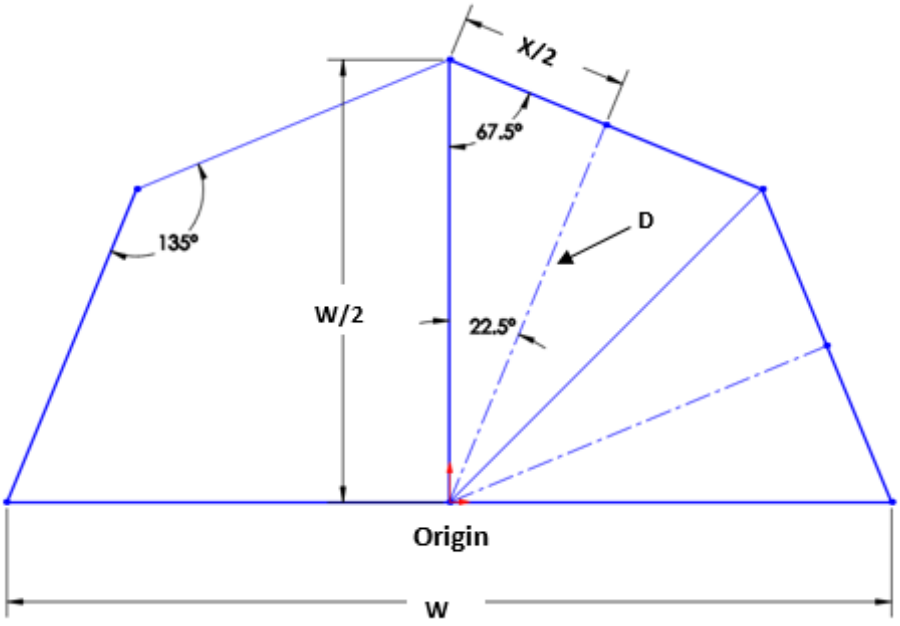

Figure 2.3 - Top view: Panel width and center distance diagram.

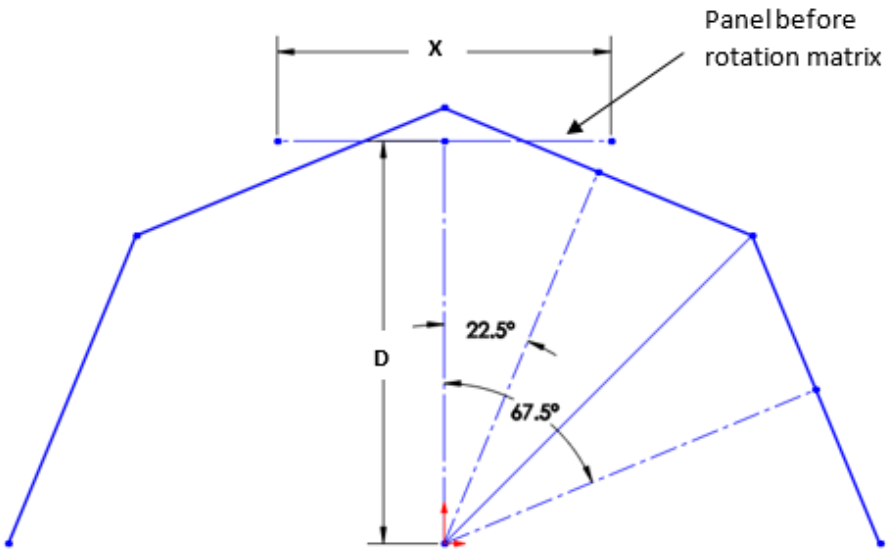

Figure 2.4 - Rotational diagram of panels.

The “passive” panels are created as four quadrilateral elements, two for the roof and two for the floor, which each need four sets of x and y coordinates to define their shape (Figure 2.5). The coordinates are calculated for one panel initially. The first set of coordinates are always zero, as they are located at to the origin of the cavity, the second and third group of coordinates are set by the width of the cavity, and the final coordinates are found using the unit circle relation of cos(45°) and sin(45°) multiplied by half the receiver width. The coordinates are copied for one panel and

reflected for the other two panels using a line of symmetry. The global location of the panels is set by the receiver height, with a +/- value of half the receiver height being added to the relative origin height.

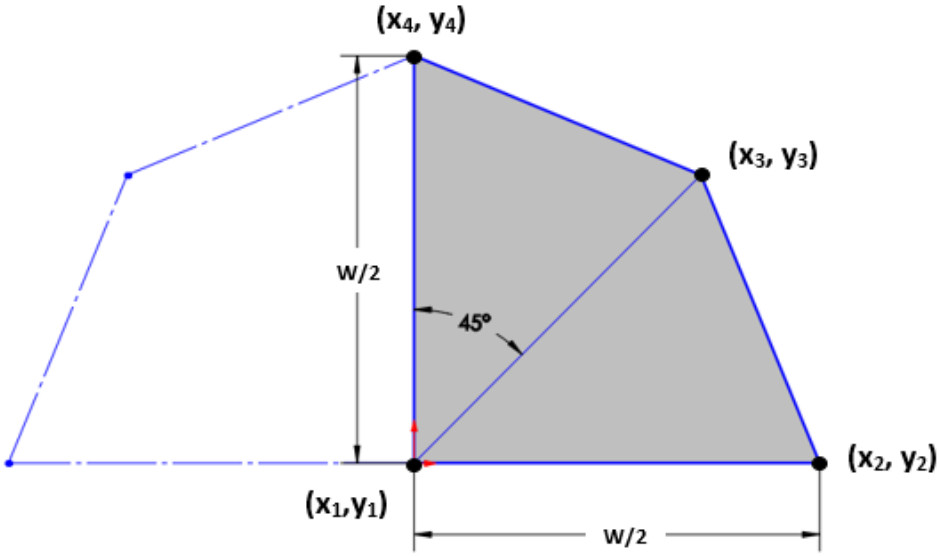

Figure 2.5 - Passive Panels Quadrilateral Elements.

If the cavity lip is enabled, two additional elements will be created at the top and bottom of the cavity at the aperture opening. The width of the lip will be the same as the width of the cavity at the aperture opening, and the heights of each lip are defined by the user. The coordinate system can be set using two different coordinate system conventions, *SolarPILOT (SP)* has the Z-axis set as the zenith, and the *SolTrace (ST)* convention sets the Y-Axis as the zenith (Figure 2.6). A cavity tilt angle can also be defined by the user, with θ_{cav} =0° being parallel to the ground and θ_{cav} =90° being perpendicular to the ground; the axis of rotation is located at half the depth of the cavity (W/4) and half of the receiver height, as shown in Figure 2.7.

Figure 2.6 - Coordinate Systems. Left: SolarPILOT, Right: SolTrace.

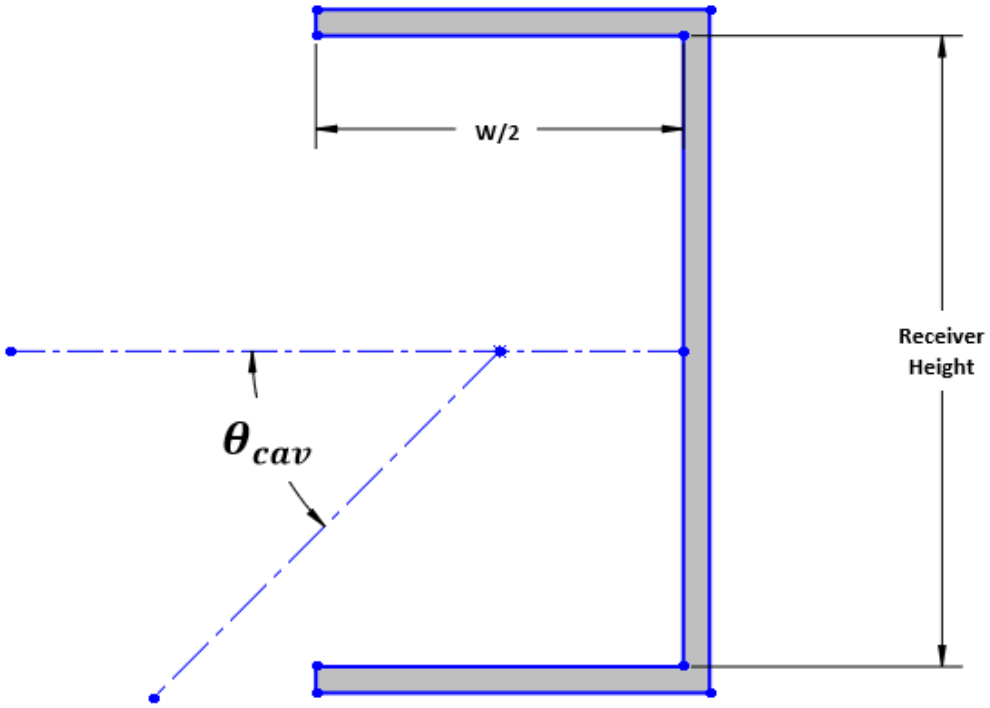

Figure 2.7 - Cross-section side view of cavity tilt angle.

2.1.2 Heliostat Aiming

A function called *Aim Point Generation* was written to accomplish the aim-point calculations that are required when setting the global orientation of an element in *SolTrace*. The heliostat fields that are being modeled have on the order of several thousand individual heliostats (elements), and each heliostat requires a unique set of x, y, and z aim points. The *Aim Point Generation* function creates two normalized three-dimensional vectors based on a heliostat's relative origin, one vector is oriented to the sun ($\vec{S}$) and the other is oriented to a specified location on the receiver where the heliostat's image will be reflected ($\vec{R}$) as seen in Figure 2.8. A third vector $\vec{H}$, which is the heliostat's surface normal, is then solved for using the law of specular reflection. This law states that the angle of incidence (θ_i) must be equal to the angle of reflection (θ_r). The angle of incidence is solved for using the $\vec{S}$ and $\vec{R}$ $vectors$, and then used to calculate the $\vec{H}$ vector. The $\vec{H}$ vector components are the aim points based on the heliostat's local coordinate system. A translation vector is then used to convert those aim points to the global coordinate system.

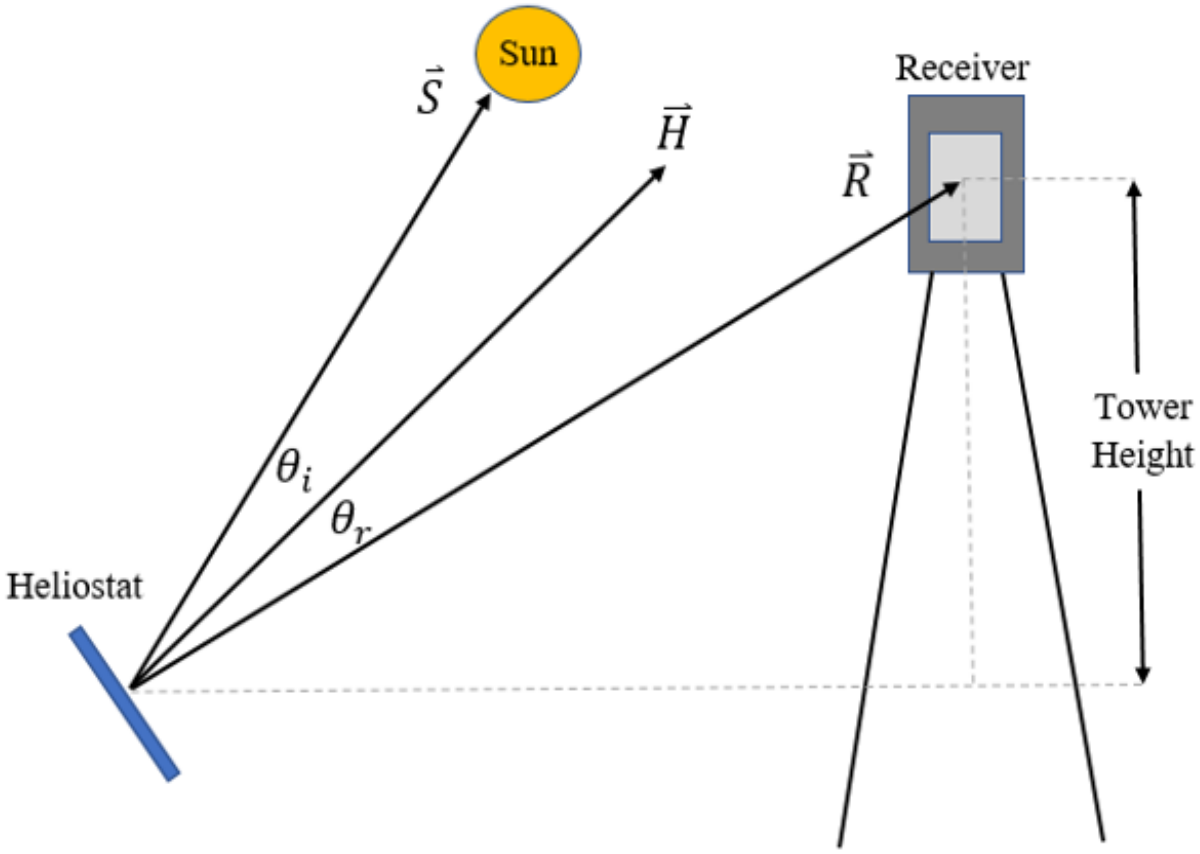

Figure 2.8 - 2D Aim Point Vector Diagram.

2.1.3 Heliostat Field Generation

A function called *Heliostat Field Generation* was written to generate a custom heliostat field based on the cavity receiver's previously defined geometry. The heliostat field angle matches that of the receiver's opening (aperture) which prevents rays from hitting the external surfaces on the side of the cavity. The heliostat field is divided into the number of sections that equals the number of active surfaces comprising the cavity receiver, as seen in Figure 2.9. Each section of the field is oriented so that it is aimed towards a specified panel. The parameters that can be set in this function include: size of the heliostat used in the field, inner and outer radii of the field, distance between

heliostats, location of the field (Northern or Southern facing), and the position of the sun. The script is capable of generating aim points for any sun position throughout the year.

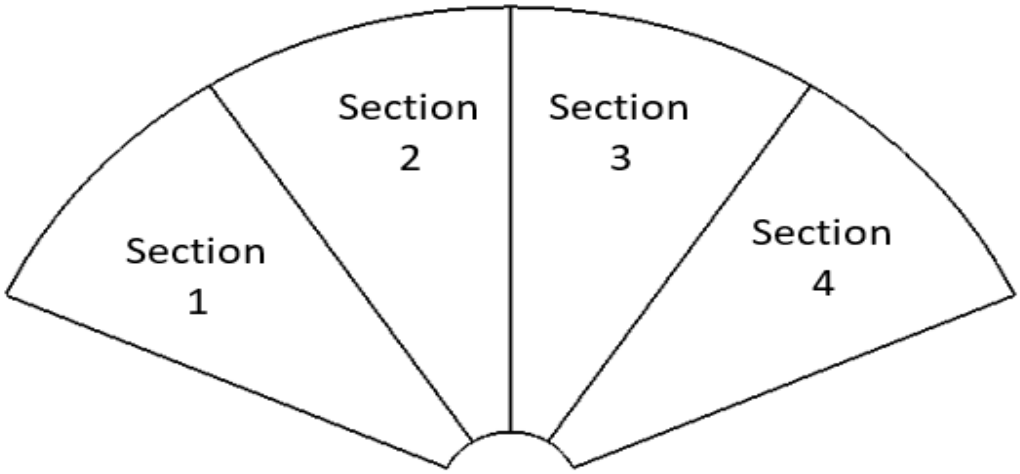

Figure 2.9 - Sectioned Heliostat Field.

2.1.4 Heliostat Field Generation with SolarPILOT

The original function that was created for heliostat field generation did not include any metrics for determining the performance of the field (cosine efficiency, blocking, shading, etc.), and required several iterations to create a uniform flux distribution on the cavity receiver. Therefore, *SolarPILOT*'s methodology for creating an optimized heliostat field was extended and applied to the baseline cavity receiver. An initial calculation is performed using Eqs. (2.1) and (2.2) to determine the minimum radius required so the nearest heliostat can aim through the cavity's aperture (R_{min}). The vertical offset in these formulas, is the distance between the bottom of the cavity and the location where the heliostat is aiming. This is the absolute minimum offset distance for the heliostat field from the base of the tower, as anything closer will result in a portion of the nearest heliostats' projected images being blocked by the cavity floor. The *SolarPILOT* aiming algorithm, as well as these formulas, can be modified in the future so that the heliostats nearest to the tower base aim towards the top of the cavity, which will reduce the minimum radius of the field.

$$\theta_{acceptance} = tan^{-1}\left(\frac{Vertical\ offset}{W/2}\right) \tag{2.1}$$

$$R_{min} = \frac{[Tower\ Height - (W/2) + Vertical\ Offset]}{tan(\theta_{acceptance})} \tag{2.2}$$

SolarPILOT's current capabilities allow the uniform generation of incident flux for a single plate but this feature of the software can be used to create a portion of the heliostat field for each of the four active panels of the cavity. This is accomplished by separating the heliostat field into four equal sections and transforming the sun's global position into four relative positions for each section. The layout of each section is based on the centerline of the panel that the heliostats will

be targeting. Figure 2.10 and 2.11 show the section layout that is required for panel 1 (P1) and panel 2 (P2), respectively. As shown, the field requires an offset for each of the four panels, with panels 3 and 4 being a reflection of panels 1 and 2. Once each of the field sections are created, they are rotated and combined to create a complete field. The flux maps from an example field can be seen in Figure 2.12. The field that was used was relatively small, using only 148 heliostats. Due to the small field size, the distribution was not completely uniform. With the use of a larger field, the distribution would become more uniform across all the panels.

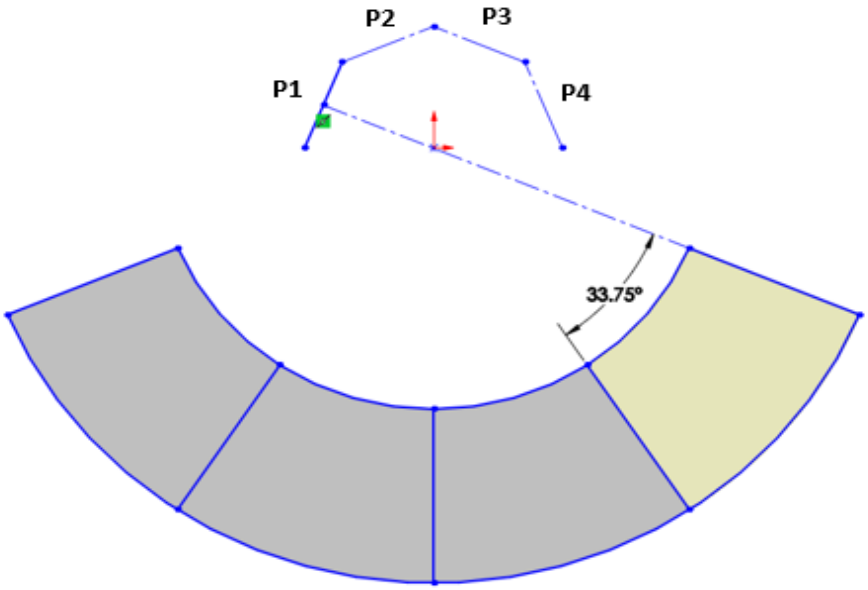

Figure 2.10 - Panel 1 heliostat section layout.

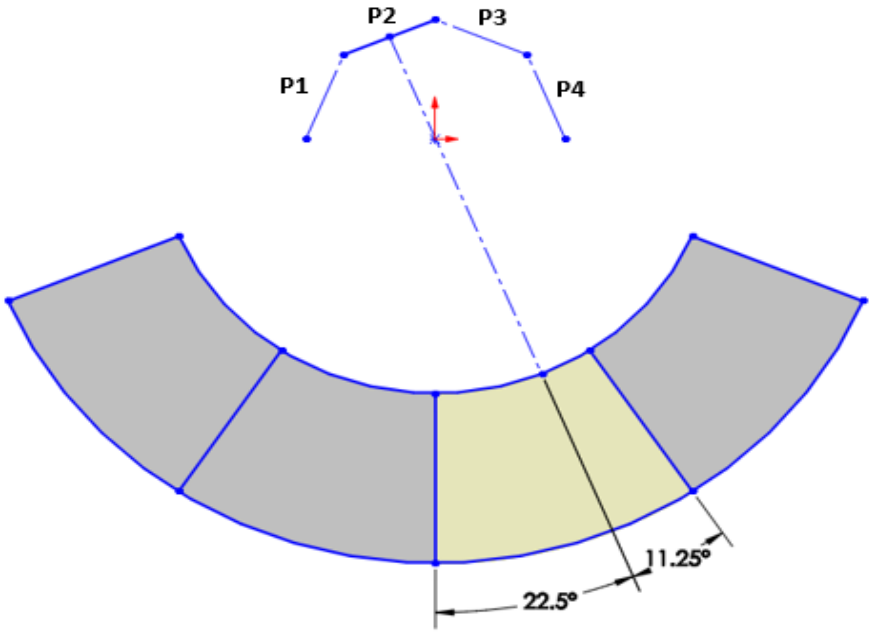

Figure 2.11 - Panel 2 heliostat section layout.

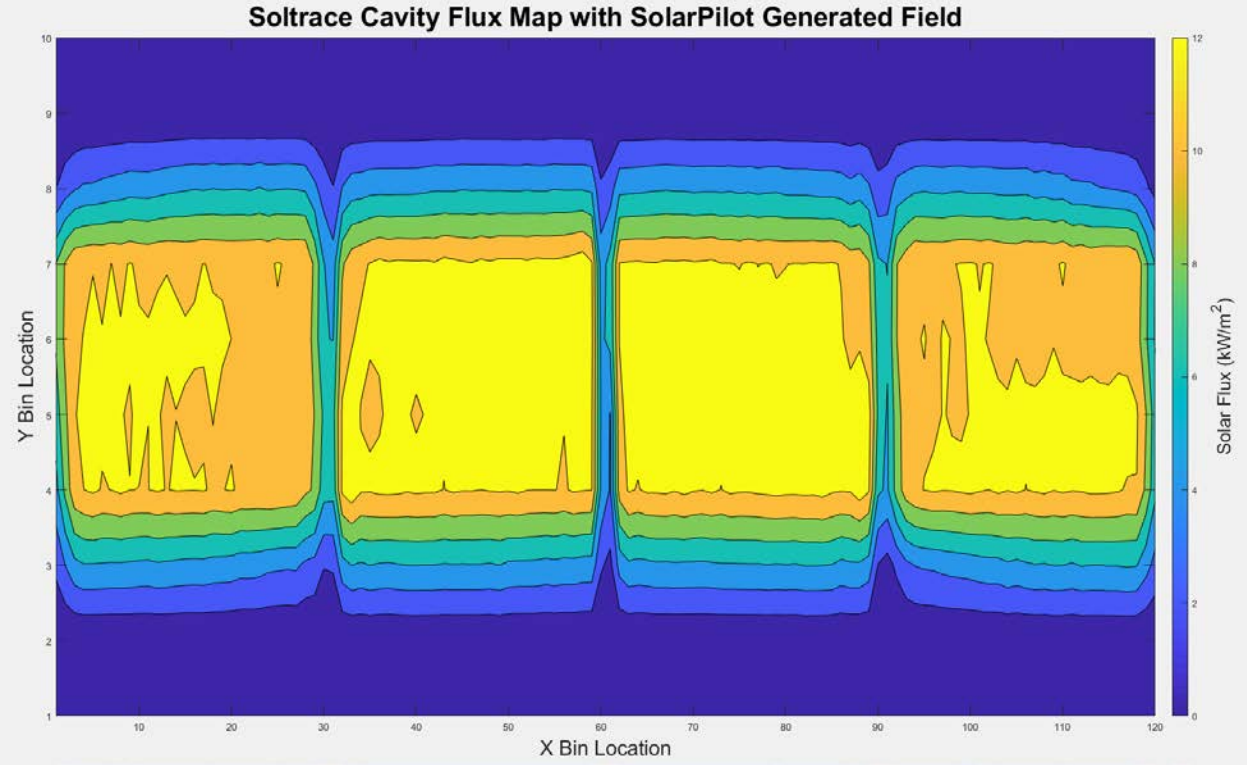

Figure 2.12 - Flux map of cavity receiver with SolarPILOT generated heliostat field.

2.1.5 DELSOL3 Comparison

A comparison between *DELSOL3* and *SOLTRACE* was carried out in order to examine differences between the solar flux maps associated with the two programs at seven different times during the day. The receiver created in *SolTrace* was a half octagon cavity with dimensions of 22.44 m wide by 19.745 m high with a tower height of 174.2 m. The lip height of the receiver was 1.78 m and the plant location was Dagget, California. The *DELSOL3* receiver was a half cylinder with the same cavity depth and height. The heliostat field was imported into *SolarPILOT* from *DELSOL3*, and then moved to *SolTrace*. To find the height of the cavity, Eqs. (2.3-2.5) were used which can be found in the *DELSOL* 3 manual (Kistler, 1986). The variable *HBOT* is the height location that is required so that the closest heliostats can target the top of the active panels. The variable *HTOP*, the top of the cavity height is set by 1.1 times the height of the aperture height (*Ry*). *HBOT* and *HTOP* can then be used to find the height of the cavity.

$$\mathrm{HBOT} = \left(\mathrm{THT} - \frac{\mathrm{RY}}{2}\sin(180 - \mathrm{RELV})\right)\left(\frac{\mathrm{RMAX} - \frac{\mathrm{W}}{2} + \frac{\mathrm{W}}{2}\cdot \mathrm{RWCAV}}{\mathrm{RMAX} - \frac{\mathrm{W}}{2} + \frac{\mathrm{RY}}{2}\cos(180 - \mathrm{RELV})}\right) \qquad (2.3)$$

$$\mathrm{HTOP} = 1.1\mathrm{xRy} \qquad (2.4)$$

$$HCAV = HTOP - HBOT \tag{2.5}$$

The *SolTrace* models used a simulation size of 5 million ray intersections. The flux points were separated into a flux map of 12 by 10 elements, in the horizontal and vertical direction, respectively, to match the flux maps of *DELSOL3*. The *SolTrace* flux maps were similar in distribution and magnitude to that of *DELSOL3*; however, there were some notable differences. First, the *DELSOL3* flux maps have a more uniform flux distribution compared to *SolTrace*. Secondly, the *SolTrace* peak solar flux location does not deviate from the center of the image as much as the *DELSOL* maps do at earlier/later times during the day. Finally, the *SolTrace* flux maps have higher peak solar flux values and lower average flux values compared to their *DELSOL3* counter-part. The percent error of *SolTrace*'s flux maps when comparing the average flux values are constant at 24-26%, and the peak flux percent error was constant at 4-6%. Flux maps of one of the days simulated can be seen in Appendix A.

The main reason for this deviation in average flux intensity is that the total energy that *DELSOL* is reporting as being delivered to the cavity is approximately identical to the energy incident on the heliostat field. This suggests that the software is not including any losses such as atmospheric attenuation, reflectivity of the heliostat, and the absorptivity of the cavity. Another reason that may account for some of the deviation in the flux maps are that the cavities are not identical. The *SolTrace* model, which is closer to the half-cylinder shape may lower the peak flux values and increase the average distribution as the reflected rays will have more distance to spread out on the receiver before intersecting a wall. Also due to the Monte-Carlo simulation, the entire heliostat image is not being simulated very well as each heliostat on average is being characterized by only 1,346 rays.

2.2 *Tonatiuh* Comparison Study

A similar comparison study was conducted between *SolTrace* and *Tonatiuh*, a ray tracing optical software developed by the National Renewable Energy Center (CENER) of Spain, due to the issues encountered with *DELSOL3*. The cavity generated for both programs was a half octagonal shape (4 panels) with a height of 19.745 m by 22.44 m wide. Seven cases were simulated for different azimuth and zenith angles with a constant DNI of 950 W/m^2. The absorptivity value of the cavity was set to 1, the heliostats were set to a reflectivity value of 0.85, and the heliostat slope error was set to 2 mrad. The sun shape was chosen to be a Buie CSR distribution (Buie et al., 2004) with a circumsolar ratio of 0.6 in *SolTrace* as seen in Figure 2.13. which is equal to a 0.6083 corrected circumsolar ratio. The Buie CSR ratio is a distribution developed from the Lawrence Berkley Laboratory circumsolar database and sunshapes published by the German Aerospace center. *Tonatiuh*'s circumsolar ratio was set to the corrected value of 0.6083. The same heliostat-field was used for all cases with a simple aim-point strategy, which was setup to aim at the center of the aperture of the cavity located 174.92 m above ground-level.

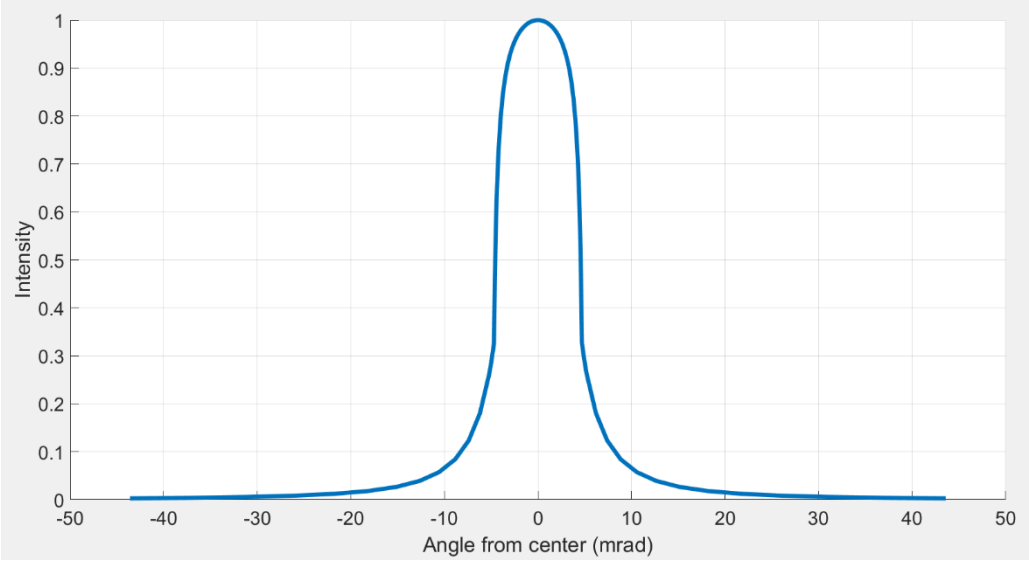

Figure 2.13 – SolTrace Buie CSR distribution.

The flux maps for *SolTrace* and *Tonatiuh* were compared by their respective average flux profiles, maximum flux, and their absorbed power for a simulation of 5 million rays. From the seven cases, the average difference across all cases between the average flux maps was 2.22% and 4.43% when comparing their maximum flux values. The power difference between the two was calculated to be 2.22%. *SolTrace* had a higher average flux value compared to *Tonatiuh*, but lower peak flux values. The higher average flux values can be attributed to *SolTrace* delivering a slightly larger amount of power to the receiver, which is most likely due to differences in the power calculations by the two programs. The lower peak values may be attributed to differences in the ray-tracing algorithms. Thirty samples were taken and averaged from *Tonatiuh* to determine the percent deviation with a 95% confidence. The deviation for the average flux was $\pm$0.59% and $\pm$4.93% for the peak flux values.

Table 2 shows each of the percent differences associated with each of the seven cases for average flux, maximum flux, and power with the Tonatiuh flux as the base. Flux maps for two case can also be seen in Appendix A in terms of kW/m^2 with the blacked dotted lines showing the location of each of the four cavity panels. For each case, the flux maps are similar in shape and magnitude, again with *SolTrace* having a higher average flux and lower peak flux. A mean average difference value of all the nodal flux values was also calculated to determine local differences between flux maps (MAE) using Eq (2.6), with N, M, and q being the nodes in the vertical direction, horizontal direction, and the flux at not i,j.

$$MAE = (N * M)^{-1} \sum_{i=1}^{N} \sum_{j=1}^{M} \left| q_{i,j}^{soltrace} - q_{i,j}^{tonatiuh} \right| \tag{2.6}$$

Case	Azimuth Angle (°)	Zenith Angle (°)	Average Flux Difference (%)	Max Flux Difference (%)	Power Difference (%)	**MAE**
1	69.8	13.5	+2.02	-2.79	+2.02	11.05
2	77.2	25.3	+2.35	-5.61	+2.35	14.17
3	94.6	37.5	+2.52	-4.52	+2.52	16.48
4	92.9	49.8	+1.94	-4.22	+1.94	17.64
5	104.3	61.9	+2.35	-4.07	+2.35	19.08
6	125.4	73.2	+2.14	-4.67	+2.14	18.37
7	180	79.3	+2.24	-5.14	+2.24	19.05
Average	-	-	**+2.22**	**-4.432**	**+2.22**	**16.55**

Table 2 - Comparison Values between SolTrace and Tonatiuh (base for calculations).

3. Radiation Heat Transfer

SolTrace allows for the incident solar radiation (short wavelength) that will be incident on each active panel in a cavity-type receiver to be predicted. The next step in the process requires the prediction of the radiative exchange within the cavity and with its surroundings. The cavity surfaces will be modeled as diffuse semi-gray bodies with the spectral distribution of radiation being modeled in two bands: short-wave and a long-wave. Using two bands enables more accurate modeling of both the radiative energy absorbed and lost from the cavity since surface absorptivity & emissivity that are functions of wavelength can be considered. The selective surfaces and coatings used in solar technology will preferably have high absorptivity in the short-wavelength region and low emissivity in the long-wavelength region. These properties reduce solar (short wavelength) and thermal (long wavelength) losses, respectively, and lead to higher overall efficiencies for the system.

The receiver's absorptivity, α, in the short-wave region will determine how much of the incoming solar radiation that was predicted by SolTrace is absorbed by the panels and how much is reflected (ρ), with $\alpha+\rho=1$. The active surfaces of a cavity receiver will emit long-wave radiation based on its surface temperature and long-wave emittance and exchange long-wave radiation with other panels or passive surfaces within the cavity operating at a different temperature as well as losses to the ambient environment through the aperture opening.

3.1 Mesh

Since the incident radiative flux may not be uniform on all receiver panels and also to allow flexibility in the routing of the HTF and evaluation of features such as lips, it is necessary to partition the receiver's surfaces into separate elements. A MATLAB function was created for a

half octagon geometry (PS10 design) with optional upper and bottom lips; this function is the Cavity_Mesh_Function. The panels are meshed by specifying the number of elements in the horizontal and vertical direction, panel_n and panel_m respectively. Currently the code requires all active panels to have the same n by mesh arrangement. The roof and floor of the cavity are also meshed in the same manner as cover_n & cover_m, with a limit of a 4 x 3 set of elements as seen in Figure 3.2. The total numbers of elements in the domain is defined by Eq. (3.1). Since there are four panels in the cavity design, the number of panel elements is multiplied by four. The cover elements are multiplied by two since there is an identical floor and roof surface. The aperture is defined as a single element, and the number of lips, N_{lips}, can be either zero (no lip), one (top lip), or two (top and bottom lip).

$$N = (panel_n \cdot panel_m) \cdot 4 + (cover_n \cdot cover_m) \cdot 2 + 1 + N_{lips} \tag{3.1}$$

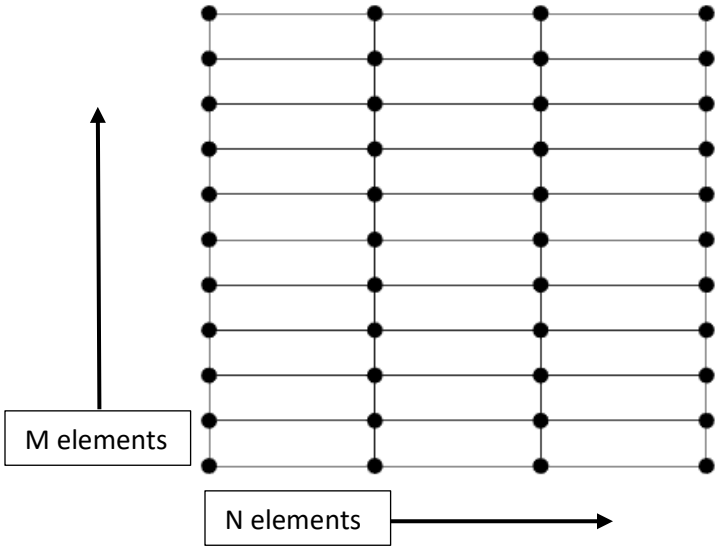

Figure 3.1 - Cavity active panel mesh example.

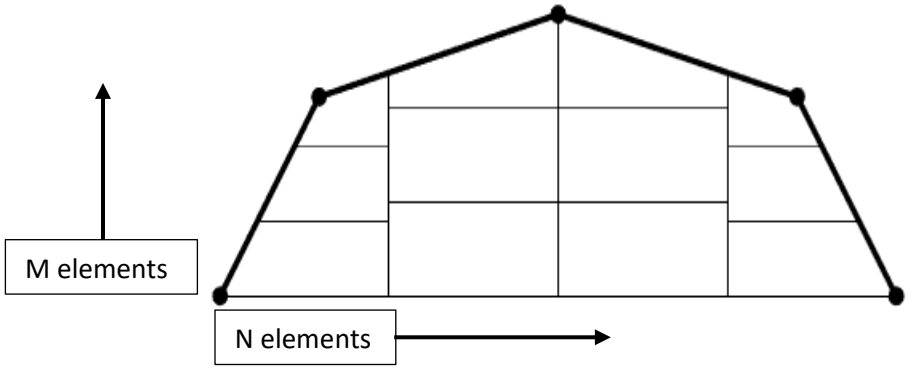

Figure 3.2 - Cavity passive roof/floor mesh example.

3.2 View Factor

To determine the radiation exchange between elements, view factors must be calculated for each element to element permutation. The view factor is a quantity that is used in the calculation of blackbody radiation exchange but can also be used in other methods for semi-gray bodies, as discussed in the subsequent sections. The view factor between two surfaces is defined as the fraction of radiation that leaves a surface and directly strikes another surface. Assuming that all the elements are blackbodies ($\alpha=\varepsilon=1$) and diffuse emitters, view factors can be used directly to determine the radiation heat transfer between multiple surfaces/elements. To calculate each view factor for the PS10 type cavity, two methods are used: numerical integration and Monte Carlo ray tracing. The numerical method to calculate the view factors for rectangles whose edges are parallel and share a common intersection line was developed by (Gross et al., 1981) This numerical method will be used to calculate the view factors for panel to panel, panel to the aperture, panel to the top lip, and panel to the bottom lip elements. To calculate the view factor between two of the rectangular elements, their length, width, orientation, are defined by nine values (x_1, x_2, y_1, y_2, etc.) as seen in Figure 3.3.

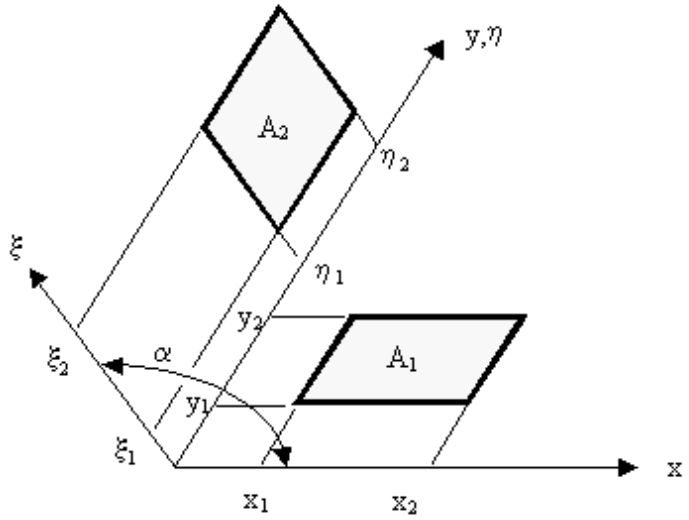

Figure 3.3. View factor between two rectangles with parallel edges with common intersection line. Reprinted from (Gross et al., 1981).

To calculate the view factor, a function G is evaluated 8 times with numerical integration (3.2). The numerical integrations in the code are done by MATLAB's numerical integration function. The values of G are then summed and divided by the area of the rectangle defined by the x and y values, denoted as A_1 (3.3). The resulting value represents the view factor and represents the radiation that leaves element 1 and reaches element 2. Reciprocity is then used to calculate the view factor from element 2 to 1 as given by equation 3.4.

$$G = -\frac{(\eta - y)\sin^2\alpha}{2\pi}\int_{\xi}\left(\frac{(x-\xi\cos\alpha)\cos\alpha - \xi\sin^2\alpha}{\left(x^2 - 2x\xi\cos\alpha + \xi^2\right)^{1/2}\sin^2\alpha}\tan^{-1}\left[\frac{\eta - y}{\left(x^2 - 2x\xi\cos\alpha + \xi^2\right)^{1/2}}\right]\right.$$
$$+\frac{\cos\alpha}{(\eta - y)\sin^2\alpha}\left\{\left[\xi^2\sin^2\alpha + (\eta - y)^2\right]^{1/2}\tan^{-1}\frac{x - \xi\cos\alpha}{\left[\xi^2\sin^2\alpha + (\eta - y)^2\right]^{1/2}} - \xi\sin\alpha\tan^{-1}\left(\frac{x - \xi\cos\alpha}{\sin\alpha}\right)\right\} \tag{3.2}$$
$$\left.+\frac{\xi}{2(\eta - y)}\ln\left[\frac{x^2 - 2x\xi\cos\alpha + \xi^2 + (\eta - y)^2}{x^2 - 2x\xi\cos\alpha + \xi^2}\right]\right)d\xi$$

$$F_{1-2} = \frac{1}{A_1}\sum_{i=1}^{2}\sum_{j=1}^{2}\sum_{k=1}^{2}\sum_{l=1}^{2}\left[(-1)^{(i+j+k+l)}G(x_i, y_j, \eta_k, \xi_l)\right] \tag{3.3}$$

$$F_{i,j}A_i = F_{j,i}A_j \tag{3.4}$$

For an enclosure, all the radiation emitted from a surface must strike a surface, so that the sum of view factors from $F_{1,N}$ to $F_{N,N}$ for N surfaces must equal one. Not every element to element view factor is a non-zero value. For example, elements on the same panel lie on the same geometric plane cannot "see themselves"; therefore, these element view factors will be zero.

3.3 Monte-Carlo

Monte-Carlo ray tracing is a technique used to numerically determine the view factors for elements that are irregular quadrilateral, where no analytical or numerical equation currently exists. This technique is used for determining view factors for elements on the roof/floor of the cavity. The Monte Carlo method has three steps for calculating the view factor for these elements. First, one element is chosen to be the emitter, with a randomly generated position being selected on the element's surface as the origin of the ray. Then, two random angles, phi and theta are generated. Finally, the intersection of this emitted ray with the plane of the target element is calculated and is determined to intersect the target element, "a hit", or not "a miss". These three steps are repeated for a set number of rays. The fraction of hits to the number of generated rays provides an estimate of the view factor. Since the value calculated for this method is probabilistic, the number of rays chosen to be generated can have an impact on the uncertainty associated with the view factor estimate. For example, using the mesh seen above and changing the number of generated rays from five thousand to five million using 30 samples, the max deviation goes from 17.9% and 0.57% respectively within a 95% confidence interval. The number of rays for an accurate solution is dependent on the two surfaces relative size, distance, and spatial orientation to each other.

The ray emission direction probability for step two of the Monte Carlo method is defined by Eqs. (3.5) and (3.6), which is a diffuse and uniform distribution (Nellis and Klein, 2009). P_θ and P_φ are randomly generated number between 0 and 1, and used to solve for an angle θ and φ.

$$P_\theta = sin^2(\theta) \tag{3.5}$$

$$P_\phi = \frac{\phi}{2\pi} \tag{3.6}$$

The unit vector representation of the generated ray, $\underline{\mathbf{r}}$ is stated in (3.7). This unit vector can be used to determine the intersection point on the target element's plane.

$$\underline{\boldsymbol{r}} = [\cos(\phi)\sin(\theta)]\underline{i} + [\sin(\phi)\sin(\theta)]\underline{j} + [\cos(\theta)]k \tag{3.7}$$

To determine if the intersection point between the ray and the target element's geometric plane is contained within the target element for irregular polygons, a "point in polygon" function was created (PIP Function). When using the point in polygon function for one of the irregular quadrilateral cavity elements, the function first calculates the slopes (m) and y-intercepts for all four lines. Then for each line, the x and y coordinate of the intersection point are used to create two new x and y values using the corresponding linear equations. These two new x and y values are used as conditional values that the intersection point is compared against to determine if the point lies within the polygon.

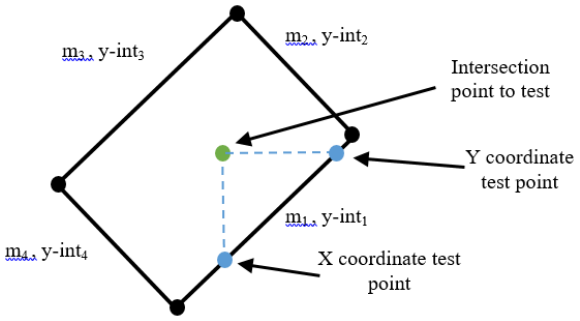

Figure 3.4. Point in Polygon (PIP) function test points for line 1.

3.4 Radiosity

Now that the view factors for the cavity system can be calculated, determining the radiation exchange between the cavity surfaces can be analyzed. Two methods to perform this analysis were considered: Radiosity and F-hat, with radiosity being the most widely known method. For this method, three terms are introduced, $E_{b,i}$, G_i and J_i which are the blackbody emissive power of surface i, incident flux (irradiation) on surface i, and the total heat flux leaving surface i respectively.

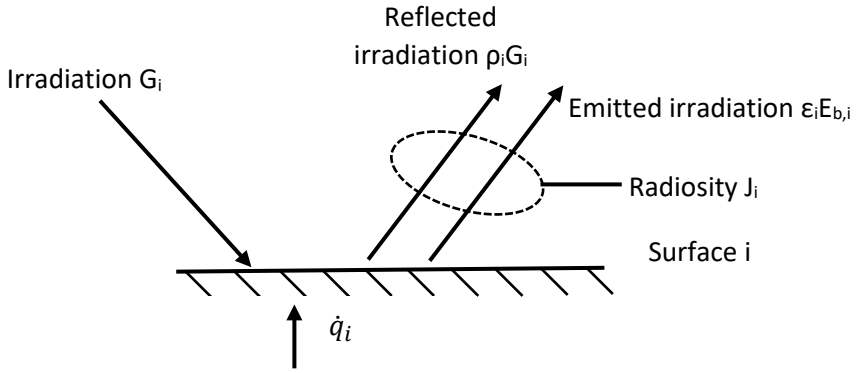

Figure 7.5. Definition of radiosity for surface i. (Nellis, & Klein, 2009).

The net radiation exchange on surface i can be expressed as the incoming radiation (irradiation) minus the radiation leaving (radiosity).

$$\dot{Q}_i = A_i \cdot J_i - A_i \cdot G_i \tag{3.8}$$

Since the reflectivity of the surface is related to the emissivity, Eq (3.8) can be rewritten as Eq (3.9).

$$\dot{Q}_i = \left(\frac{\varepsilon_i \cdot A_i}{1-\varepsilon_i}\right) \cdot \left(E_{b,i} \cdot J_i\right) \tag{3.9}$$

To set up a system of equations that has N surfaces, Eqs (3.10) and (3.11) can be used. It should be noted that the radiosity method only provides the net heat transfer rate for a surface, and not the surface-to-surface radiation transfer. Also, since the system of 2N equations is dependent on temperature, the equations must be solved several times when using an iterative solver such as the one implemented in the next stage of the code. Due to these factors, the radiosity method was not used.

$$\dot{Q}_i = \left(\frac{\varepsilon_i \cdot A_i}{1-\varepsilon_i}\right) \cdot \left(E_{b,i} - J_i\right) for\ i = 1 \ldots N \tag{3.10}$$

$$\dot{Q}_i = A_i \cdot \sum_{j=1}^{N} F_{i,j}\left(J_i - J_j\right) for\ i = 1 \ldots N \tag{3.11}$$

3.5 F-hat

Another method for solving radiation problems involving grey-surfaces, is the $\hat{F}$ (F-hat) method (Beckman, 1971). The $\hat{F}$ parameter is similar to the view factor F, with the only difference being that the $\hat{F}$ value represents the ratio of radiation leaving a surface and strikes another surface (directly or indirectly) to the total radiation leaving the surface. For example, $\hat{F}_{i,j}$, is the ratio of the radiation that leaves surface I and strikes surface j directly and through all other indirect paths, via reflections off other surfaces, to the total radiation leaving surface i.

Consider a simple three surface problem as shown in Figure 3.6 to explain the process of setting up the formulation for calculating the $\hat{F}$ parameter. For this problem, the nine view factors are calculated in the normal way, either by analytical, numerical, or Monte Carlo methods (Fi,i , Fi,j, Fi,k , Fj,i, etc.). To convert the view factors F into the $\hat{F}$ parameters, the indirect radiation from the emitting to target surface needs to be added to the view factor.

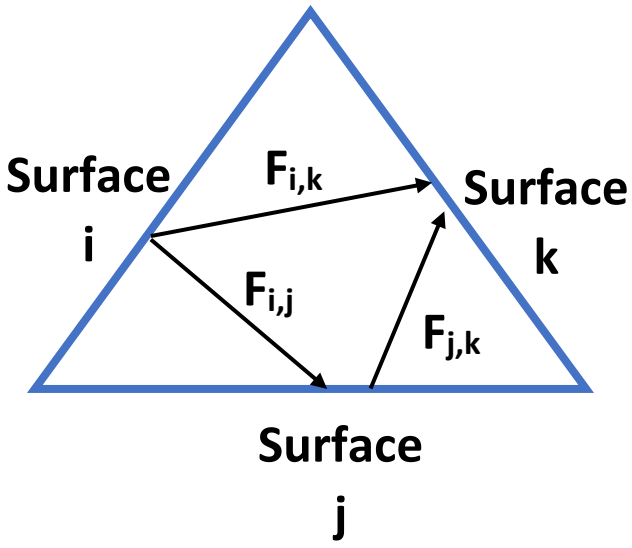

Figure 3.6. Three surface radiation problem.

The component of direct radiative exchange between surface i and j is represented by the view factor $F_{i,j}$. When looking at radiation coming from surface i to j, the indirect radiation can come from any of the three surfaces through a series of reflections and end up being absorbed by surface j. The indirect radiation coming from surface k can be described by $F_{i,k}$, based on the radiation that directly goes from surface i to k, the reflectivity of surface (ρ_k), and the radiation from surface k that will directly and indirectly hit surface j ($\hat{F}_{k,j}$). When these terms are combined and the same is done for indirect radiation from surface i and j, Eq (3.12) results. It should be noted that this equation is implicit, as the $\hat{F}$ values are needed to calculate themselves. Eq (3.12) can be rewritten for N surfaces as seen in Eq (3.13).

$$\hat{F}_{i,j} = F_{i,j} + F_{i,i}\rho_i\hat{F}_{i,j} + F_{i,j}\rho_j\hat{F}_{j,j} + F_{i,k}\rho_k\hat{F}_{k,j} \tag{3.12}$$

$$\hat{F}_{i,j} = F_{i,j} + \sum_{n=1}^{N} \rho_n F_{i,n}\hat{F}_{n,j} \quad for\ i = 1..N\ \ and\ j = 1..N \tag{3.13}$$

The implicit formulation can be used in solvers such as the Engineering Equation Solver (EES) that do not require an explicit form of an equation; however for computer languages that require explicit assignments, such as MATLAB or C++, the equations (3.12) and (3.13) by themselves are not directly useful. The implicit form of Eq (3.13) can be rearranged into an explicit form with a few mathematical operations. The implicit form of Eq (3.13) is first stated in matrix form (3.14).

$$\left[\hat{F}\right] = F + \left[F\rho\hat{F}\right] \tag{3.14}$$

The $F\rho\hat{F}$ term on the right side of this equation can be subtracted on both sides. This will lead to:

$$\left[\hat{F}\right] - \left[F\rho\hat{F}\right] = F \tag{3.15}$$

Then factoring out the common $[\widehat{F}]$ term on the left side of the equation, we will be left with an identity matrix (I) minus the view factor times the reflectivity.

$$\left[\hat{F}\right][I - F\rho] = F \tag{3.16}$$

The $\hat{F}$ parameter can then be isolated by multiplying the inverse of the term that contains the identity matrix, which leads to an explicit form.

$$\left[\hat{F}\right] = [I - F\rho]^{-1}F \tag{3.17}$$

Since all the energy emitted needs to be absorbed, Eq (3.18) must be satisfied. This calculation can be performed as a check to ensure that the $\hat{F}$ values are correct.

$$\sum_{j=1}^{N}\left(1 - \rho_j\right)\hat{F}_{i,j} = 1 \quad for\ i = 1..N \tag{3.18}$$

The $\widehat{F}$ parameters can be used to determine the rate of radiation heat transfer for both the short-wave (solar) and long-wave (thermal) bands. The net radiation transfer for surface i for both modes are defined by Eqs (3.19) and (3.20) respectively.

$$\dot{Q}_{solar,i} = A_i \sum_{j=1}^{N} \hat{F}_{i,j}\left[Flux_{solar,i}(1 - \varepsilon_i)\varepsilon_j \; - \; Flux_{solar,j}\left(1 - \varepsilon_j\right)\varepsilon_i\right] for\ i = 1\ldots N \tag{3.19}$$

$$\dot{Q}_{thermal,i} = \varepsilon_{i,thermal}A_i\sigma \sum_{j=1}^{N} \varepsilon_{j,themal}\hat{F}_{i,j}\left(T_i^4 - T_j^4\right) for\ i = 1\ldots N \tag{3.20}$$

3.6 Example Radiation Problem with Radiosity and F-hat method

To show how both radiosity and the F-hat method can be used to solve a radiation heat transfer problem, a three surface example taken from chapter 10 of (Nellis & Klein, 2009) is solved using both methods. The example shown in Figure 3.7 and has two identical parallel plates at different temperatures with surface-dependent emissivity. The third surface in the problem is the surroundings.

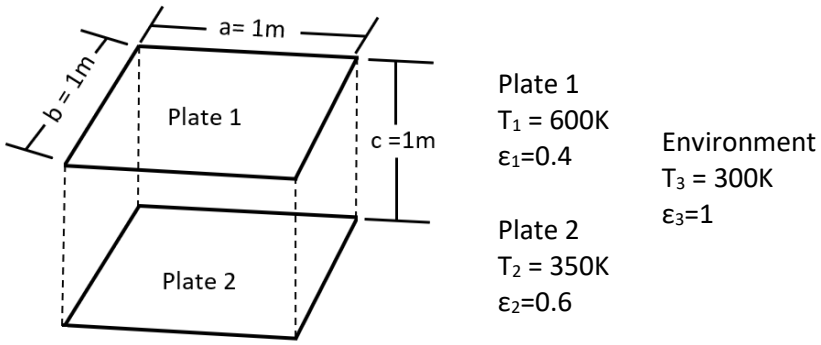

Figure 3.7. Three surface example problem of two parallel plates at a finite distance.

The first step of the process involves calculating the view factors between each surface to surface interaction with surface 1, 2, and 3 defined as Plate 1, Plate 2, and the environment respectively. Since the radiation emitted by surface 1 and 2 cannot directly strike themselves, those view factors ($F_{1,1}$ and $F_{2,2}$) will be zero. The view factors for surface 1 to 2 and 2 to 1 ($F_{1,2}$ and $F_{2,1}$) can be found using Eq. (3.21), with X and Y being the ratio of the length and width of the plates to the separation distance, respectively (Howell, 1982). The view factors in this example are calculated to be 0.1998.

$$F_{1-2} = \frac{2}{\pi XY}\left\{\begin{array}{l} ln\left[\frac{(1+X^2)(1+Y^2)}{1+X^2+Y^2}\right]^{1/2} + X\sqrt{1+Y^2}\,tan^{-1}\frac{X}{\sqrt{1+Y^2}} \\ +Y\sqrt{1+X^2}\,tan^{-1}\frac{Y}{\sqrt{1+X^2}} - X\,tan^{-1}X - Y\,tan^{-1}Y \end{array}\right\} \tag{3.21}$$

The view factors $F_{1,3}$ and $F_{2,3}$ can be calculated using the enclosure rule. Subtracting the view factors calculated by Eq (3.21) from 1, equals 0.8002. Since $F_{1,1}$ and $F_{2,2}$ are zero, they are excluded from these calculations. Lastly, to determine the view factors for surface 3, the reciprocity theorem defined in Eq. 3.4 can be used, using an arbitrary value for the area of the environment. If a large value is used for the surrounding area then $F_{3,1}$ and $F_{3,2}$ are small, and $F_{3,3}$ being approximately equal to 1. Because the product of area and view factor is the important parameter, the area used for the surroundings is not important. The EES code used for this example can be seen below.

```
"EES Sample Radiation Problem"
$UnitSystem SI MASS RAD PA K J
$TABSTOPS 0.2 0.4 0.6 0.8 2.5 in

"Dimensions"
a=1[m]                          "Length of plates"
b=1[m]                          "Width of plates"
c=1[m]                          "Distance between plates"

"Temperatures"
T[1]=600[K]                     "Plate 1 temperature"
T[2]=350[K]                     "Plate 2 temperature"
T[3]=300[K]                     "Plate 3 temperature"

"Emissivities"
e[1]=0.4[-]                     "Emissivity of plate 1"
e[2]=0.6[-]                     "Emissivity of plate 2"
e[3]=0.9999[-]                  "Emissivity of surroundings"

"Areas"
A[1]=a*b                        "Area of plate 1"
A[2]=a*b                        "Area of plate 2"
A[3]=1e10 [m^2]                 "Area of surroundings, ~infinite"

"View Factors"
"Surface 1"
F[1,1]=0                        "Plate 1 cannot see itself"
F[1,2]=F3D_1(a,b,c)             "Function calling Eq. (3.21)"
F[1,3]=1-F[1,2]                 "Enclosure rule for surface 1"
"Surface 2"
F[2,1]=F3D_1(a,b,c)             "Function calling Eq. (3.21)"
F[2,2]=0                        "Plate 2 cannot see itself"
F[2,3]=1-F[2,1]                 "Enclosure rule for surface 2"
"Surface 3"
F[3,1]=A[1]*F[1,3]/A[3]         "Reciprocity between surface 1 and 3"
F[3,2]=A[2]*F[2,3]/A[3]         "Reciprocity between surface 2 and 3"
F[3,3]=1-F[3,1]-F[3,2]          "Enclosure rule for surroundings"
```

$$F = \begin{bmatrix} 0 & 0.1998 & 0.8002 \\ 0.1998 & 0 & 0.8002 \\ 8E-11 & 8E-11 & 1 \end{bmatrix}$$

Figure 3.8. View factors for each surface to surface interaction.

Now that the view factors are calculated, the net rate of radiation heat transfer can be calculated by the radiosity method using Eqs. (3.10) and (3.11) with the EES. Note that the emissivity for the surroundings is set to slightly less than 1 to avoid a division by zero in Eq. (3.10). The rate of heat transfer from the three surfaces can be seen in Figure 3.9.

```
"Boundary Conditions"
E_b[1]=sigma#*T[1]^4                          "Blackbody emissive power per unit area for surface 1"
E_b[2]=sigma#*T[2]^4                          "Blackbody emissive power per unit area for surface 2"
E_b[3]=sigma#*T[3]^4                          "Blackbody emissive power per unit area for surface 3"

"Radiosity Method"
duplicate i=1,3
    q_dot[i]=e[i]*A[i]*(E_b[i]-J[i])/(1-e[i])     "Net radiation exchange for all surfaces"
    q_dot[i]=A[i]*sum(F[i,j]*(J[i]-J[j]),j=1,3)   "Energy balance for each surface"
end
```

$$\dot{Q} = [2{,}719 \quad -102 \quad -2{,}617]$$

Figure 3.9. Net rate of heat transfer from each surface.

Using the F-hat method, the view factors from Figure 3.8 and the surface reflective values (ρ=1-ε) can be used in Eq. (3.17). Substituting the values into the Eq. can be seen below in Eq. (3.22). Inverting the matrix $[I - F\rho]$ may be the only difficult part in solving for the F-hat values, however many algorithms already exists for this type of operation which are computationally fast and accurate.

$$\hat{F} = \left(\begin{bmatrix} 1 & 0 & 0 \\ 0 & 1 & 0 \\ 1 & 0 & 1 \end{bmatrix} - \begin{bmatrix} 0 & 0.0799 & 8E-5 \\ 0.1199 & 0 & 8E-5 \\ 4.8E-11 & 3.2E-11 & 1E-4 \end{bmatrix} \right)^{-1} \cdot \begin{bmatrix} 0 & 0.1998 & 0.8002 \\ 0.1998 & 0 & 0.8002 \\ 8E-11 & 8E-11 & 1 \end{bmatrix} \quad (3.22)$$

$$\hat{F} = \begin{bmatrix} 1.0097 & 0.0807 & 8.7E-5 \\ 0.1210 & 1.0097 & 9E-5 \\ 5.23E-11 & 3.62E-11 & 1.0001 \end{bmatrix} \cdot \begin{bmatrix} 0 & 0.1998 & 0.8002 \\ 0.1998 & 0 & 0.8002 \\ 8E-11 & 8E-11 & 1 \end{bmatrix} \quad (3.23)$$

The F-hat values for this example can be seen in Figure 3.10. Comparing the F-hat values to the view factors from Figure 3.8, the F-hat values are larger because they now incorporate indirect radiation transfer; however, they still lie between 0-1. Eq. (3.18) which can be used to check if the values are correct. Using the F-hat method allows for each surface-to-surface radiation exchange to be determined (Figure 3.11), where the radiosity method only can provide the net transfer. Summing the radiation values from Figure 3.11 leads to the equivalent solution found by the radiosity method in Figure 3.9. The MATLAB code used for this is written below.

$$\hat{F} = \begin{bmatrix} 0.0161 & 0.2017 & 0.8726 \\ 0.2017 & 0.0242 & 0.9049 \\ 8.7E-11 & 9E-11 & 1 \end{bmatrix}$$

Figure 3.10. F-hat values for each surface to surface interaction.

$$\dot{Q} = \begin{bmatrix} 0 & 315 & 2{,}404 \\ -315 & 0 & 213 \\ -2{,}404 & -213 & 0 \end{bmatrix} = \begin{bmatrix} 2{,}719 \\ -102 \\ -2{,}617 \end{bmatrix}$$

Figure 3.11. Radiation exchange between surfaces with F-hat method.

```
%%%F-hat Sample Problem MATLAB Code%%%
clear all                          %Clear variables in workspace
clc                                %Clear command window
sigma=5.67E-8;                     %Stefan-Boltzmann constant. [W/m^2-K^4]
F=xlsread("ViewFactors.xlsx");     %Load view factor matrix (Figure 3.8) from excel spreadsheet.
epsilon=[0.4,0.6,1];               %Emissivity of each surface
A=[1,1,1e10];                      %Areas
T=[600,350,300];                   %Temperatures
rho=1-epsilon;                     %Calculates the reflectivity of each surface.
KD=eye(3);                         %Creates a 3 x 3 identity matrix
F_hat=inv(KD-F.*rho)*F             %Solves Eq. (3.17) for F-hat values
Check_F_hat=zeros(3,1);            %Initialize vector to use for Eq. (3.18)
for i=1:3
   for j=1:3
      %Check F-hat solves Eq. (3.18). All rows should equal 1.
      Check_F_hat(i)=Check_F_hat(i)+(1-rho(j))*F_hat(i,j);
      %Calculates the radiation exchange between each surface.
      Q(i,j)=epsilon(i)*A(i)*sigma*(epsilon(j)*F_hat(i,j)*(T(i)^4-T(j)^4));
   end
end
Q_net=sum(Q,2);                    %Sums columns to determine the net radiation exchange.
```

4. Energy Balance

An energy balance for each element in the cavity system can be written as shown by Eq (4.1), with the incoming energy on the left-hand side of the equation balanced against the solar loss, thermal loss, convection loss, and the energy transferred to the HTF on the right-hand side. The convective loss and energy transfer to the HTF for each node can be defined by Eqs. (4.2) and (4.3) respectively. It should be noted that $\dot{Q}_{HTF,out,i}$ is only a non-zero value for the active panel elements.

$$\dot{Q}_{in,i} = \dot{Q}_{solar,out,i} + \dot{Q}_{thermal,out,I} + \dot{Q}_{convection,out,i} + \dot{Q}_{HTF,out,i} \quad (4.1)$$

$$\dot{Q}_{convection,out,i} = \bar{h}A_i(T_i - T_\infty) \tag{4.2}$$

$$\dot{Q}_{HTF,out,i} = UA_i\left(T_i - T_{HTF,i}\right) \tag{4.3}$$

The incoming radiation that is calculated by SolTrace as described in Chapter 2 can be used to find the net solar radiation losses of the system with Eq. (3.19). The thermal loss, convection loss, and energy transfer to the HTF fluid are dependent on the panel's nodal temperatures which are unknown at this point. To solve for the panel nodal temperatures, the energy balance can be converted to matrix form (4.4), with the unknowns in x being the nodal temperatures.

$$Ax = b \tag{4.4}$$

However, because the temperature values in Eq (3.20) have an exponent to the 4th power while Eqs. (4.2) and (4.3) have an exponent of 1, the problem will require an iterative approach to solve. To have a starting guess point for the nodal temperatures, the convection loss (4.2) and HTF gain (4.3) can be set to zero which leads to Eq. (4.5). Since this form of the equation does not include convection loss or the gain to the HTF, the maximum nodal temperature of the system can be determined by this approach.

$$\dot{Q}_{in,i} = \dot{Q}_{solar,out,i} + \dot{Q}_{thermal,out,i} \tag{4.5}$$

This form of the problem only involves temperatures to the fourth power, and therefore can be solved directly using matrix inversion. The A matrix (4.6) of this formula is a N-1 x N-1 coefficient matrix and the x vector is a N-1 x 1 of unknown temperature values to the fourth power. The Nth column and row is not included because T_N is the ambient temperature and is defined by the user. The b vector (4.8) is a N-1 x 1 of known values, such as the incoming radiation, solar radiation loss, etc. Note that the epsilon values in Eqs. (4.6) and (4.8) and for the rest of chapter 4 are the thermal emissivities. After solving for the maximum nodal temperature values of the system, they can then be set as the first initial guess values when solving Eq. 4.1 iteratively.

$$A = \begin{bmatrix} -\varepsilon_1\hat{F}_{1,1} + \sum_{j=1}^{N}\varepsilon_j\hat{F}_{1,j} & -\varepsilon_2\hat{F}_{1,2} & \cdots & \cdots & -\varepsilon_{N-1}\hat{F}_{1,N-1} \\ -\varepsilon_1\hat{F}_{2,1} & \ddots & & & -\varepsilon_{N-1}\hat{F}_{2,N-1} \\ \vdots & & -\varepsilon_j\hat{F}_{i,j} + \sum_{j=1}^{N}\varepsilon_j\hat{F}_{i,j} & & \vdots \\ -\varepsilon_1\hat{F}_{N-2,1} & & & \ddots & -\varepsilon_{N-2}\hat{F}_{N-2,N-1} \\ -\varepsilon_1\hat{F}_{N-1,1} & -\varepsilon_2\hat{F}_{N-1,2} & \cdots & \cdots & -\varepsilon_{N-1}\hat{F}_{N-1,N-1} + \sum_{j=1}^{N}\varepsilon_j\hat{F}_{N-1,j} \end{bmatrix} \quad (4.6)$$

$$x = \begin{bmatrix} T_{1,max}^4 \\ T_{2,max}^4 \\ \vdots \\ T_{N-2,max}^4 \\ T_{N-1,max}^4 \end{bmatrix} \quad (4.7)$$

$$b = \begin{bmatrix} \frac{Q_{in,1} - Q_{solar,out,1}}{\varepsilon_1 A_1 \sigma} + \varepsilon_7\hat{F}_{1,7}(T_\infty^4) \\ \frac{Q_{in,2} - Q_{solar,out,2}}{\varepsilon_2 A_2 \sigma} + \varepsilon_7\hat{F}_{2,7}(T_\infty^4) \\ \vdots \\ \frac{Q_{in,N-2} - Q_{solar,out,N-2}}{\varepsilon_{N-2} A_{N-2} \sigma} + \varepsilon_7\hat{F}_{N-2,7}(T_\infty^4) \\ \frac{Q_{in,N-1} - Q_{solar,out,N-1}}{\varepsilon_{N-1} A_{N-1} \sigma} + \varepsilon_7\hat{F}_{N-1,7}(T_\infty^4) \end{bmatrix} \quad (4.8)$$

Before setting up the next set of matrices and vectors to solve Eqn (4.1), a few aspects of the code will be discussed. The HTF inlet and outlet temperatures are defined by the user with the flow path being routed from the bottom of the cavity panels to the top. These temperatures define the nodal temperature values of the HTF for each panel element ($T_{HTF,i}$), which are assumed to be a linear variation from inlet to outler. An initial mass flow rate ($\dot{m}$) is calculated with Eq. (4.9), with a guess value for the thermal efficiency of the system ($\eta_{thermal}$).

$$\dot{m}_{HTF} = \frac{\eta_{thermal} \cdot \dot{Q}_{in,panel}}{c_{HTF} \cdot (T_{HTF,out} - T_{HTF,in})} \quad (4.9)$$

The conductance (UA_i) in Eq. (4.3) can be determined by calculating the reciprocal of the total thermal resistance between the panel outer surface and the HTF (Eq. 4.10). It should be noted that

only half of the panel's tube banks are irradiated, and the non-irradiated side is assumed to be at the HTF temperature. The total thermal resistance consists of a radial conduction resistance between the tube's outer and inner surface (4.11) and a convection resistance from the inner tube's surface to the HTF (4.12). The circumferential conduction radiation is not accounted for as it was determined to be negligible (Teichel, 2011).

$$UA_i = \frac{1}{R_{conduction,i} + R_{convection,i}} \tag{4.10}$$

$$R_{conduction,i} = \frac{ln\left(\frac{D_{tube,outer}}{D_{tube,inner}}\right)}{\pi \cdot L_{tube,i} \cdot k_{tube} \cdot N_{tubes}} \tag{4.11}$$

$$R_{convection,i} = \frac{2}{h_{HTF,i} \cdot N_{tubes} \cdot L_{tube,i} \cdot D_{tube,inner} \cdot \pi} \tag{4.12}$$

The outer and inner diameter of the tubes are set to 40mm and 37.5mm respectively, which are the default values in SAM's molten power tower model. The length of the tube per element ($L_{tube,i}$) and the number of tubes (N_{tube}) is dependent on the routing of the HTF. In this model, the routing is assumed to be a vertical alignment. The heat transfer coefficient for the HTF (h_{HTF}) is calculated by laminar and turbulent flow correlations from (Nellis & Klein, 2009). Alternatively, the UA_i can be set directly by the user if desired.

For the convection portion of the problem, the average heat transfer coefficient for the entire cavity can be one of three choices: user-defined, (Siebers & Kraabel, 1984), or (Clausing, et al., 1987) described in chapter 1. Note that the correction factor from the Siebers and Kraabel correlation for inclination or added lips is not used. The correction factor stated by the author was based on the hypothesized effect that the inclination angle and cavity lips were thought to have on the system using convective and non-convective zones. The convective and non-convective zones effects may be influenced by the temperature gradients between the air and panel and needs to be investigated further.

Before writing Eqn. (4.1) in matrix form, the temperature portion of the thermal radiation heat transfer (Eq 3.20) will be factored into a linear form as shown by equation (4.13). The temperatures that are denoted with an asterisk are values that will be used in the A matrix and b vector and will be updated with each sequential iteration until a convergence criterion is satisfied.

$$T_i^4 - T_j^4 = \left(T_i^2 + T_j^2\right)^* \left(T_i + T_j\right)^* \left(T_i - T_j\right) \tag{4.13}$$

The A coefficient matrix is the same size as before, however now it includes the T^* values. The matrix can be built into two parts, with initial values being added as seen in Eqn. (4.14) and the second portion being added to the main diagonal of the matrix (4.15). The b vector is similar to before, however now it includes a convection and HTF component.

$$A = \begin{bmatrix} -\varepsilon_1 \hat{F}_{1,1}(T_1^2 + T_1^2)^*(T_1 + T_1)^* & \cdots \\ \vdots & -\varepsilon_j \hat{F}_{i,j}\left(T_i^2 + T_j^2\right)^*\left(T_i + T_j\right)^* \\ -\varepsilon_1 \hat{F}_{N-1,1}(T_{N-1}^2 + T_1^2)^*(T_{N-1} + T_1)^* & \cdots \end{bmatrix}$$

$$\begin{matrix} \cdots & -\varepsilon_{N-1} \hat{F}_{1,N-1}(T_1^2 + T_{N-1}^2)^*(T_1 + T_{N-1})^* \\ & \vdots \\ \cdots & -\varepsilon_{N-1} \hat{F}_{N-1,N-1}(T_{N-1}^2 + T_{N-1}^2)^*(T_{N-1} + T_{N-1})^* \end{matrix} \Bigg] \tag{4.14}$$

$$A_{i,i} = A_{i,i} + \frac{(U_i + h_i)}{\varepsilon_i \sigma} + \sum_{j=1}^{N} \varepsilon_j \hat{F}_{i,j}\left(T_i^2 + T_j^2\right)^*\left(T_i + T_j\right)^* \; for \; i = 1 \ldots N-1 \tag{4.15}$$

$$x = \begin{bmatrix} T_1 \\ \vdots \\ T_{N-1} \end{bmatrix} \tag{4.16}$$

$$b = \begin{bmatrix} \dfrac{Q_{in,1} - Q_{solar,out,1}}{\varepsilon_1 A_1 \sigma} + \dfrac{\bar{h}_i \cdot T_\infty + U_i \cdot T_{HTF,1}}{\varepsilon_1 \sigma} \\ \vdots \\ \dfrac{Q_{in,N-1} - Q_{solar,out,N-1}}{\varepsilon_{N-1} A_{N-1} \sigma} + \dfrac{\bar{h}_i \cdot T_\infty + U_i \cdot T_{HTF,N-1}}{\varepsilon_{N-1} \sigma} \end{bmatrix} \tag{4.17}$$

The convergence error is calculated with Eqn. (4.18) for all nodal temperatures, and the max value of the error is compared to a set tolerance value. Additionally, a new mass flow rate value is calculated with a new efficiency value in (4.9) and compared to the previous mass flow rate value. These checks are done to determine if another iteration must be performed or if the solution is converged. A general process flow diagram can be seen in Figure 4.1.

$$Error = \frac{|T - T^*|}{T} \; for \; i = 1 \ldots N \tag{4.18}$$

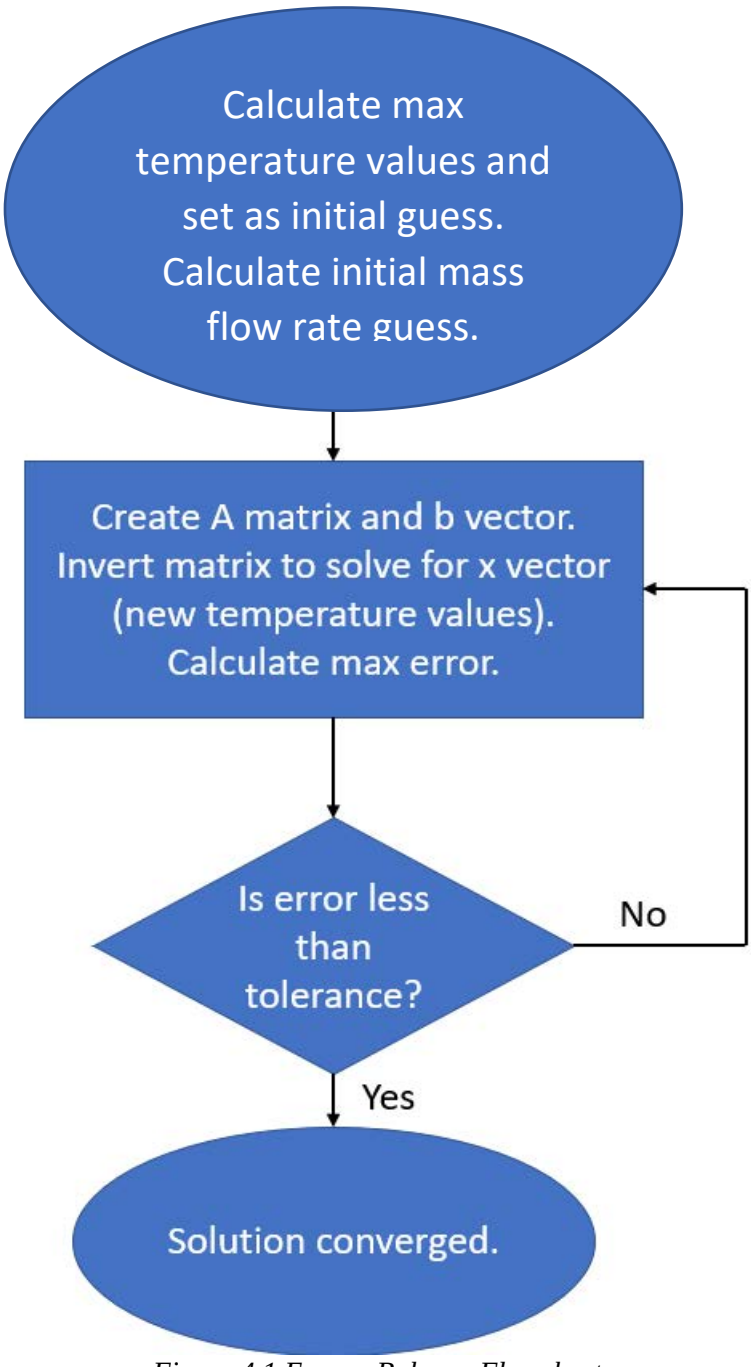

Figure 4.1 Energy Balance Flowchart.

Once the solution is converged, the nodal temperature can be used to determine the losses associated with the system as well as the HTF energy gain of the system. The solar radiation loss is pre-calculated using Eqn. (3.19) and the thermal radiation loss can be calculated by (3.20). These losses will be defined as the amount of radiation leaving the aperture. The convection loss and the HTF gain of the system can both be calculated using Eqs. (4.2) and (4.3) respectively.

4.1 Using Soltrace Flux Maps

To demonstrate that the code developed in this project is able to use data from external software such as SolarPILOT and Soltrace, a sample model was performed. The model was a 100 MW, 10 node system with a pyromark coating, with the same dimensions as the previous studies. The heliostat field and aim points were generated with SolarPILOT's priority aiming and imported in to SolTrace to solve for the incident flux maps. A percent distribution for each panel and node can be seen below in Table 2. The flux distribution was imported into the MATLAB code which was used to predict the efficiency. The efficiency of system was calculated to be 91.9%, with solar, thermal, and convection losses of 2.6%, 3.7%, and 1.8% respectively.

Nodes	Panel 1	Panel 2	Panel 3	Panel 4
1	5.14	5.55	5.55	5.14
2	8.81	9.23	9.23	8.81
3	11.52	11.95	11.95	11.52
4	12.06	12.49	12.49	12.06
5	11.50	11.89	11.89	11.50
6	11.50	11.84	11.84	11.50
7	12.04	12.40	12.40	12.04
8	11.48	11.89	11.89	11.48
9	8.79	9.21	9.21	8.79
10	5.16	5.56	5.56	5.16

Table 4. SolTrace Flux Map Distribution for 100 MW system.

5. Cavity Studies

Now that the thermal performance of the cavity receiver can be predicted, a series of studies is undertaken to investigate the effects of the material coating (radiative properties) and added lips (convective loss enhancements). In addition, a comparison between an external receiver and cavity is conducted to determine the difference in the performance between the two types of receivers. The first two studies for the surface coating and lip effects is performed using a cavity with a receiver panel height of 12 m and a receiver panel width of 14 m. The incoming solar power is set as 100 MW; therefore each panel will receive 25 MW at an average flux of 389 kW/m^2. The panels are meshed using 10 nodes, and a single node is assumed for the roof and floor surfaces. The Siebers & Kraable convection correlation is used which neglects effects of wind. The same view

factor matrix will be used for all simulations in order to avoid any small inconsistencies caused by repeating the Monte-Carlo simulations. The HTF inlet and outlet temperatures are set to 563 K and 848 K, respectively.

5.1 Surface Coating

For this study, three different materials will be investigated: oxidized Inconel, Pyromark paint, and a multi-layer Ti-Si coating developed by Sandia (Ambrosini, A., et al. 2013). The Ti-Si coating has the best performance out of the three materials due to its high solar absorptivity and low thermal emissivity. The efficiency of the panel using the Ti-Si is 93.1%, compared to 92.2% and 89% of Pyromark and Inconel, respectively. Figure 5.1 shows a spider plot that includes the key parameters and resulting loss outputs for the three different absorber surface types. Table with the data in the subsequent figures can be found in Appendix B.

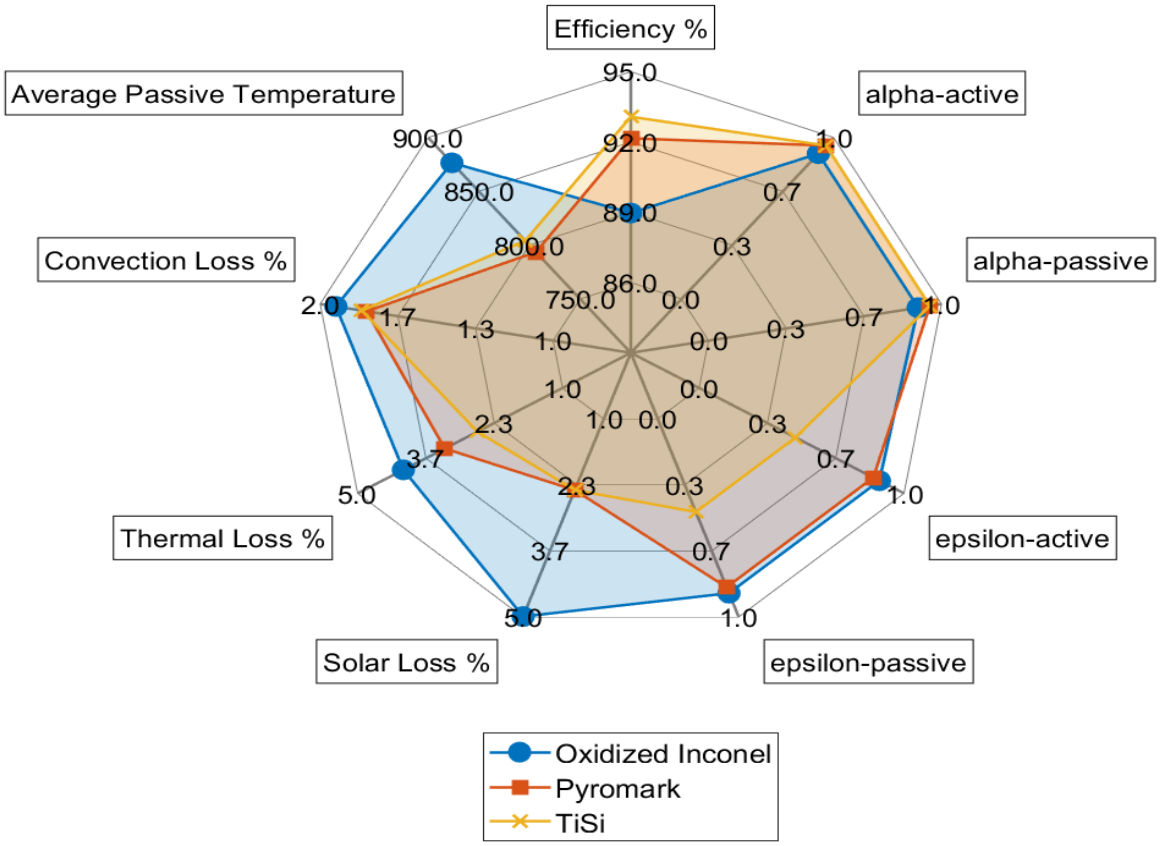

Figure 5.1 Coating Comparison. Active and Passive surface have the same α and ε values.

An additional case was run with a highly reflective material (α=ε=0.05) used for the passive surfaces (in this case, just the floor and ceiling) to determine what effects it might have on the overall efficiency of the cavity receiver. The reflective passive surfaces lead to an increased efficiency for all three receiver panel material options as shown by the spider plot in Figure 5.2 with the Pyromark cavity experiencing the largest efficiency increase by 1.4%. This increase is mainly due to the reflective material being able to prevent more of the thermal radiation from

escaping the cavity through the aperture opening and reflecting it back to the active receiver panel surfaces. Each of the cases showed a vast improvement in the passive surfaces being much cooler than the previous case.

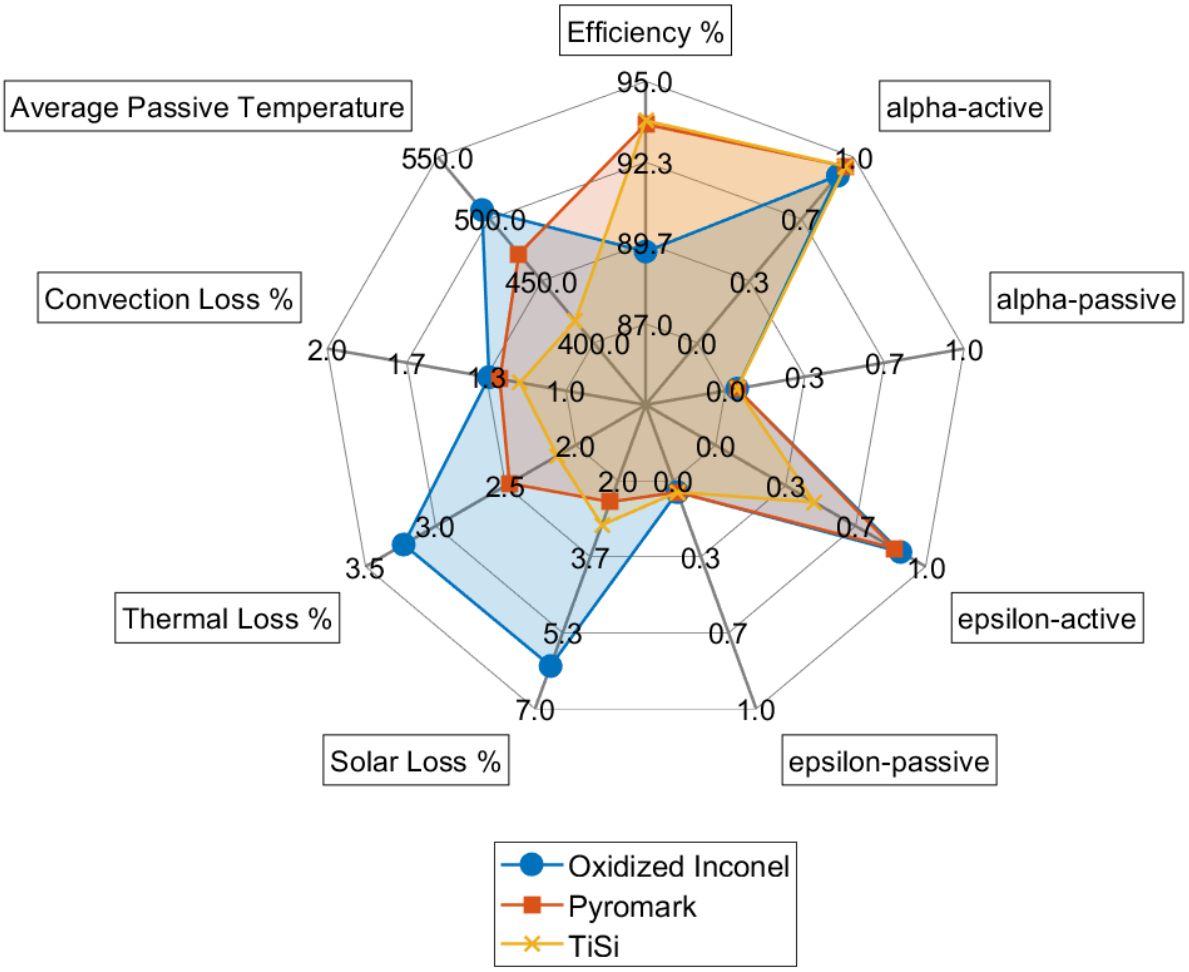

Figure 5.2 Coating Comparison. Passive surface are set as highly reflective material.

5.2 Lip Effects

The second set of studies will determine the effects that a passive upper and bottom lip will have on the cavity system. For both cases, 2 m upper and lower lips are added to the cavity as additional passive surfaces. The same two cases with the three different coatings aererun, with the first again assuming that the active and passive surfaces have the same coating (Figure 5.3), and the second case switching the passive surface to a reflective material (Figure 5.4).

Similar to the trend seen in the cavity without a lip, the addition of a lip at the cavity aperture improves the efficiency of all of the coatings, with the greatest improvement for the oxidized Inconel. This improved efficiency is the result of lower solar and thermal losses, even though the

convection losses are predicted to increase due to the additional passive surface area (note that the reduction in the average heat transfer coefficient that might accompany the use of a lip is not accounted for here).

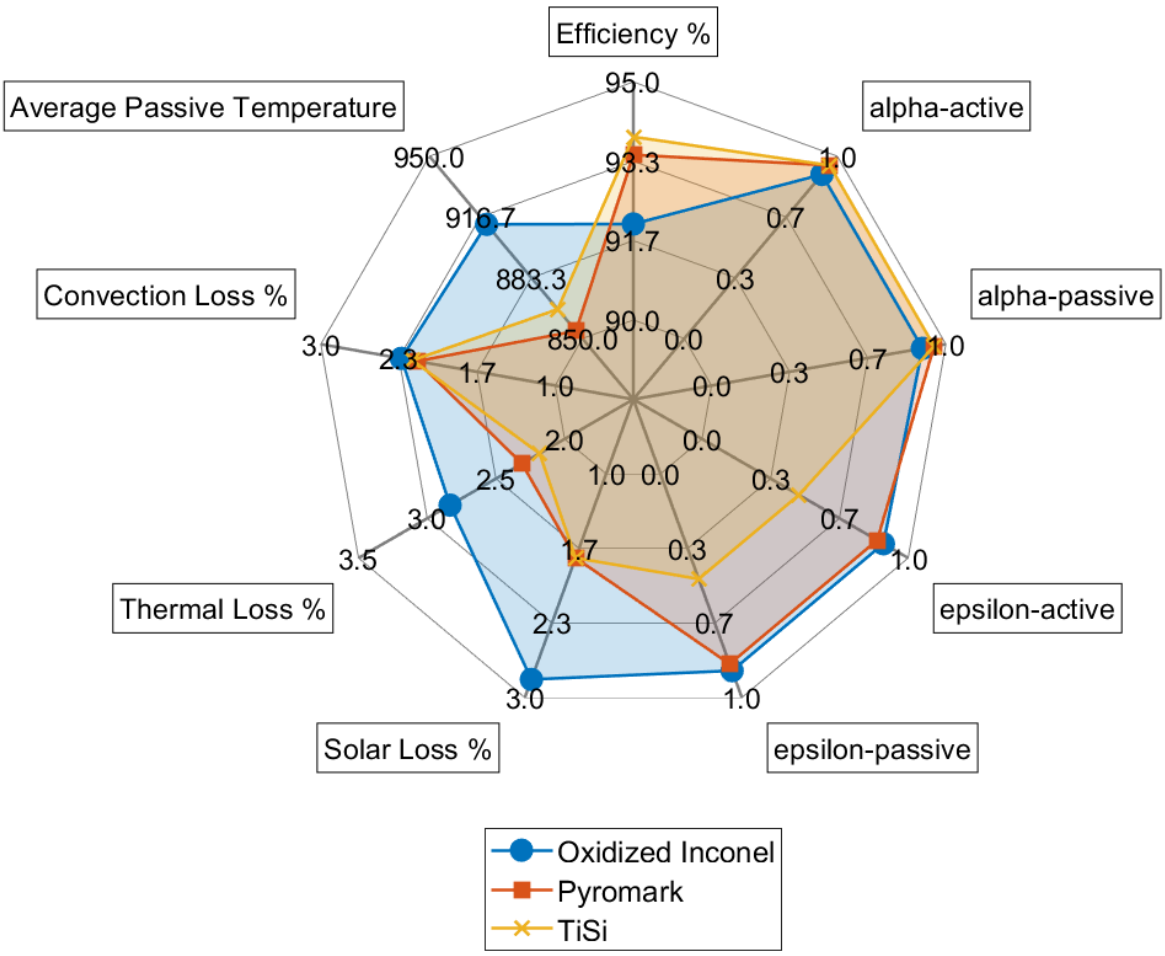

Figure 8.3 Added 2(m) top and bottom lips. Active and Passive surface have the same α and ε values.

Changing the passive material to be highly reflective has a similar effect to what was noted in the previous study, with one difference. The Pyromark and Ti-Si coating both showed an additional small gain in efficiency, about 1%, by changing the passive surface material. However, the oxidized Inconel performed slightly worse with the coating change. This is because a larger portion of solar energy is escaping the aperture due to the lower absorptivity of the coating. Additionally, increasing the lip size does theoretically improve the efficiency of all the coating options since it allows less radiation to escape. However, the increase in lip size does impact the flux distribution on the panels as heliostats are not be able to aim uniformly on the entire panel as their view will be obscured by the lip.

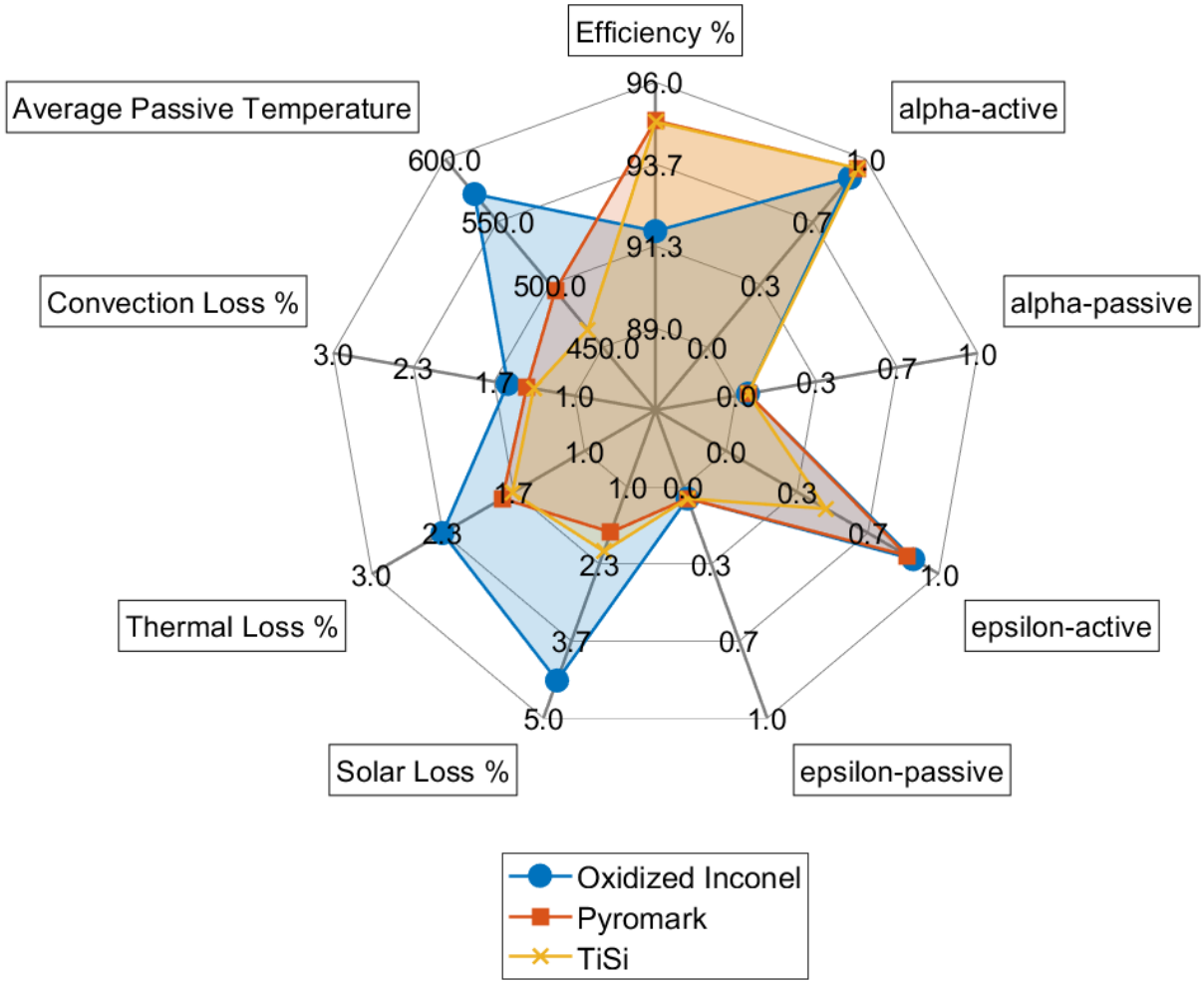

Figure 5.4 Added 2(m) top and bottom lips. Passive surface are set as highly reflective material.

5.3 External vs Cavity

One of the main objectives of this project was to be able to model cavity receivers and compare their performance to existing cylindrical receivers. To make this comparison an 8 panel "cylindrical" receiver was modeled using the same methodology that was used for the cavity receiver. Since the panels on the cylindrical receiver only exchange radiation with the environment and not between themselves, the radiation exchange is greatly simplified. The incoming power/heat flux was kept the same for both models and they were assumed to have identical active surface area. The receiver height was kept at 12 m with the same parameters for power, 100 MW.

To determine the differences in radiative performance between the two models, the first simulation was performed with the convection coefficient set to zero. For all three surface coatings, the cavity

outperforms the cylindrical receiver since the active surfaces are shielded from the ambient environment as shown in Figure 5.5. When comparing the efficiencies of both systems, the largest difference is seen with Inconel with a difference of 5.7%. This difference diminishes with the best performing coating of Ti-Si with a difference of 2.3%. The cavity is superior in minimizing both solar and thermal radiation losses.

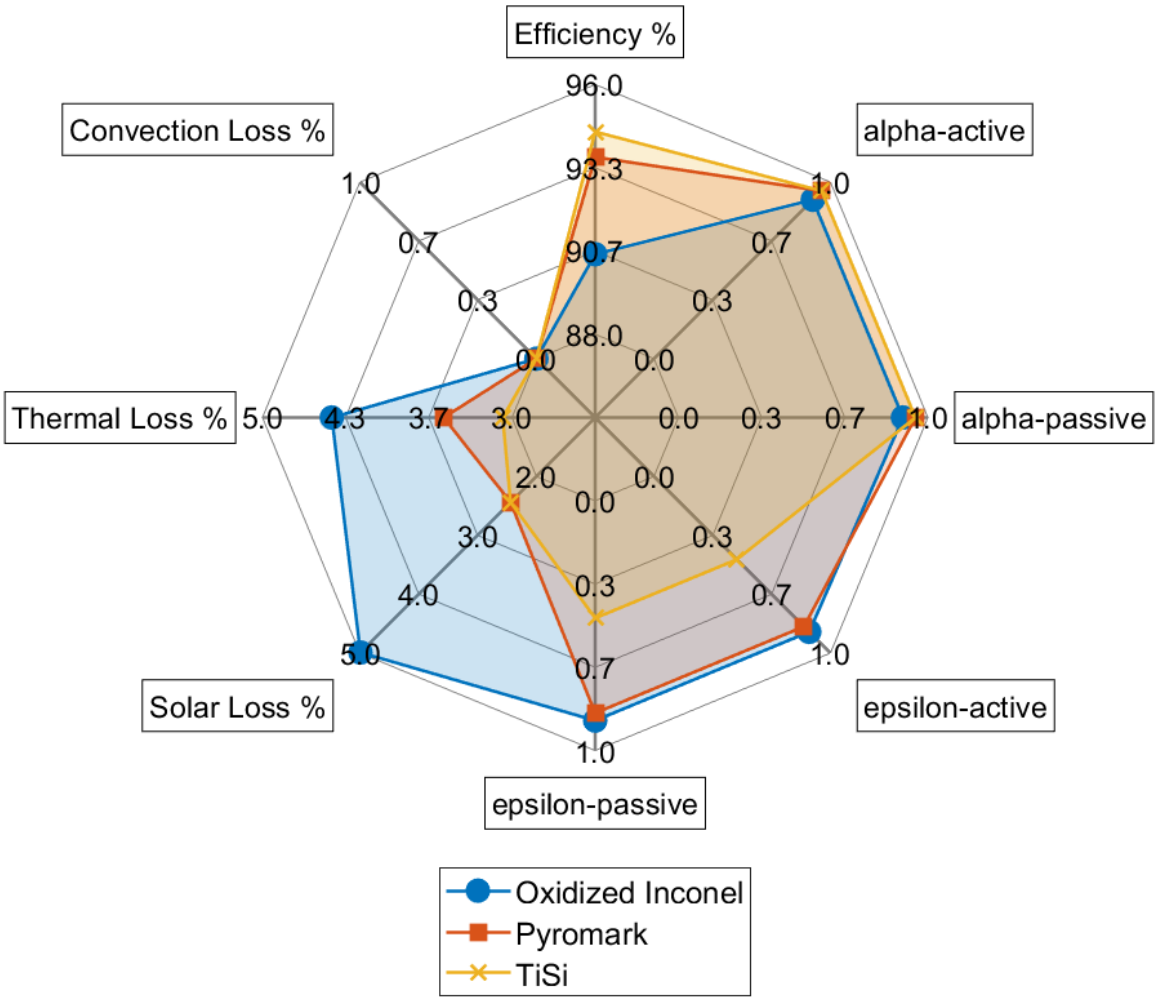

Figure 5.5 Cavity receiver with convection turned off. Active and passive surfaces are the same coating.

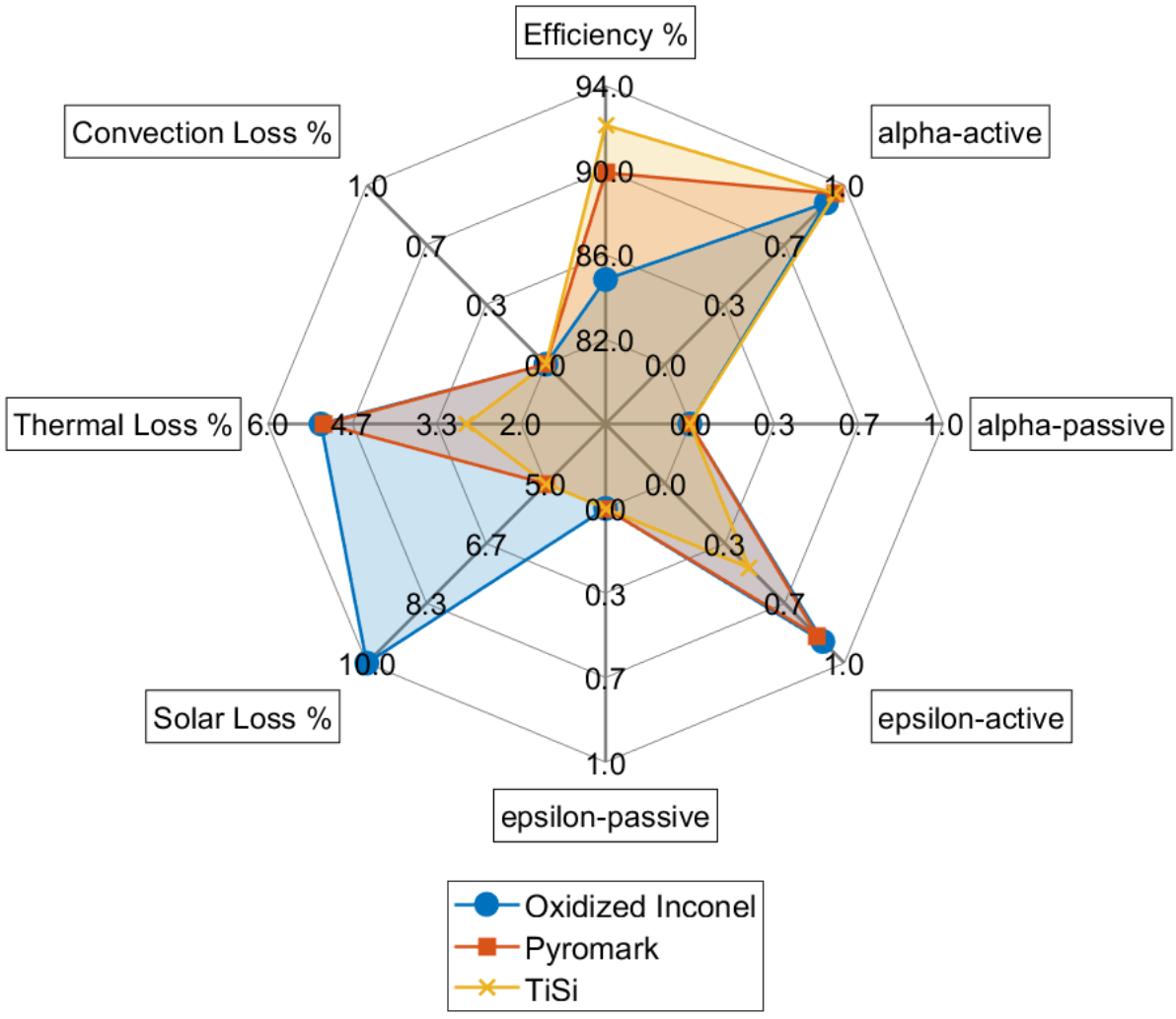

Figure 5.6 External receiver with convection turned off.

The next case uses the same convection heat transfer coefficient that is calculated for the cavity receiver for the external receiver case as well. The cavity still outperforms the external receiver in regards to radiation losses; however because the cavity has a significant passive surface area, the convection loss are higher as shown in Figure 5.7. The difference in the efficiency are still similar to that of the no convection case.

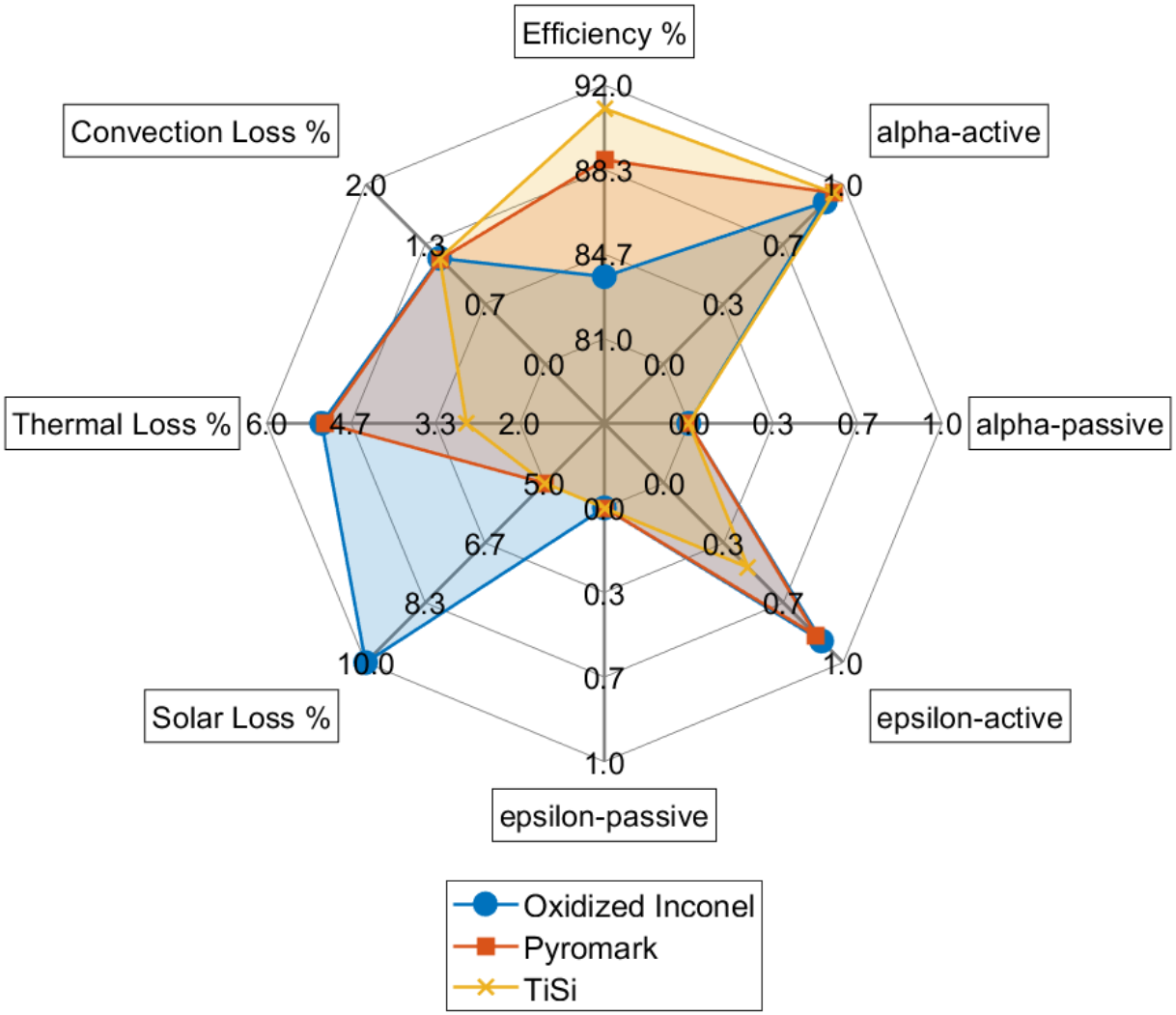

Figure 5.7 External receiver with convection value of cavity receiver.

The efficiency of both designs were plotted as a function of the heat transfer coefficient for 0 - 50 (W/m^2K) as seen in Figure 5.8. The trends show that the cavity receiver is more efficient than its counterpart when using the same coatings, but that the difference in efficiency between the two decreases when using selective surface coatings. It should be noted between the Inconel-Cavity and Pyromark-Cylindrical, when the heat transfer coefficient is above 15(W/m^2-K), the cylindrical will outperform the cavity.

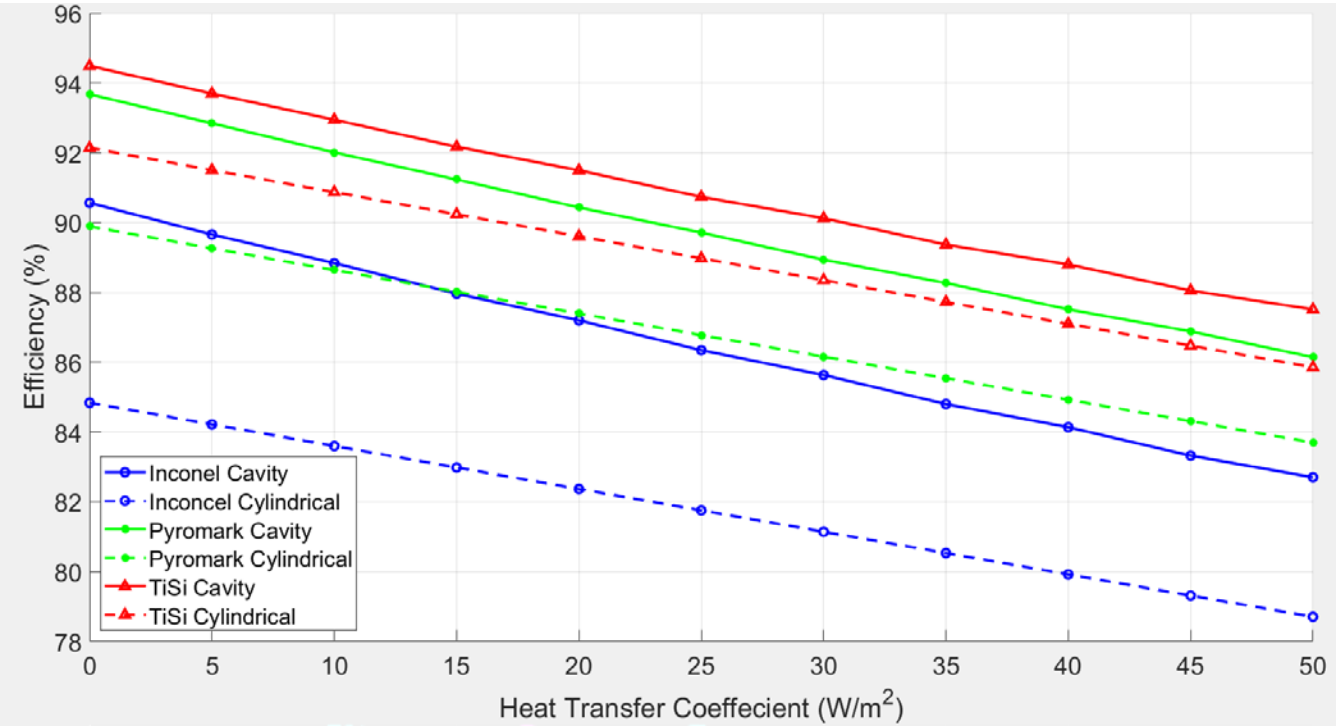

Figure 5.8 Heat transfer coefficient vs Efficiency for Cavity and External Receivers.

6. Conclusion and Future Work

Code development for the modeling of a cavity receiver was done with modification/scripting of NREL's current software SolarPILOT and SolTrace as well as newly created code in MATLAB, "*Octagonal Cavity Thermal Model*". SolarPILOT was used to generate a heliostat field and aim-points for a half-octagon cavity receiver. That heliostat data can then be imported in SolTrace and run to determine the solar flux on each of the cavity's surfaces. That data can be imported into the MATLAB code and used to determine the efficiency of the system as well as the losses from radiation and convection.

It was shown that the cavity receiver has a better overall thermal performance compared to an external cylindrical receiver system with the same active area and incident power. The receiver surface coating was shown to play a major role on each system's efficiencies. The selective coatings such as the Ti-Si multi-layer material developed by Sandia results in smaller differences in efficiency between the two designs. It should be noted that the cavity being shielded from additional environment factors such as the wind may lead to larger differences in performance.

It was also shown that adding lips to the cavity system can lead to an increase in the system's performance and that adding a reflective coating to the passive surfaces was generally better. Two aspects that were not considered in this model was the effects the receiver's geometry has on the heliostat field, as a cavity receiver will be limited to a north-facing field (in northern hemisphere) with a limited acceptance angle. This limited field and the decrease in the aperture size caused by adding lips may reduce the amount of energy that can be delivered to a cavity system. This suggests there is an optimum aperture area.

There is still a great deal that can be done in this subject area moving forward from this point. The largest source of uncertainty within the model is the convection losses. Experimental data for large-scale cavity receivers is still needed to validate current correlations or establish new ones. Collecting data from a plant that is currently in use may be possible with imaging technique such as shadowgraph, Schlieren, or DIC/PIV. In addition to collecting experimental data on full-scale receivers, CFD may offer some insights that can be used to better understand the convective heat loss and compare to the existing model.

Improving the coupling of the HTF to the model and modifying the code so that routing of the fluid can be studied for a better understanding of the impact it has on the receiver system. Also determining if the passive surfaces may possibly be used to preheat the HTF before circulating it through the active surface may be beneficial depending on the passive surface temperature. Modification can be done to the Monte-Carlo ray tracing algorithm that was developed so that higher quality meshes, and geometric changes can easily be done without a great deal of computational time being used. The code could also be modified to generate other geometries beside the half octagon cavity. The half octagon cavity was used because of its simplicity; However, the geometry is not optimized to prevent radiation or convection losses.

References

Ambrosini, A., Ghanbari, C., Kennedy, C., Lambert, T., Hall, A., Gray, M., & Ho C. (2013). High-Temperature Solar Selective Coating Development for Power Tower Receivers. Sandia National Laboratories.

Beckman, W. (1971). Solution of heat transfer problems on a digital computer. *Solar Energy*, *13*(3), 293–300.

Buie, D., Monger, A., & Dey, C. (2003). Sunshape distributions for terrestrial solar simulations. *Solar Energy*, *74*(2), 113–122.

Clausing, A. M. (1983). Natural Convection Correlations for Vertical Surfaces Including Influences of Variable Properties. *Journal of Heat Transfer*, *105*(1), 138–143.

Clausing, A. M., Waldvogel, J. M., & Lister, L. D. (1987). Natural Convection from Isothermal Cubical Cavities With a Variety of Side-Facing Apertures. *Journal of Heat Transfer*, *109*(2), 407–412.

Ding, W., Bonk, A., & Bauer, T. (2019). *Molten chloride salts for next generation CSP plants: Selection of promising chloride salts & study on corrosion of alloys in molten chloride salts.* 24th SolarPACES Conference: International Conference on Concentrating Solar Power and Chemical Energy Systems, Casablanca, Morocco.

Gallego. B. (2016, September 29). *How to achieve US$63MWh in a Concentrated Solar Power tower project with storage.* HELISCSP. http://helioscsp.com/how-to-achieve-us63mwh-in-a-concentrated-solar-power-tower-project-with-storage/

Gross, U., Spindler, K., and Hahne, E. (1981). Shape factor equations for radiation heat transfer between plane rectangular surfaces of arbitrary position and size with rectangular boundaries. *Heat Mass Transfer, 8*, 219-227.

Ho C., & Iverson B. (2012). *Reveiw of Central Receiver Designs for High-Temperature Power Cycles.* 18th SolarPACES Conference, Marrakech, Morocco.

Ho, C. K., & Iverson, B. D. (2014). Review of high-temperature central receiver designs for concentrating solar power. *Renewable and Sustainable Energy Reviews*, *29*, 835–846.

Howell, J. R. (1982). *A catalog of radiation configuration factors*. New York: McGraw-Hill Book.

IRENA (2019), Renewable Power Generation Costs in 2018, International Renewable Energy Agency, Abu Dhabi.

Jilte, R. D., Kedare, S. B., & Nayak, J. K. (2013). Natural Convection and Radiation Heat Loss from Open Cavities of Different Shapes and Sizes Used with Dish Concentrator. *Mechanical Engineering Research*, *3*(1), 25.

Kistler, B. (1986). A User's Manual for DELSOL3: A Computer Code for Calulating the Optical Performance and Optical System Design for Solar Thermal Central Recevier Plants. Sandia National Laboratories. SAND86-8018.

Leibfried, U., & Ortjohann, J. (1995). Convective Heat Loss from Upward and Downward-Facing Cavity Solar Receivers: Measurements and Calculations. *Journal of Solar Energy Engineering*, *117*(2), 75–84.

Lillian, B. (2016, May 25). *NRG Confirms Cause of Fire at Ivanpah Solar Plant.* Solar Industry. https://solarindustrymag.com/update-nrg-confirms-cause-of-fire-at-ivanpah-solar-plant

Nellis, G., & Klein, S. A. (2012). *Heat transfer*. Cambridge: Cambridge University Press.

Ngo, L., Bello-Ochende, T., & Meyer, J. (2015). Numerical modelling and optimisation of natural convection heat loss suppression in a solar cavity receiver with plate fins. *Renewable Energy*, *74*, 95–105.

Osunaa, R., Olavarríaa, R., Morilloa, R., Sáncheza, M., Canteroa, F., Fernández-Queroa, V., … & Silva, M. (2006). *PS10, Construction of a 11mw Solar Thermal Tower Plant In Seville, Spain*. 13th SolarPACES Conference, Seville, Spain.

Paitoonsurikarn, S. & Lovegrove K., (2006). A New Correlation for Predicting the Free Convection Loss from Solar Dish Concentrating Receivers.

Samanes, J., & Garcia-Barberena, J. (2014). A model for the transient performance simulation of solar cavity receivers. *Solar Energy, 110,* 789–806.

Sengupta, M., Xie, Y., Lopez, A., Habte, A., Maclaurin, G., & Shelby, J. (2018). The National Solar Radiation Data Base (NSRDB). *Renewable and Sustainable Energy Reviews, 89,* 51-60.

Siebers, D., & Kraabel, J. (1984). Estimating convective energy losses from solar central receivers. Sandia National Laboratories. SAND84-8717.

Teichel, S. H. (2011). Modeling and Calculation of Heat Transfer Relationships for Concentrated Solar Power Receivers. University of Wisconsin – Madison, Solar Energy Laboratory.

Wendelin, T., Dobos, A., & Lewandowski A. (2013). SolTrace: A Ray-Tracing Code for Complex Solar Optical Systems. National Renewable Energy Laboratory. TP-5500-59163.

Appendix A: Flux Maps from *ST*, *DELSOL3*, & *Tonatiuh* Comparison.

DELSOL3 (Top) vs. SolTrace (Bottom) Solar Flux Maps:

Case 1: Azimuth 69.8° Zenith 13.5°

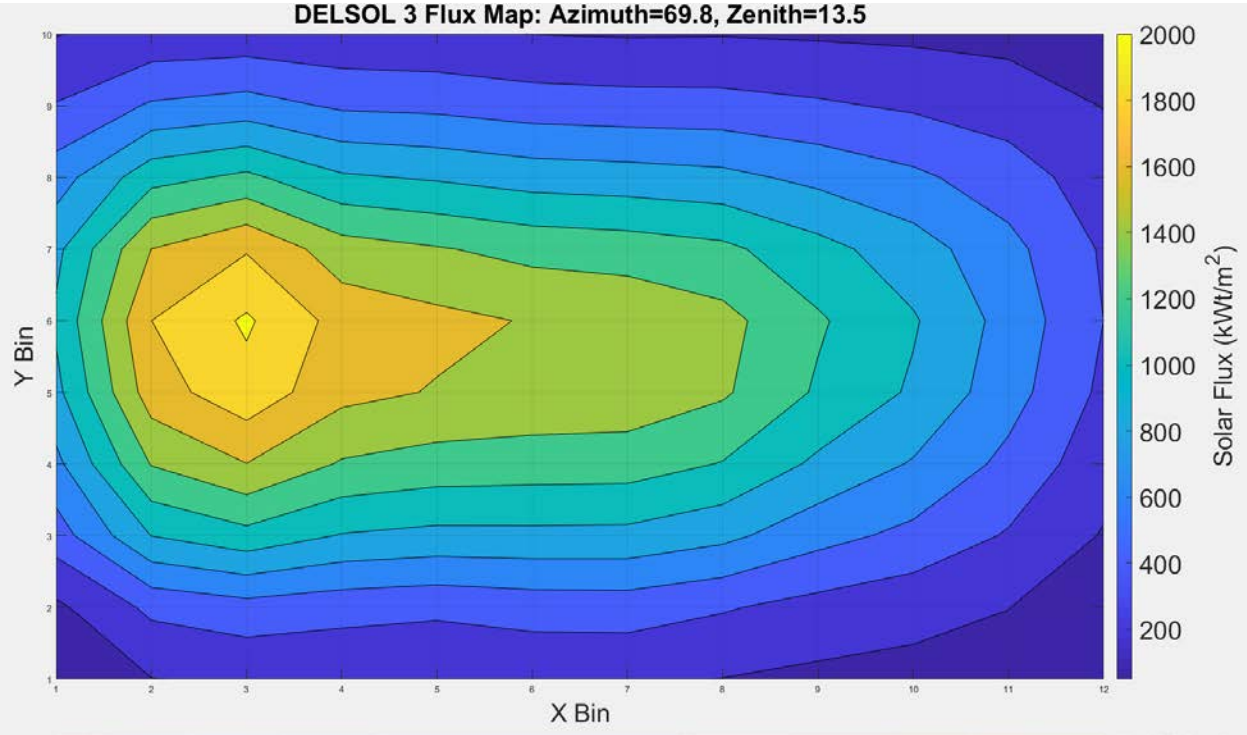

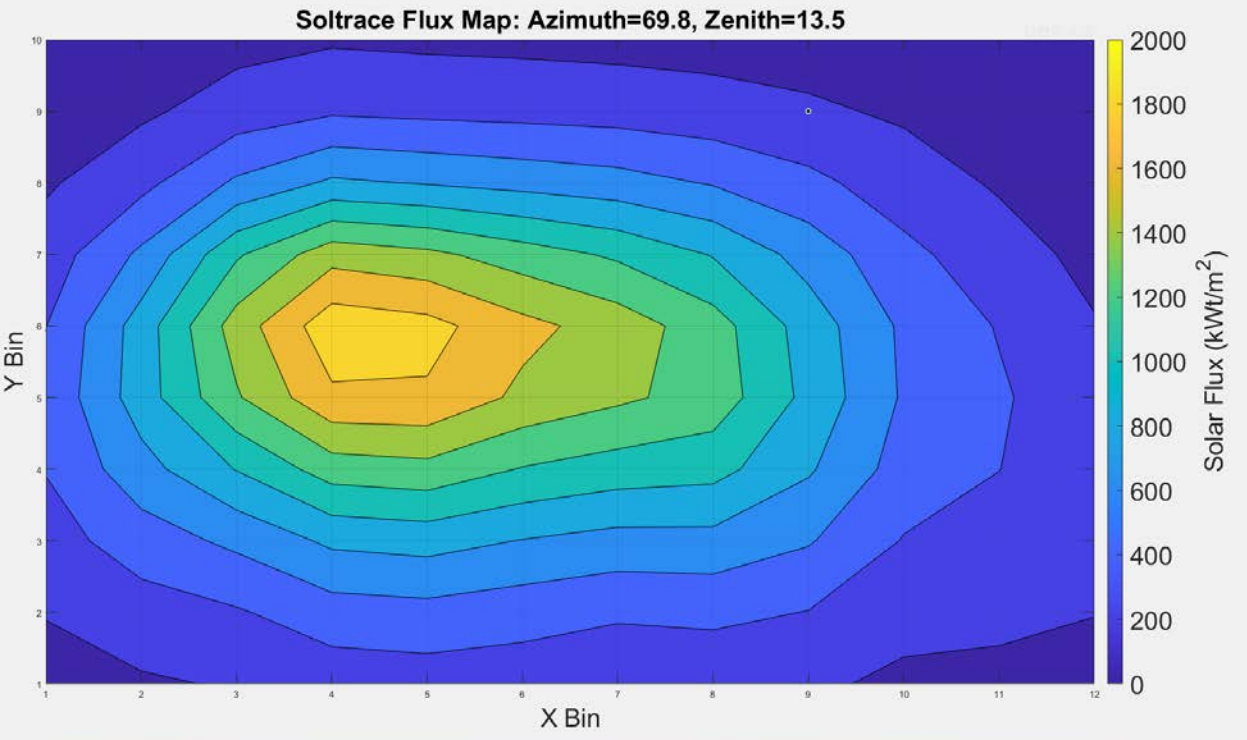

Case 3: Azimuth 84.6° Zenith 37.5°

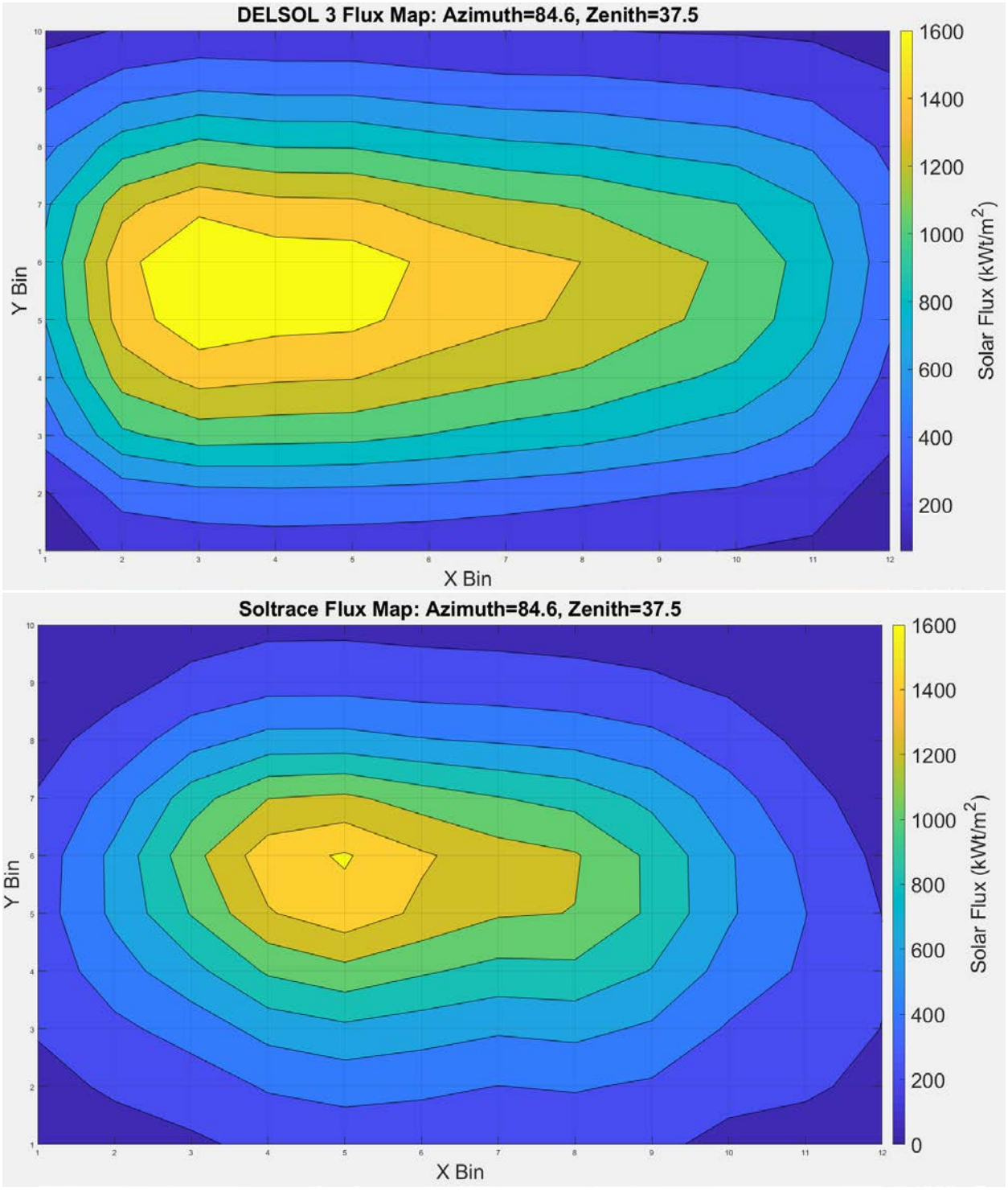

Case 5: Azimuth 104.3° Zenith 61.9°

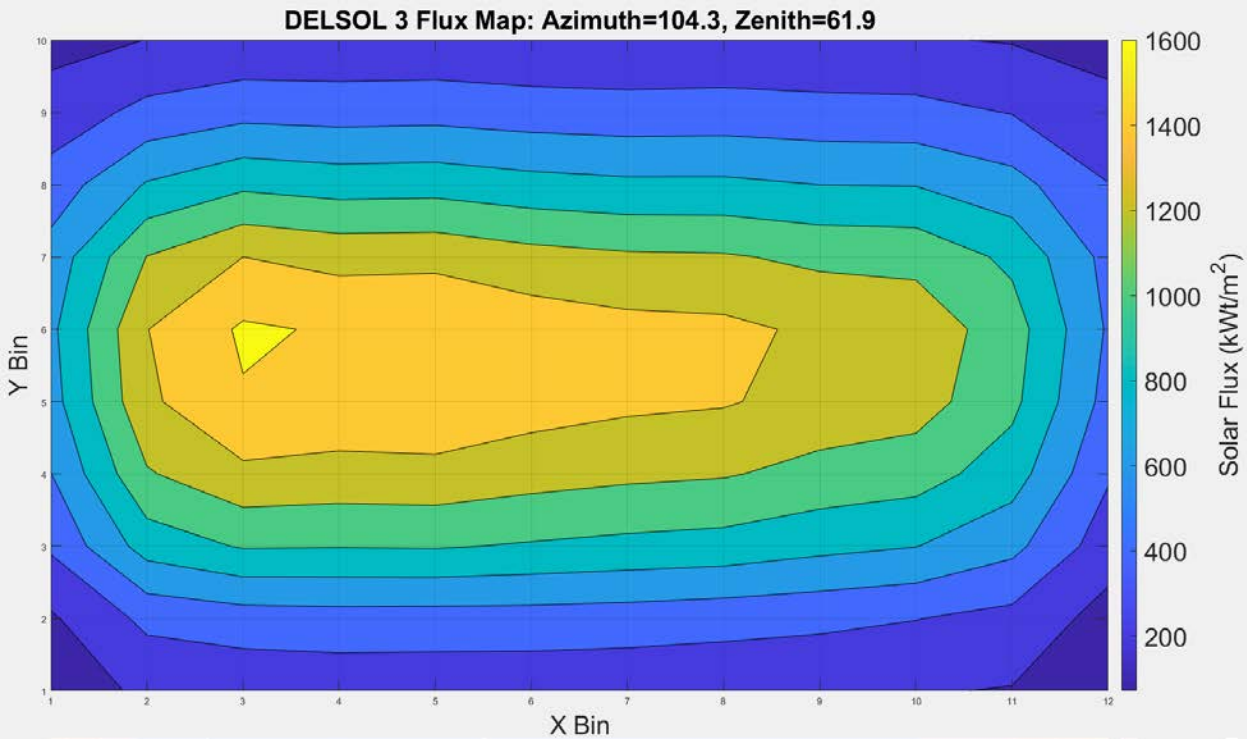

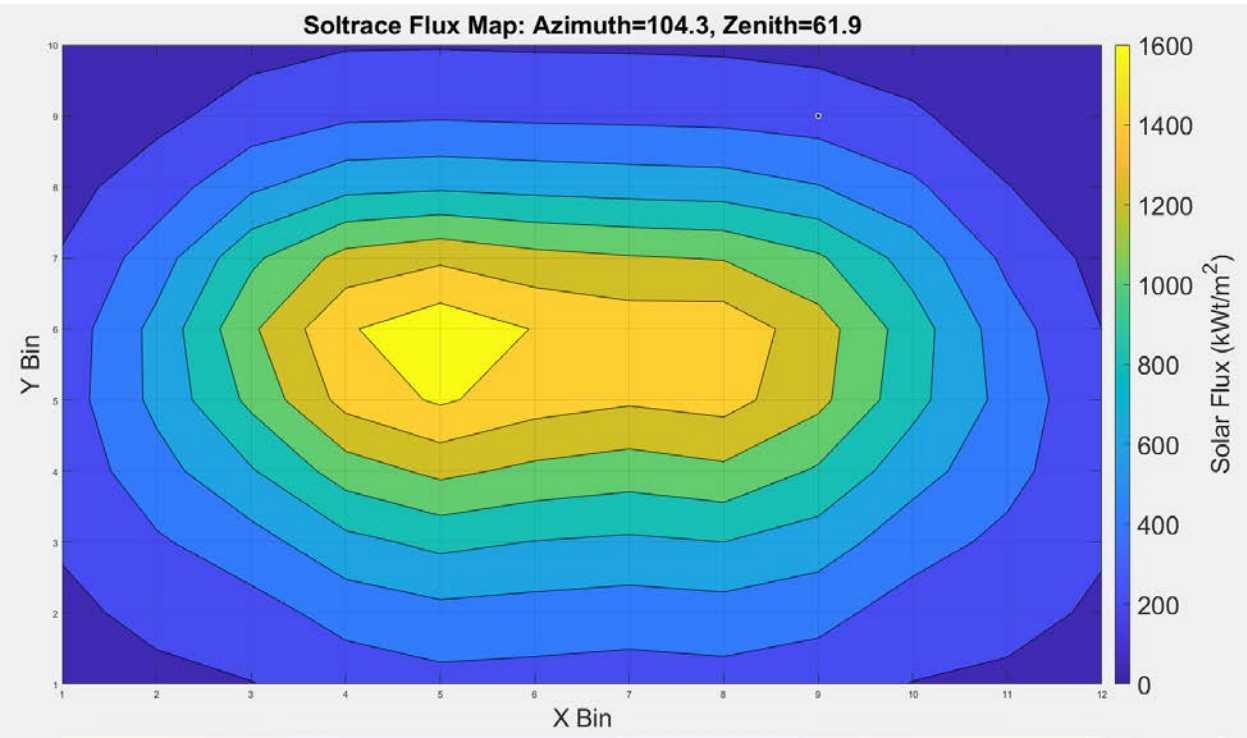

Case 7: Azimuth 180° Zenith 79.3°

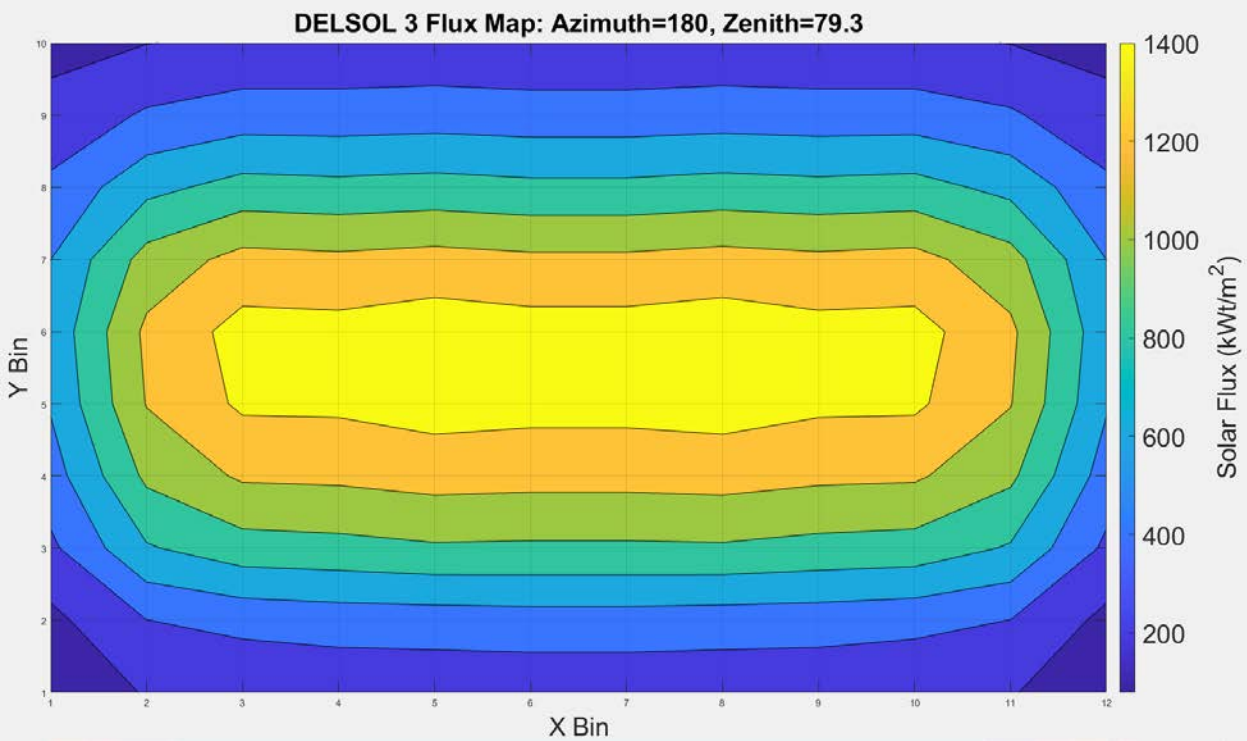

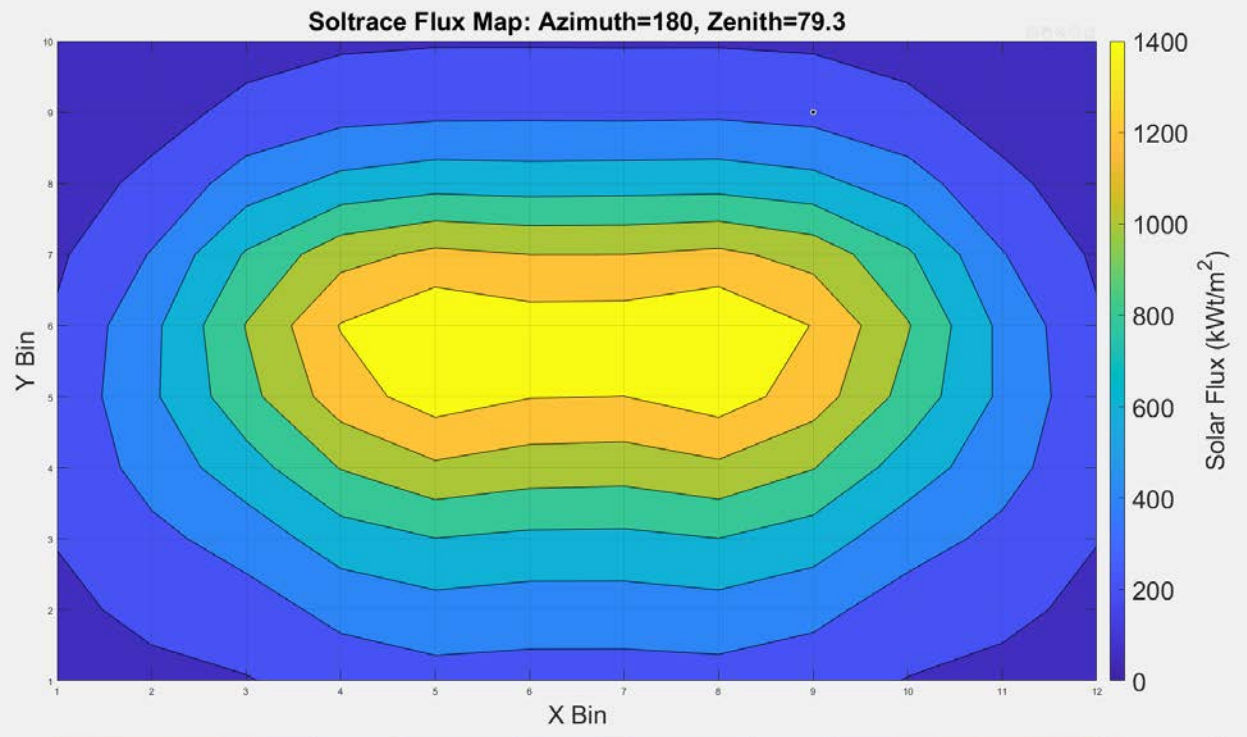

Tonatiuh (Top) vs. SolTrace (Bottom) Solar Flux Maps:

Case 1: Azimuth 69.8° Zenith 13.5°

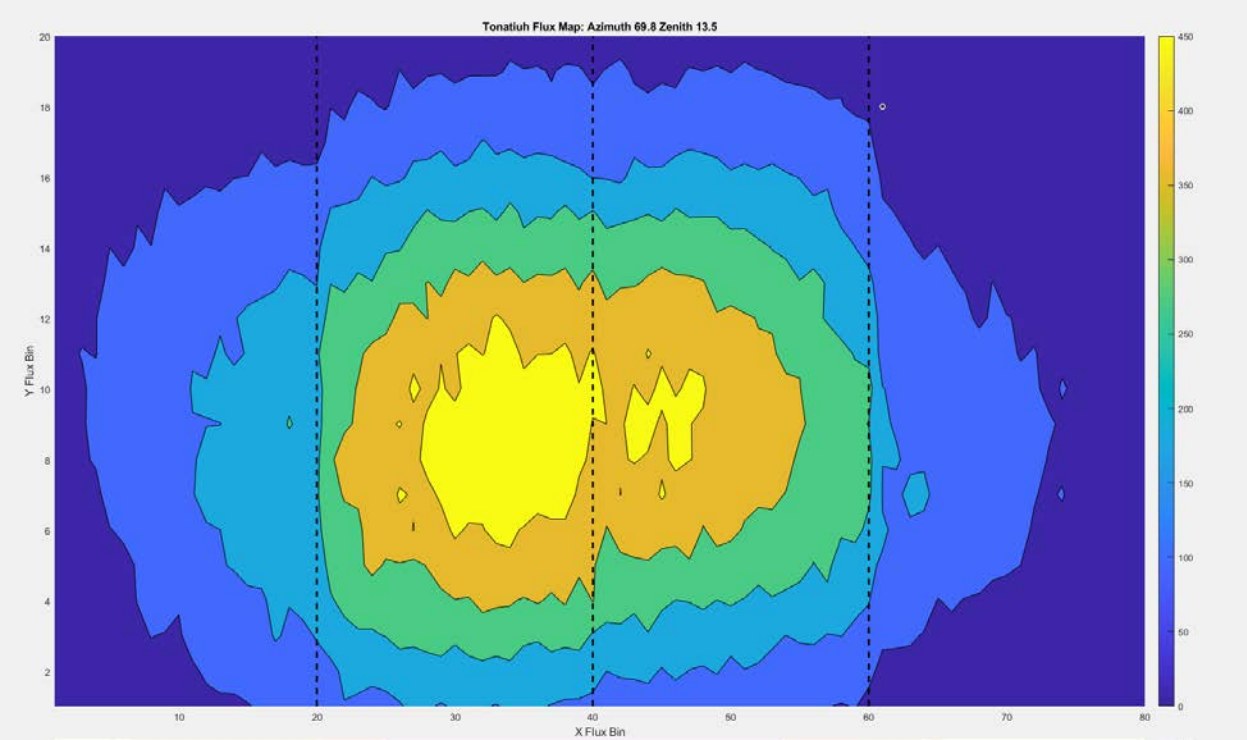

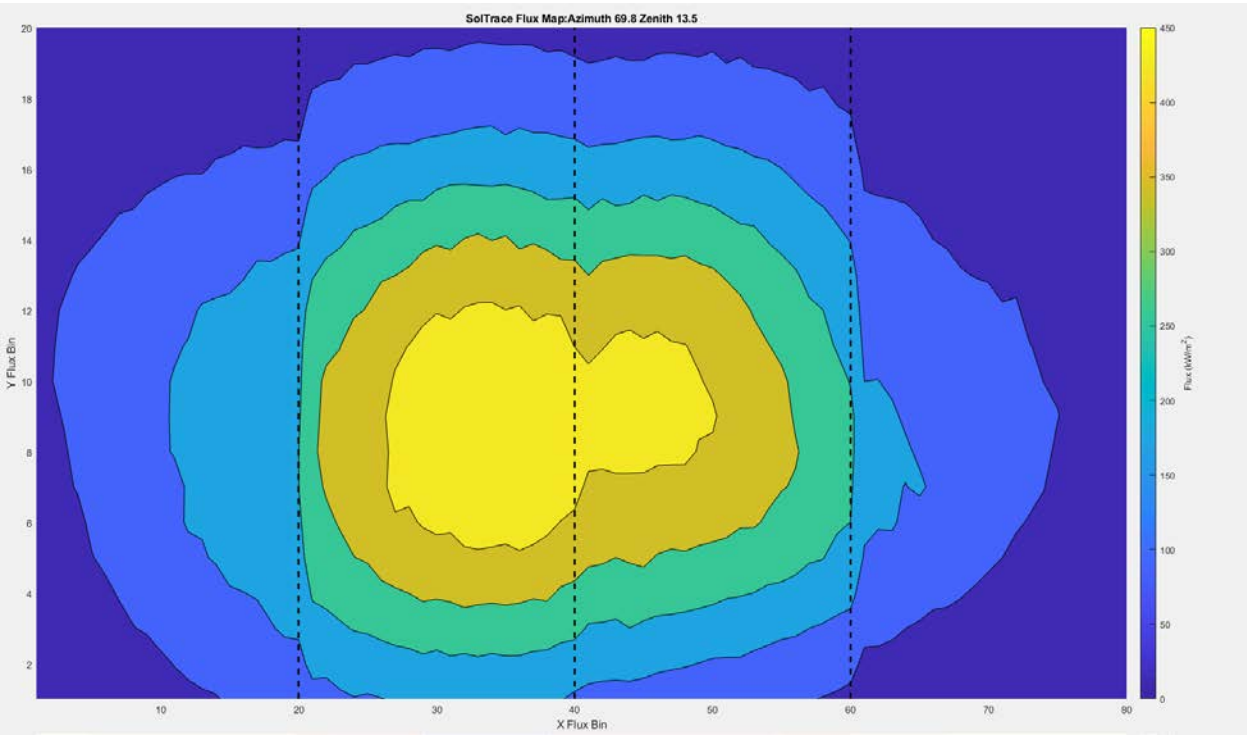

Case 3: Azimuth 84.6° Zenith 37.5°

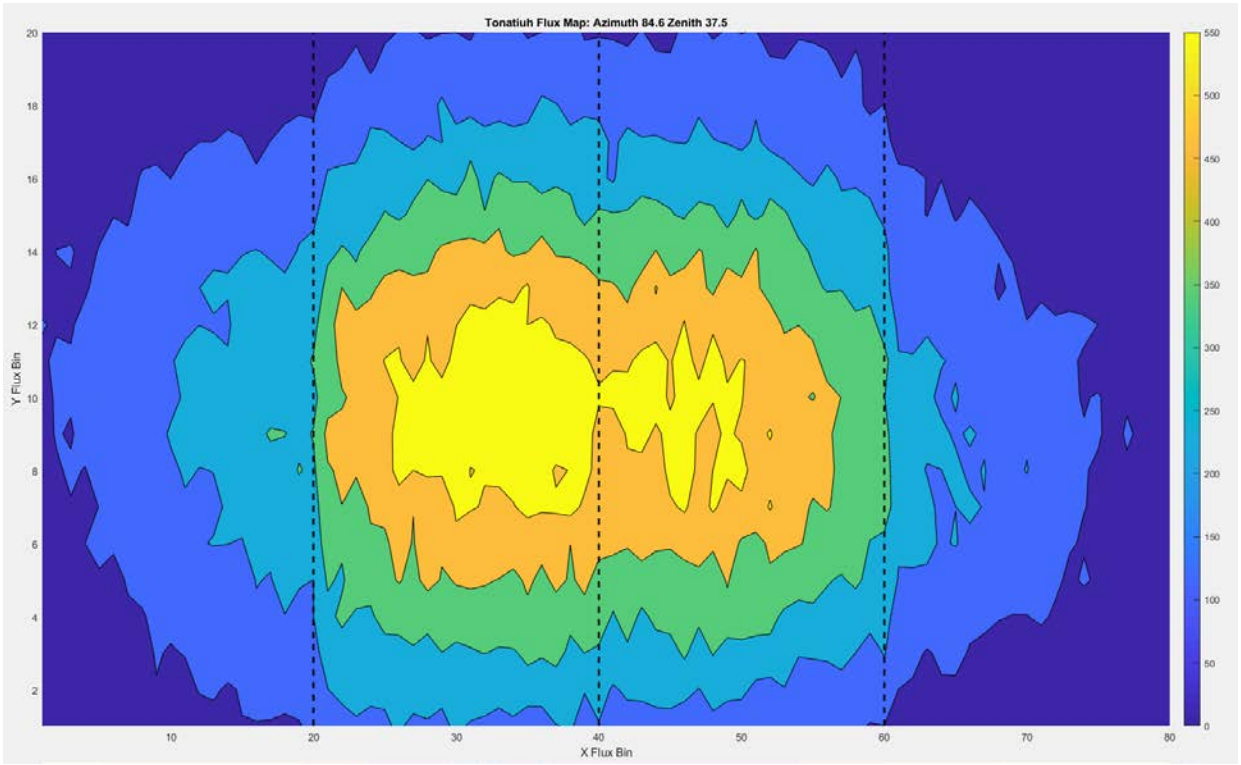

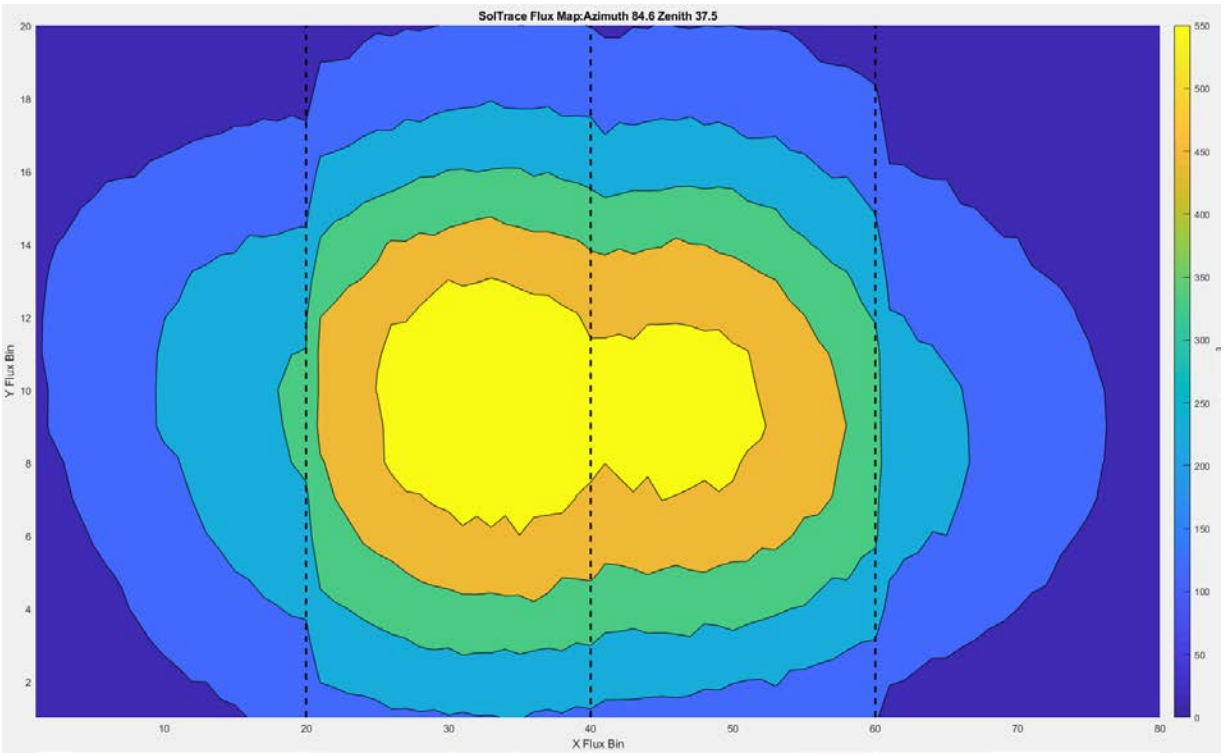

Case 5: Azimuth 104.3° Zenith 61.9°

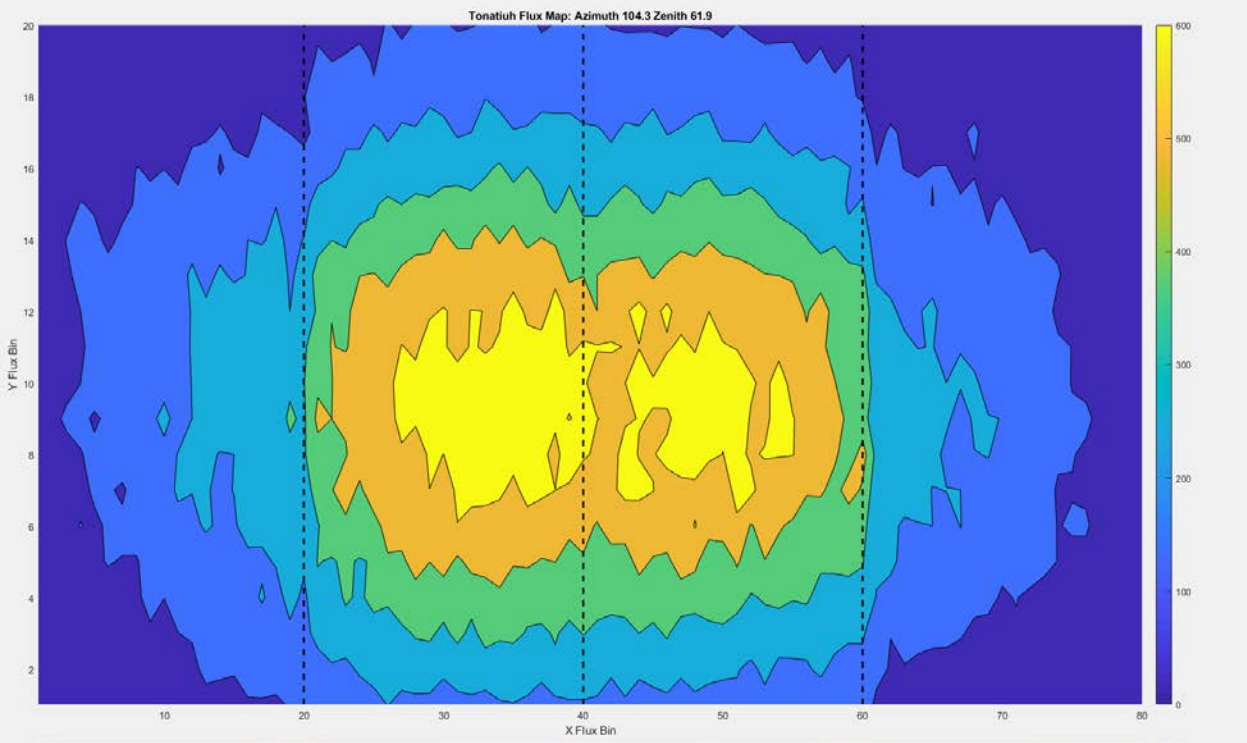

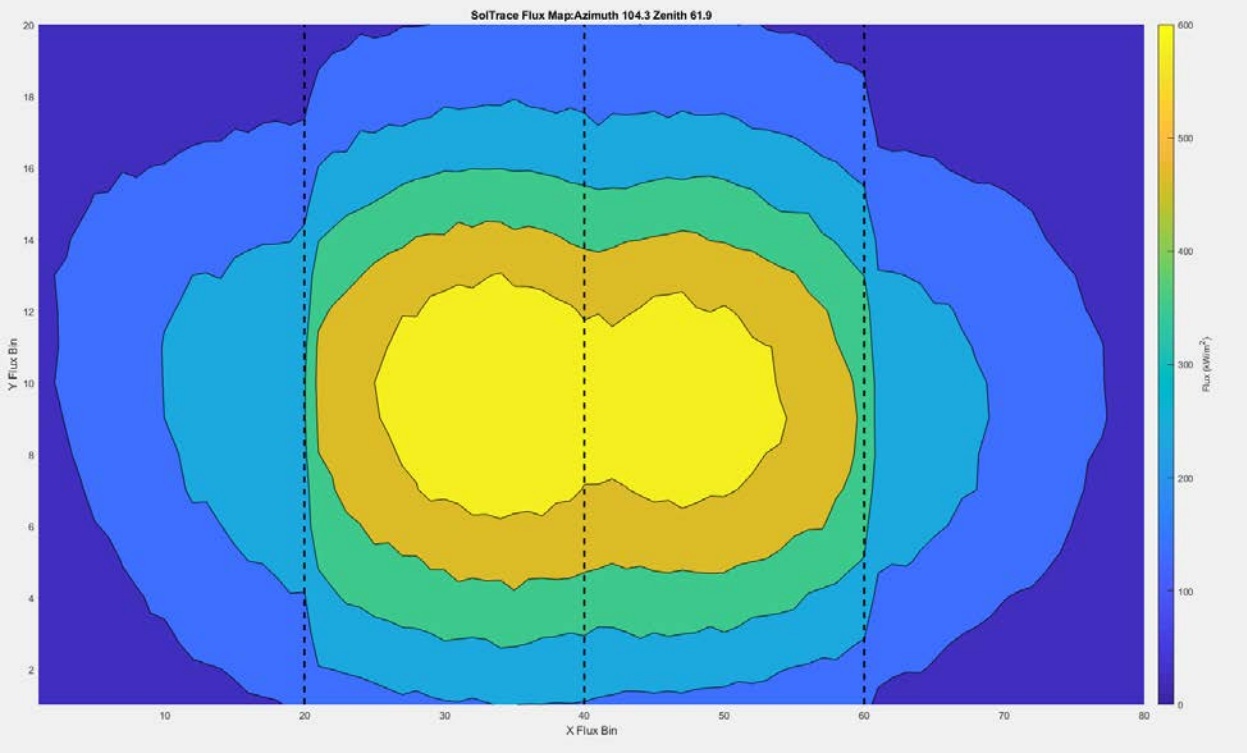

Case 7: Azimuth 180° Zenith 79.3°

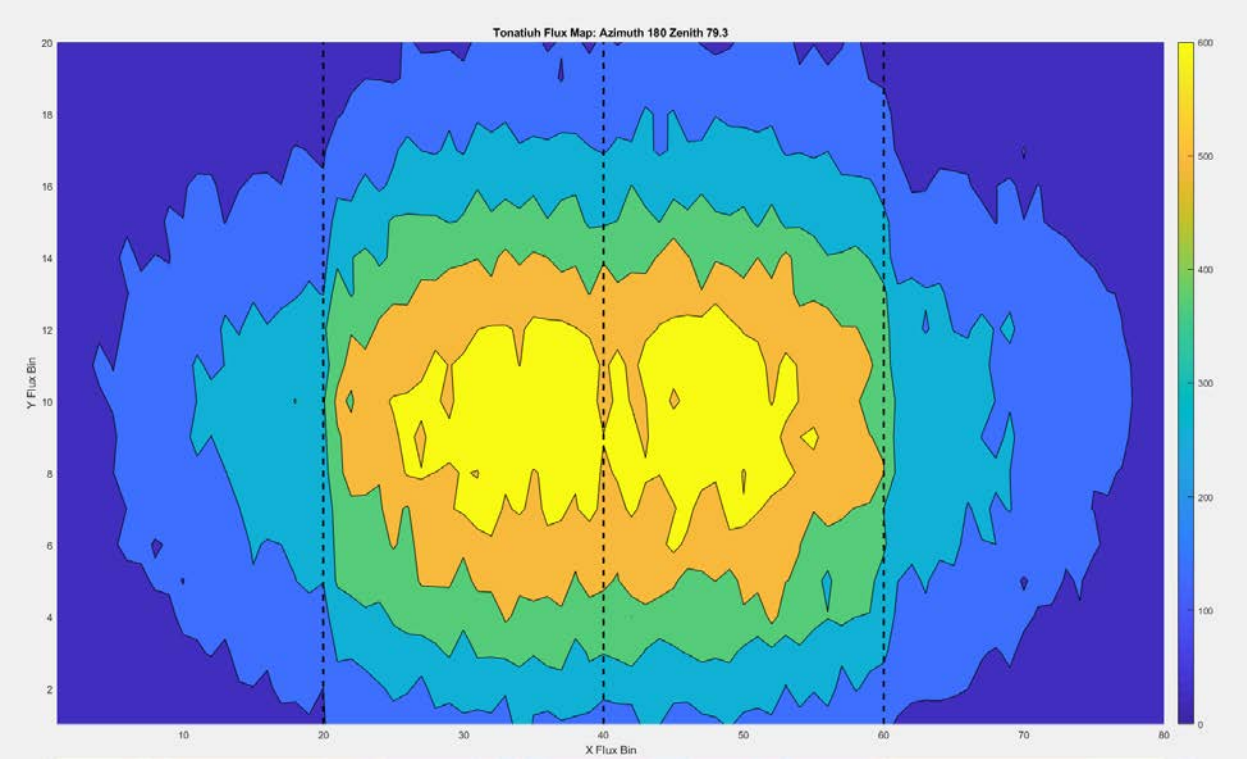

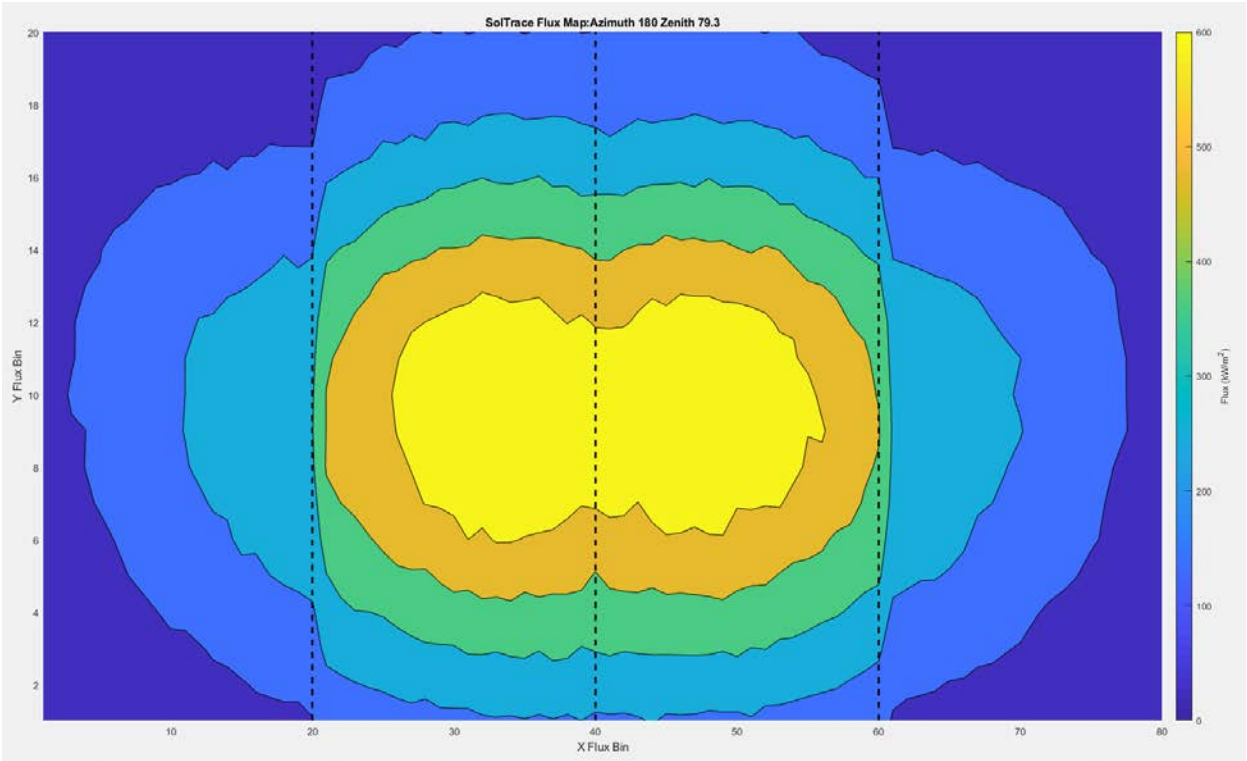

Appendix B: Tables from Thermal Simulation Case Studies.

Coating Comparison. Active and Passive surface have the same α and ε values			
Coating	Inconel	Pyromark	TiSi
α - active	0.9	0.95	0.95
α - passive	0.9	0.95	0.95
ε - active	0.88	0.85	0.47
ε - passive	0.88	0.85	0.47
Solar Loss (%)	4.99	2.44	2.44
Thermal Loss (%)	4.11	3.30	2.66
Convection Loss (%)	1.93	1.80	1.82
Efficiency (%)	88.97	92.16	93.08
Passive Surface Temp (K)	876	794	804

Coating Comparison. Passive surface are set as highly reflective material			
Coating	Inconel	Pyromark	TiSi
α - active	0.9	0.95	0.95
α - passive	0.05	0.05	0.05
ε - active	0.88	0.85	0.47
ε - passive	0.05	0.05	0.05
Solar Loss (%)	6.06	2.46	2.97
Thermal Loss (%)	3.23	2.47	2.13
Convection Loss (%)	1.32	1.28	1.19
Efficiency (%)	89.39	93.58	93.71
Passive Surface Temp (K)	507	472	418

Added 2(m) top and bottom lips. Active and Passive surface have the same α and ε values			
Coating	Inconel	Pyromark	TiSi
α - active	0.9	0.95	0.95
α - passive	0.9	0.95	0.95
ε - active	0.88	0.85	0.47
ε - passive	0.88	0.85	0.47
Solar Loss (%)	2.84	1.75	1.75
Thermal Loss (%)	2.83	2.31	2.18
Convection Loss (%)	2.31	2.18	2.22
Efficiency (%)	92.02	93.47	93.85
Passive Surface Temp (K)	913	854	866

Added 2(m) top and bottom lips. Passive surface are set as highly reflective material			
Coating	Inconel	Pyromark	TiSi
α - active	0.9	0.95	0.95
α - passive	0.05	0.05	0.05
ε - active	0.88	0.85	0.47
ε - passive	0.05	0.05	0.05
Solar Loss (%)	4.35	1.78	2.11
Thermal Loss (%)	2.34	1.77	1.68
Convection Loss (%)	1.56	1.40	1.34
Efficiency (%)	91.76	94.91	94.87
Passive Surface Temp (K)	572	495	464

Cavity receiver with convection turned off. Active and passive surfaces are the same coating			
Coating	Inconel	Pyromark	TiSi
α - active	0.9	0.95	0.95
α - passive	0.9	0.95	0.95
ε - active	0.88	0.85	0.47
ε - passive	0.88	0.85	0.47
Solar Loss (%)	4.99	2.44	2.44
Thermal Loss (%)	4.44	3.55	3.07
Convection Loss (%)	0	0	0
Efficiency (%)	90.57	93.68	94.49

External receiver with convection turned off.			
Coating	Inconel	Pyromark	TiSi
α - active	0.9	0.95	0.95
α - passive	0.9	0.95	0.95
ε - active	0.88	0.85	0.47
ε - passive	0.88	0.85	0.47
Solar Loss (%)	10.00	5.00	5.00
Thermal Loss (%)	5.16	5.11	2.86
Convection Loss (%)	0	0	0
Efficiency (%)	84.84	89.89	92.14

External receiver with convection value of cavity receiver.			
Coating	Inconel	Pyromark	TiSi
α - active	0.9	0.95	0.95
α - passive	0.9	0.95	0.95
ε - active	0.88	0.85	0.47
ε - passive	0.88	0.85	0.47
Solar Loss (%)	10.00	5.00	5.00
Thermal Loss (%)	5.13	5.08	2.84
Convection Loss (%)	1.17	1.16	1.17
Efficiency (%)	83.69		90.98